

AD-A040 396

ROCKWELL INTERNATIONAL ANAHEIM CALIF AUTONETICS GROUP  
LAMINAR BODY ANALYSIS HEAT PLUS SUCTION STABILIZED.(U)

DEC 76 R S SCOTTI, K T CORBETT

F/G 20/4

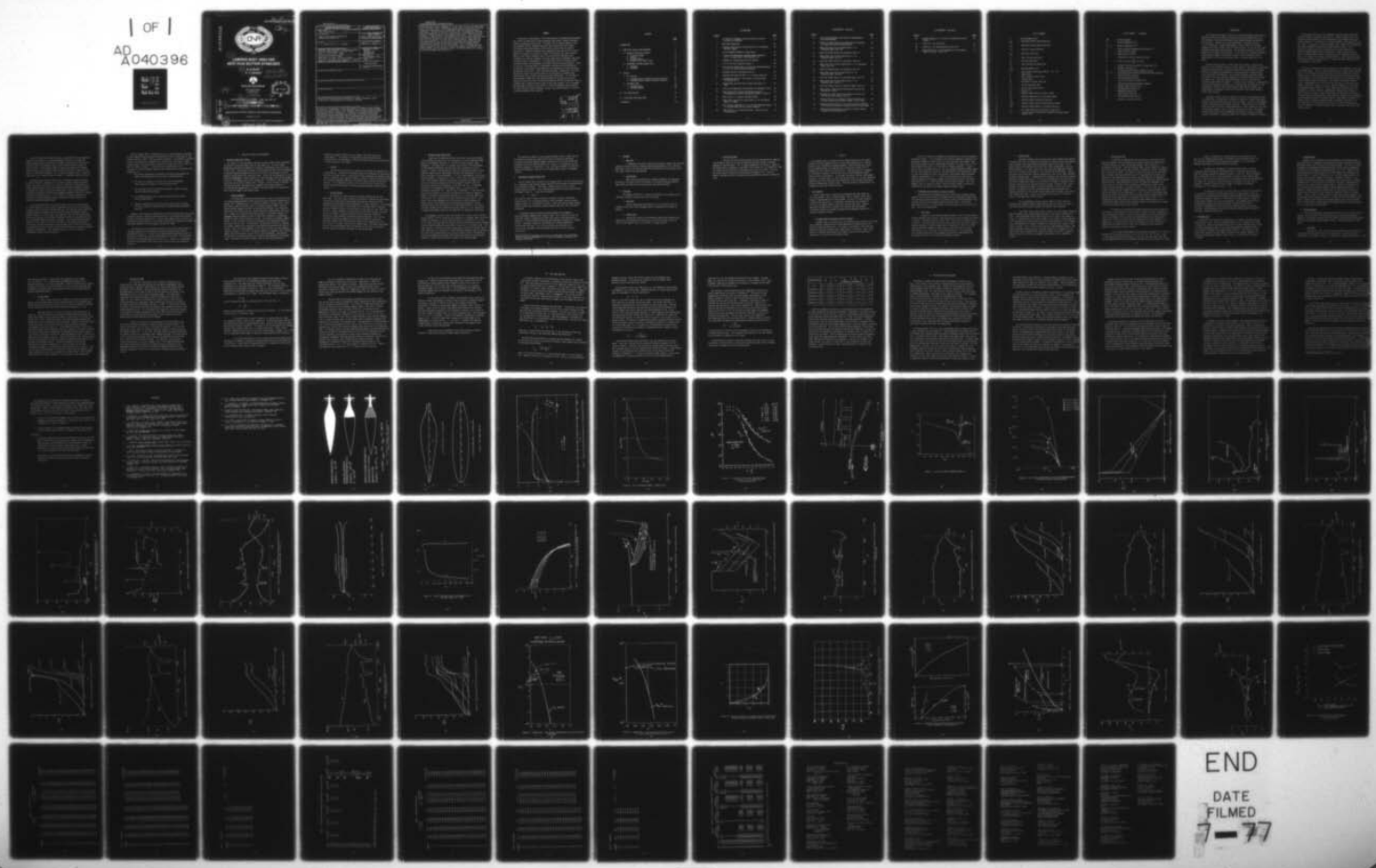
N00014-76-C-0586

ONR-CR289-013-1F

NL

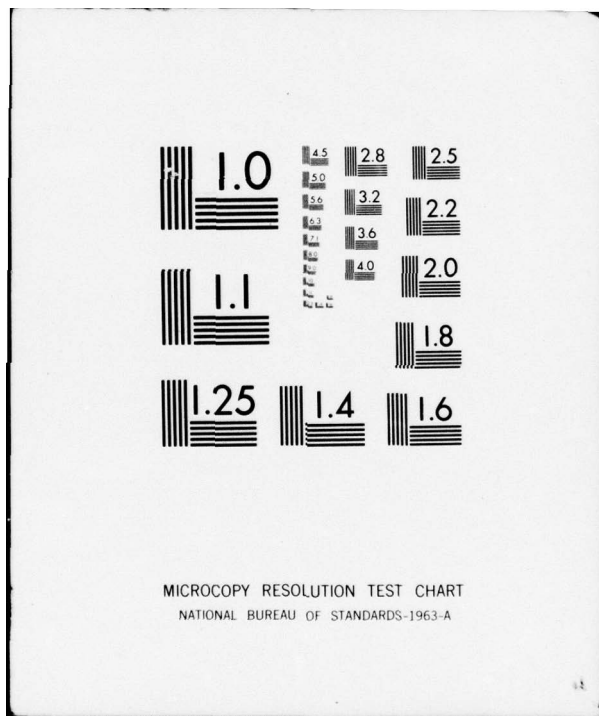
UNCLASSIFIED

| OF |  
AD  
A040396  
EEF EER



END

DATE  
FILMED  
7-77



(18) (19)  
REPORT ONR-CR 289-013-1F

ADA040396



(6) **LAMINAR BODY ANALYSIS  
HEAT PLUS SUCTION STABILIZED .**

(10) R. S./Scotti  
K. T./Corbett

(16) RR03141

(17) RR0314181



Rockwell International

Marine Systems Division  
Autonetics Group  
3370 Miraloma Avenue  
P.O. Box 4921  
Anaheim, California 92803

DDC

JUN 10 1977

B

CONTRACT N00014-76-C-0586 ONR TASK 289-013

(15) (11) 22 DECEMBER 1976

FINAL REPORT FOR PERIOD 1 APRIL 1976 — 30 OCTOBER 1976

Approved for Public Release; Distribution Unlimited

DDC FILE COPY



PREPARED FOR THE

OFFICE OF NAVAL RESEARCH • 800 N. QUINCY ST. • ARLINGTON • VA • 22217

390713

## UNCLASSIFIED

SECURITY CLASSIFICATION OF THIS PAGE (When Data Entered)

REPORT DOCUMENTATION PAGE		READ INSTRUCTIONS BEFORE COMPLETING FORM
1. REPORT NUMBER ONR-CR289-013-1F	2. GOVT ACCESSION NO.	3. RECIPIENT'S CATALOG NUMBER
4. TITLE (and Subtitle) "HEAT PLUS SUCTION STABILIZED LAMINAR BODY ANALYSIS"		5. TYPE OF REPORT & PERIOD COVERED FINAL REPORT 1 APRIL 1976 to 30 OCT 76
		6. PERFORMING ORG. REPORT NUMBER
7. AUTHOR(s) R. S. Scotti and K. T. Corbett		8. CONTRACT OR GRANT NUMBER(s) N00014-76-C-0586 new
9. PERFORMING ORGANIZATION NAME AND ADDRESS Rockwell International, Autonetics Group 3370 Miraloma Avenue, P.O. Box 3105 Anaheim, California 92803		10. PROGRAM ELEMENT, PROJECT, TASK AREA & WORK UNIT NUMBERS 61153N RR031-01-81 NR 289-013
11. CONTROLLING OFFICE NAME AND ADDRESS Department of Navy, Office of Naval Research, Vehicles and Propulsion Program, Code 211, Arlington, VA 22217		12. REPORT DATE 22 December 1976
14. MONITORING AGENCY NAME & ADDRESS (if different from Controlling Office)		13. NUMBER OF PAGES 80
		15. SECURITY CLASS. (of this report) UNCLASSIFIED
		15a. DECLASSIFICATION/DOWNGRADING SCHEDULE
16. DISTRIBUTION STATEMENT (of this Report)		
17. DISTRIBUTION STATEMENT (of the abstract entered in Block 20, if different from Report)		
18. SUPPLEMENTARY NOTES		
19. KEY WORDS (Continue on reverse side if necessary and identify by block number) Navy Vehicle Design and Construction; Laminar Boundary Layer Transition; Drag Reduction; Suction; Heating		
20. ABSTRACT (Continue on reverse side if necessary and identify by block number) An analytical investigation of the effectiveness of combined surface heating and suction in stabilizing a laminar boundary layer within a region of adverse pressure gradient was carried out. The study is of an applied nature in that two candidate vehicle configurations, which were selected for their widely differing pressure distributions, were utilized as test beds for specific calculations. Numerical boundary layer computations were carried out for each vehicle for various distributions of suction and heating over their surfaces. Results in the form of boundary layer flow and stability characteristics → next page		

UNCLASSIFIED

SECURITY CLASSIFICATION OF THIS PAGE(When Data Entered)

illuminate the relative strengths of the two stabilization techniques taken both individually and in combinations. The stabilizing effects of heating, being relatively weaker, are overwhelmed by moderate adverse pressure gradients. Those of suction, on the other hand, are apparently unlimited and constrained only by practical considerations associated with the withdrawal of large fractions of the boundary layer itself. Under some flow conditions, combinations of surface heating and suction may be more practical and efficient for boundary layer stabilization than of either technique utilized individually. For the sake of more meaningful comparison, the drag equivalents of the suction and of the heating processes have been calculated and combined with the hydrodynamic drag to estimate total, effective drag for each of the cases treated. Also, an attempt has been made to generalize the results in terms of parameters which describe the three effects, pressure gradient, suction and surface heating, in relation to laminar boundary layer stability.

UNCLASSIFIED

SECURITY CLASSIFICATION OF THIS PAGE(When Data Entered)

## SUMMARY

An analytical investigation of the effectiveness of combined surface heating and suction in stabilizing a laminar boundary layer within a region of adverse pressure gradient was carried out. The study is of an applied nature in that two candidate vehicle configurations, which were selected for their widely differing pressure distributions, were utilized as test beds for specific calculations. Numerical boundary layer computations were carried out for each vehicle for various distributions of suction and heating over their surfaces. Results in the form of boundary layer flow and stability characteristics illuminate the relative strengths of the two stabilization techniques taken both individually and in combinations. The stabilizing effects of heating, being relatively weaker, are overwhelmed by moderate adverse pressure gradients. Those of suction, on the other hand, are apparently unlimited and constrained only by practical considerations associated with the withdrawal of large fractions of the boundary layer itself. Under some flow conditions, combinations of surface heating and suction may be more practical and efficient for boundary layer stabilization than of either technique utilized individually. For the sake of more meaningful comparison, the drag equivalents of the suction and of the heating processes have been calculated and combined with the hydrodynamic drag to estimate total, effective drag for each of the cases treated. Also, an attempt has been made to generalize the results in terms of parameters which describe the three effects, pressure gradient, suction, and surface heating, in relation to laminar boundary layer stability.

NTIS	White Section	<input checked="" type="checkbox"/>
DOC	Buff Section	<input type="checkbox"/>
UNARMED		<input type="checkbox"/>
JUSTIFICATION		
BY _____		
DISTRIBUTION/AVAILABILITY CODES		
DISC.	AVAIL. AND/OR SPECIAL	
A		

## CONTENTS

	<u>Page</u>
INTRODUCTION	1
I. ANALYTICAL DETAILS AND PROCEDURES	5
A. REVIEW OF ANALYTICAL DETAILS	5
1. Pressure Gradient	5
2. Suction	6
3. Surface Heating	6
4. Boundary Layer Shape Factor	7
B. PROCEDURES FOLLOWED DURING STUDY	8
1. Forebody	9
2. Afterbody	9
II. RESULTS	11
A. AR-3 VEHICLE	11
1. Forebody Region (Favorable Pressure Gradient)	11
2. Afterbody Region (Adverse Pressure Gradient)	12
B. REICHARDT BODY	15
1. Forebody Region	16
2. Afterbody Region	16
III. HULL DRAG ANALYSIS	22
IV. DISCUSSIONS AND CONCLUSIONS	26
REFERENCES	32

## ILLUSTRATIONS

<u>Figure</u>		<u>Page</u>
1	The Effects of Geometry, Heat and Heat Plus Suction on Vehicle Performance	34
2	Body Shape Comparison	35
3	Potential Flow Velocity Distributions for 5:1 Reichardt and AR-3 Shapes	36
4	Critical Reynolds Number vs Shape Factor	37
5	Critical and Transitional Reynolds Numbers (Based on "e <sup>9</sup> ") vs. Shape Factor (from Reference 13)	38
6	Schematic of Afterbody Suction Plus Heating	39
7	H vs S/L for AR-3 (Reference Table 1)	40
8	Skin Friction Coefficient vs S/L for the Afterbody Region of AR-3 for Several Surface Overheats	41
9	Afterbody Suction Distributions (AR-3)	42
10	Continuous Suction Cold Wall, $\Delta T = 0$ (after Figure 9)	43
11	Discontinuous Suction - The Effects of Varying Width of Heating (AR-3)	44
12	Discontinuous and Continuous Suction High Value, $\Delta T = 35^{\circ}\text{F}$	45
13	Suction and Temperature Distributions on Afterbody of AR-3	46
14	Shape Factor and Friction Coefficient Histories Corresponding to Suction and Heating shown in Figure 13	47
15	Shape Factor vs. Distance (Reichardt Body)	48
16	Shape Factor and Friction Coefficient vs. S/L (Reichardt Body, $\Delta T = 40^{\circ}\text{F}$ )	49
17	Skin Friction Coefficient vs. S/L for the Afterbody Region of the Reichardt Body for Several Overheats	50
18	Shape Factor vs. S/L (Reichardt Body - Various Suction Distributions)	51

ILLUSTRATIONS - Continued

<u>Figure</u>		<u>Page</u>
19	Suction and Temperature Distributions Investigated on the Reichardt Body	52
20	Effects of Surface Heating on Shape Factor in Presence of Unfavorable $dp/dx$ (Reichardt Body)	53
21	Shape Factor and Friction Coefficient vs. S/L (Reichardt Body, Case 1-W)	54
22	Stability Growth Factors for Reichardt, Case 1-W	55
23	Shape Factor and Friction Coefficient vs. S/L Reichardt Body, Case 2-W	56
24	Stability Growth Factors for Reichardt, Case 2-W	57
25	Shape Factor and Friction Coefficient vs. S/L (Reichardt Body, Case 3-W)	58
26	Stability Growth Factors for Reichardt, Case 3-W	59
27	Shape Factor and Friction Coefficient vs. S/L Reichardt Body, Case 4-W	60
28	Stability Growth Factors for Reichardt Body, Case 4-W	61
29	Shape Factor and Friction Coefficient vs. S/L Reichardt Body, Case 5-W	62
30	Stability Growth Factors for Reichardt Body, Case 5-W	63
31	Shape Factor - Reg* History Discontinuous Suction Plus Heating (AR-3 Body)	64
32	Shape Factor - Reg* History Discontinuous Suction Plus Heating (Reichardt Body, Case 1-W)	65
33	Velocity Profiles in an Adverse Pressure Gradient with Suction and Heating (reference Figure 12, AR-3 Body)	66
34	Second Derivative Profiles in an Adverse Pressure Gradient with Suction and Heating (reference Figure 12, AR-3 Body)	67
35	Required Surfacing Heating and Suction to Delay Laminar Separation (from Reference 11)	68

ILLUSTRATIONS - Continued

<u>Figure</u>		<u>Page</u>
36	Suction Parameter vs. $\beta$ History for Reichardt and AR-3 Bodies	69
37	$\beta$ and $C_f$ vs. S/L (AR-3 Body)	70
38	$\beta$ and $C_f$ vs. S/L {Reichardt Body (Case 1-W)}	71
39	Drag Coefficient vs. Suction Quantity (8:1) Reichardt Body in Air $Re_L = 18.2 \times 10^6$	72

## LIST OF SYMBOLS

A	= Area parameter (ft <sup>2</sup> )
$C_{D_H}$	= Equivalent heating drag coefficient
$C_{D_S}$	= Equivalent suction drag coefficient
$C_{D_t}$	= Total hull drag coefficient
$C_{D_W}$	= Wake drag coefficient
$C_f$	= Skin friction coefficient
$C_p$	= Pressure coefficient
$C_{Q_t}$	= Total suction flow coefficient
$d_{max}$	= Maximum diameter (ft)
h	= Heat transfer coefficient (BTU/hr - ft <sup>2</sup> - °F)
H	= Shape factor
L	= Total length of vehicle (ft)
P	= Pressure (psi)
$P_H$	= Pump power for waste heat (hp)
$P_S$	= Suction pump power (hp)
Q	= Suction flow rate (ft <sup>3</sup> /sec)
R	= Radius (ft)
$R_L$	= Reynolds number based on vehicle length
$R_{tr}$	= Reynolds number based on transition length
$R_e$	= Reynolds number (reference Figure 36)
$Re_{\delta^*}$	= Reynolds number based on displacement thickness
$Re_x$	= Reynolds number based on x distance from nose
S	= Arc length from nose along body's surface (ft)
$S_0$	= Torodial area of boundary layer momentum thickness around vehicle (ft <sup>2</sup> )

LIST OF SYMBOLS - Continued

SHP	=	Shaft horsepower
$T_w$	=	Surface temperature ( $^{\circ}$ F)
$T_{\infty} = T_a$	=	Ambient temperature ( $^{\circ}$ F)
$\Delta T$	=	Surface overheat temperature difference ( $^{\circ}$ F)
U	=	Local velocity (ft/sec)
$U_e$	=	Edge velocity (ft/sec)
$U_{\infty}$	=	Freestream or vehicle velocity (ft/sec)
$U''$	=	Profile curvature $\frac{\partial^2 U}{\partial Y^2}$ (1/ft-sec)
x	=	Distance from nose of vehicle straight back (ft)
y	=	Distance from wall (ft)
W	=	Tollmien-Schlichting wave frequency (1/sec)
$W^* = w^*$	=	Non-dimensionalized Tollmien-Schlichting wave frequency
$v_w$	=	Suction velocity (ft/sec)
$\alpha$	=	Disturbance amplitude (ft)
$\alpha_0$	=	Initial disturbance amplitude (ft)
$\beta$	=	Falkner-Skan pressure gradient parameter
$\delta$	=	Boundary layer thickness (ft)
$\delta^*$	=	Displacement thickness (ft)
$\theta$	=	Momentum thickness (ft)
$\rho$	=	Local density (lbs/ft <sup>3</sup> )
$\rho_{\infty}$	=	Freestream density (lbs/ft <sup>3</sup> )
$\nu$	=	Kinematic viscosity (ft <sup>2</sup> /sec)

## INTRODUCTION

The principal advantages of laminar over turbulent boundary layer flow for operational vehicles are reduced frictional drag and diminished self noise. Such prospects of increased performance have tempted designers and engineers over the years. However, due to the uncertainty of transition and the crucial differences in designs appropriate to either laminar or turbulent boundary layer flows, laminar flow and transition have, for the most part, been designed around rather than exploited. The strongest deterrents to practical application of laminar flow have been: (1) The inability to achieve transition length Reynolds numbers of practical interest, and (2) a profound lack of understanding of the transition process itself, including prediction of its onset.

Important break-throughs in recent years have, however, attracted more attention to and rekindled interest in these problems. Specifically, considerable progress has been achieved in extending transition to higher Reynolds numbers utilizing the stabilizing mechanisms of pressure gradient<sup>1</sup> (vehicle shape), surface heating<sup>2,3</sup> and suction<sup>4</sup>. New, elaborate computer codes which model the present transition prediction theories are now operational<sup>5</sup> and available for general use. These are being corroborated as well as improved by an increasing experimental data base<sup>6,7</sup>. In short, recent advances in understanding of the transition process (though still incomplete) and of techniques for the maintenance of laminar flow to significantly higher Reynolds numbers have brought about a resurgence of hope for the practical and reliable design of laminar flow vehicles.

Ultimately, however, before a laminar flow vehicle can be deemed suitable for application, a reckoning of the desirable features of laminar flow against reliability and effective costs will have to be made. The risk and consequences of early transition must be carefully assessed. Effective costs, on the other hand, would take the form of system complexity, of limits imposed on the range of operating conditions, and, of course, of dollars and cents. The subject of the present report, while fundamental and technical in nature, provides valuable information to eventually enable this necessary reckoning or trade-off.

As previously mentioned, three parameters have been shown to favorably affect the stability and delay transition of a laminar boundary layer; viz, favorable pressure gradient, surface temperature (over ambient) and surface suction velocity.<sup>6,7</sup> Increasing any of these parameters individually will aid, to a limit, in stabilizing a laminar boundary layer. When used in combination, the effects undoubtedly become interrelated and more complex. Still, theoretical studies have led to the prediction of large extensions of transition length Reynolds numbers when heat is added to the surface of a vehicle forebody, where pressure is decreasing in the streamwise direction, that is, in a region of favorable pressure gradient. These results have been confirmed (at the least) qualitatively in recent laboratory experiments<sup>3</sup> and in the Autonetics flow tube.<sup>8</sup>

The focus of the present study is primarily on the afterbody, rather than the forebody region. Here the pressure gradients are strongly adverse and the effects of suction must be called into play in order to stabilize a laminar boundary layer. Before describing the intent and scope of the present study, it would be well to first complete the description of its motivation by means of the following sample calculations: The vehicle configuration shown in Figure 1 (designated as AR-3, one of the two utilized as a test bed in the present study) has a length of 55 feet, a maximum diameter of 11 feet and a displacement volume of 2446 ft<sup>3</sup>. Given a power plant with 2000 SHP, drag estimates for a fully turbulent, unheated hull boundary layer indicates a vehicle speed of 35 knots. Now if the forebody is heated with a portion of the waste heat from the propulsion system such that laminar flow is maintained to the streamwise location of minimum pressure (approximately 72 percent of length), drag is reduced and vehicle speed is increased to 55 knots. At this condition, the last 28 percent of the vehicle, the afterbody region, which is supporting a turbulent boundary layer, contributes about 90% of the remaining drag.

If the afterbody were laminarized, say, by the addition of the remaining waste heat, of suction, or of some combination of the two, to extend the laminar boundary layer to 90 percent of length, the drag falls to 12 percent of that of the fully turbulent vehicle and the vehicle speed increases to nearly 75 knots. From another viewpoint, the 55-knot speed for the heated laminar vehicle may be obtained with a 33 percent reduction in power for the case of a laminarized afterbody. This is indeed an appealing and - within the frame work of the available stability theory - a completely feasible prospect.

The stabilizing effects of suction are considerably stronger than those of surface heating<sup>9</sup>, particularly in a region of adverse pressure gradient. However, by clever and efficient utilization of propulsion system waste heat, surface heating appears to be a less complicated and more economical technique as compared to suction for practical applications. With a view towards the aforementioned necessary reconciliation between performance gains due to laminar flow and corresponding costs, it is of interest to attempt to maximize the utilization of heat and thereby reduce the amount of suction necessary to laminarize afterbody boundary layers.

The problem addressed in the present study is that of the effectiveness of surface heating, of suction and of combinations of the two in the afterbody or adverse pressure region of laminar vehicles. The study was purely analytical, although support and guidance was taken from relevant experimental studies whenever possible. In this regard, the Autonetics Flow Tube at Colorado State University has proven to be a unique, flexible, relatively inexpensive facility for high Reynolds number laboratory experiments. The present problem has been idealized in the sense that no notice was taken of the probable engineering difficulties associated with neatly injecting heat into the vehicle surface and with operating micro-pore suction surfaces on the presence of naturally occurring (clogging) contaminants. These further aspects are, in fact, presently, simultaneously under study at Autonetics.

Two hull shapes, both of fineness ratio 5 to 1, were selected on the basis of their widely differing pressure distributions to serve as test beds for the present analytical study. These are shown in Figure 2. The external or potential velocity distributions corresponding to a vehicle speed that yields a length Reynolds number at minimum pressure location of at least  $250 \times 10^6$  (in water at 40°F) are shown in Figure 3. Calculations were performed utilizing axisymmetric, finite-difference boundary layer computer codes to determine such quantities as:

1. The forebody temperature distributions and heating requirements for laminar flow stabilization to the point of minimum pressure.
2. The limits of extension of laminar flow into the afterbody's adverse pressure gradient with surface heating alone.
3. The continuous suction distributions required to maintain laminar flow over the entire afterbody.
4. The intermittent heat plus suction distributions which provide similar stabilization.
5. Stability characteristics for the various cases tested, including critical disturbance frequencies and corresponding amplitude growth histories.

Moreover, total drag was estimated for the two hull shapes under the various conditions studied. Wake drag, drag equivalent of suction and drag equivalent of heating have been accounted for. A total drag summary serves as a basis for comparison of effectiveness of the different laminar flow stabilization schemes, not only among themselves but also between the two hull shapes.

Some discussion of the theoretical details which describe the effects of pressure gradient, surface heating and suction on boundary layer flows is presented in Section I. The step by step computational procedures as well as an overview of the range of cases investigated is also given. The calculated results are presented and described in Section II. Section III is dedicated to the hull drag analysis while discussions and conclusions are contained in Section IV.

## I. ANALYTICAL DETAILS AND PROCEDURES

### A. REVIEW OF ANALYTICAL DETAILS

The effects of pressure gradient and wall suction on both laminar separation and transition have been under study for many years now. In fact, Prandtl demonstrated the delay of separation by suction in experiments carried out over 70 years ago<sup>4</sup>. In the case of suction, delayed separation most likely corresponds to delayed transition because the effects of suction on the boundary layer are powerful and are felt across the entire layer. Within the last decade or so, the additional technique of surface heating for a water boundary layer has been added to the list of boundary layer control mechanisms. The details of the analyses and experiments are of little interest here. However, a brief listing of the major findings along with a few graphs which summarize the relevant parametric relationships for stabilization of laminar flow would perhaps be an appropriate way to set the stage for the present study.

#### 1. Pressure Gradient

It has been well established experimentally as well as analytically that a favorable pressure gradient stabilizes and an adverse gradient destabilizes a laminar flow.<sup>6</sup> Mechanistically, a favorable gradient of pressure tends to thin the boundary layer and thereby lower its thickness Reynolds number, while an adverse gradient destabilizes the flow through the formation of an inflection point within the velocity profile. Recent theoretical (approximate) results by King<sup>9</sup> suggest that increased stability produced by "reasonable" changes in a favorable pressure gradient are smaller than those produced by corresponding changes in either surface heating or suction. The problem is extremely complex, however, in the sense that the relative strengths of the mechanisms depend on the actual level of each. In other words, the magnitude of effects of heating, for example, depend on the magnitude of the pressure gradient and the level of suction. Still, the above statement is believed to be true over the parametric ranges of interest. The effects of pressure gradient on boundary layer stability compete with the other two in a way that is little understood - particularly for the case of an adverse gradient, as identified and addressed in the present study. The effects of pressure gradient, suction and surface heating on

separation of laminar boundary layers, however, have been previously investigated.<sup>10</sup> The results for separation are both interesting and illuminating for the phenomenon of stability/transition and will be discussed in later sections of this report.

## 2. Suction

The stabilizing influence of suction occurs through two separate but related effects: Thinning of the boundary layer and alterations of the profile. Both are of a global nature in that they are felt throughout the boundary layer. Suction, therefore, has a powerful effect on stability; stability characteristics are intimately dependent upon both the boundary layer velocity and curvature profiles. It is apparently possible, at least intuitively, to stabilize a laminar boundary layer against any adverse pressure gradient with sufficient suction.

## 3. Surface Heating

The effects of surface heating on laminar stabilization are less well-known. The linear theory stability calculations of Wazzan and Smith which incorporate surface heating have become quite popular recently and their agreement with experiments using heated models is indeed impressive. The effects of surface heating for water (Prandtl number of 8) have been shown to manifest primarily through viscosity variations and to be confined to a thin layer near the wall. Slight alterations of the velocity profile near the wall are shown by the calculations of Wazzan and Smith to have significant effects on transition in both favorable and adverse pressure gradients. The localized influence of heating as compared to the global influence of suction on transition suggest that heating would be strongly overshadowed by suction. This issue is, of course, central to the present study. Few known calculations and very little experimental data are available for the case of an adverse pressure gradient, excluding the output of the present study.

#### 4. Boundary Layer Shape Factor

Experience has demonstrated that the effects of pressure gradient, surface heating and suction can be correlated to a critical Reynolds number based on displacement thickness as a function of gross boundary layer parameters. The shape factor,  $H$ , defined as the ratio of the displacement to the momentum thicknesses, has been used quite successfully in this capacity. Figure 4 from Reference 6 shows the relationship between critical Reynolds number based on displacement thickness and shape factor,  $H$ , for flows involving all three mechanisms. To a first approximation, the critical Reynolds number is a function of  $H$  alone. This is not, in general, strictly true. More accurate, detailed calculations for Falkner-Skan wedge flow profiles carried out recently by Gazley and Wazzan<sup>11</sup> indicate that the correlation requires two parameters, one of which may be  $H$ . Furthermore, the history or evaluation of the boundary layer - as evinced by the streamwise distribution of  $H$  - may also be of importance. In the same study, they also constructed a first order correlation of a transition Reynolds number (also based on displacement thickness) to  $H$  for the same wedge flows utilizing the " $e^9$ " criterion to indicate transition (see Figure 5). Their results are in good agreement with calculations performed by Wazzan for heated, laminar flow vehicles and with preliminary experimental results obtained during tests with models of the same heated vehicles. The studies by Gazley and Wazzan are continuing and quite promising, in the presence of a growing experimental data base for comparisons to theoretical predictions.

The immediate utility of such correlations lies in their use for vehicle design studies<sup>12</sup> and for indicating the probability of boundary layer transition without the necessity of costly, detailed stability calculations.<sup>13</sup> It was in the latter role that good use was made of the established correlation between critical Reynolds number and shape factor (Figure 4) in the present study. The shape factor is relatively easy and inexpensive to monitor for various vehicle flow conditions, say, by means of finite difference boundary layer calculations. Only those flow configurations that survive scrutiny of their  $H$  distribution need be investigated for boundary layer stability by means of the relatively elaborate, linear stability analysis computer code (the TAPS code).

The question of whether a given laminar boundary layer is stable can not be answered by studying the shape factor alone, as presently understood. A universal transition Reynolds number correlation has yet to be established. Exceeding the critical Reynolds number for a given  $H$  is a necessary, but not sufficient condition for transition - hence, the need ultimately for detailed stability calculations. More will be said about these factors in subsequent sections.

#### B. PROCEDURES FOLLOWED DURING STUDY

Two hull shapes were selected for the present study: the first, the so-called AR-3, generated by the Parsons-Goodson routine<sup>14</sup> and the second, a Reichardt body, as illustrated in Figure 2. Both have a fineness ratio of 5 to 1 and an assumed length of 55 feet. Their corresponding potential velocity distributions are shown in Figure 3. Using the relationship

$$C_p = 1 - (U/U_\infty)^2$$

The curves in Figure 3 may be rescaled to potential pressure coefficient. Attention here is to be focused primarily on the afterbody, adverse pressure gradient region. As illustrated in Figure 2, these two vehicles taken together afford a broad range of adverse pressure gradient over their quite dissimilar afterbodies.

All boundary layer calculations were performed with axisymmetric, finite difference boundary layer computer codes\* such as that built into the Transition Analysis Program System (TAPS) code, which is now operational at Autonetics. Detailed stability analyses were performed by Professor F. Wazzan of UCLA. These were compared to and extended by in-house computations utilizing the TAPS code. The following step-by-step procedures were (more or less) employed during the computational phase of this study for each vehicle.

---

\*We would like to acknowledge and express our appreciation for the boundary layer calculations performed by Dr. C. Merkle of Dynamics Technology, Inc., Torrance, California.

## 1. Forebody

### a. Heat Only

A temperature distribution which would maintain laminar flow over the favorable pressure gradient, forebody region was determined by trial and error. Both shape factor H and detailed stability calculations were utilized to insure that stable laminar flow was obtained.

### b. Suction Only

Weak suction was applied over unheated forebodies to investigate the effects of suction relative to heating in a favorable pressure gradient. Shape factor and stability calculations were once again monitored.

## 2. Afterbody

The heating selected in 1 (above) was applied on the forebody for all subsequent afterbody configurations and calculations.

### a. Heat Only

Various temperature distributions, up to a practical limit of overheating, were tried in the afterbody region to investigate the effects of heating.

### b. Suction Only

Suction was applied to the afterbody region while monitoring the shape factor to determine the minimum levels and distributions required to stabilize the boundary layer to the 90-95% of length position.

c. Suction Plus Heat

The best suction distribution from (b) was then modified by removing circumferential strips of suction and replacing them with strips of constant temperature, heated surface. This is shown schematically on Figure 6. Width of the heated strips, abruptness of transition from "suction on" to "suction off" (and vice versa) and the locations of the heated strips were all varied. Initially, the results were scrutinized by monitoring the evaluation of H. Later on, however, detailed stability calculations were performed for the most interesting cases.

## II. RESULTS

The forebody section is taken to be the forward position of the vehicle extending from the stagnation point to the minimum pressure point. Minimum pressure occurs downstream of maximum diameter. While attention was focused on the afterbody region, calculations were performed and results will be presented for both regions of both vehicles. Input data consists of geometry or coordinates, potential flow velocity field, surface temperature and/or suction velocity distribution. In raw form, the results include; displacement thickness,  $\delta^*$ ; shape factor,  $H$ ; and friction coefficient,  $C_f$ , at each streamline computing station and total wake drag (obtained by a Squire-Young integration through the downstream boundary layer). Detailed stability characteristics are presented for the most interesting cases.

### A. AR-3 VEHICLE

The hull shape shown in Figure 2a and designated AR-3 was chosen for this study because it has a large favorable pressure gradient region which extends to approximately 72% of body length. As such, it is well suited to a laminar flow application. Calculations indicate that the forebody of this hull will support laminar flow with a minimal heat input. However, beyond the minimum pressure location, the pressure gradient becomes increasingly adverse, and laminar separation and subsequent transition to turbulent flow occur rapidly.

#### 1. Forebody Region (Favorable Pressure Gradient)

Boundary layer calculations over the forebody region of the AR-3 hull have been conducted to determine the minimum temperature distribution which will maintain stabilized laminar flow. The process is basically a trial and error approach in which the boundary layer shape factor is monitored. Once a good profile is obtained, more detailed and complex stability calculations are employed to verify that the flow remains stable.

The final iteration of temperature distribution for the AR-3 forebody is presented in Table 1. Also included in this table are geometry, potential flow and surface temperature distributions for the entire body; and boundary layer calculation outputs including displacement thickness,  $\delta^*$ , shape factor, H, and heat transfer coefficient, h, to the point of laminar separation. Figure 7 shows a plot of the shape factor, H, over the favorable pressure gradient region. For this case, labeled "no suction", the shape factor falls monotonically with S/L over the forebody and then rises rapidly as the adverse pressure gradient region is encountered,  $S/L \geq .7$ . Stability calculations for this case by Professor Wazzan of UCLA show a maximum Tollmien-Schlichting wave disturbance amplification of  $e^{2.4}$  in the favorable pressure gradient region. Thus, the boundary layer is expected to remain laminar and quite stable to the point of separation at the onset of the adverse pressure gradient region.

## 2. Afterbody Region (Adverse Pressure Gradient)

Having defined the forebody conditions sufficient to maintain laminar boundary layer flow to the point of minimum pressure, subsequent boundary layer calculations were made to determine the extent to which stabilized laminar flow could be carried into the adverse pressure gradient region. Three basic approaches were tried - (a) heat alone, (b) suction alone, and (c) suction plus heat. Each is discussed below.

### a. Heat Alone

Extension of the maximum forebody overheating of  $26^{\circ}\text{F}$  into the adverse pressure gradient region results in the shape factor history labelled "no suction" in Figure 7. Greater overheats of  $80^{\circ}\text{F}$ ,  $100^{\circ}\text{F}$ ,  $120^{\circ}\text{F}$  and  $132^{\circ}\text{F}$  beginning from 5 feet to 13 feet before the point of minimum pressure show negligible effect in delaying the onset of laminar separation as indicated by a zero skin friction. Figure 8 presents a summary of these cases in terms of the skin friction coefficient,  $C_f$ , as a function of longitudinal position. This plot shows skin friction going to zero and subsequent separation at approximately the same location for all of the specified afterbody overheats.

b. Suction Alone

Subsequent boundary layer characteristics were computed with emphasis on defining the level of afterbody suction which is required to keep the boundary layer attached in the adverse pressure-gradient region of the body. Of the several suction distributions which were tried, three representative cases are given on Figure 9. For these three cases, the suction was commenced at about the 0.72 S/L location on the body ( $S = 39.6$  feet on the 55-foot body). Beyond this point, the suction was linearly increased until the .95 S/L point, and then allowed to decrease again. "Optimization" of the amount of suction was primarily achieved by rotating the  $V_w/U_\infty$  vs. S/L suction schedule about the peak point on the curve, although some checks as to the effect of changes in location of the initial starting point for the suction were also made. With the "low" suction schedule, the shape factor begins to diminish rapidly as soon as the suction section is encountered, but the strong unfavorable pressure gradient soon overcomes the effect of the suction and the shape factor increases very rapidly until separation occurs. A plot of the shape factor versus S/L is given in Figure 7, and shows these effects clearly.

The "intermediate" suction schedule shown on Figure 9 kept the boundary layer attached slightly longer than did the "low" value, but again as the pressure gradient grew more adverse the boundary layer separated.

The "high" suction level shown on Figure 9 was sufficiently strong to keep the boundary layer attached beyond the peak in the suction schedule ( $S/L = 0.95$ ). The corresponding shape factor history for this case is also shown on Figure 7. Although the scale of the ordinate on this figure is highly magnified, it is important to note how rapidly the integral characteristics of the boundary layer, represented by  $H$ , change in response to relatively small changes in the level of suction. This is the result of two very strong competing factors, the pressure gradient and the suction. Additional details of the behavior of the shape factor versus distance after the point at which the suction is begun are given on Figure 10, which has an expanded longitudinal scale as compared to Figure 7.

c. Suction Plus Heat

In addition to computations with continuously distributed suction, some discontinuous suction schedules were studied to assess the effectiveness of surface heating as a means for delaying boundary layer separation in conjunction with suction. Starting from the "high" suction schedule of Figure 9, the initial 2.5 feet of suction were retained, followed by a heated, impermeable wall (zero-suction) region. The initial 2.5 feet of suction was used to ensure that a "strong" velocity profile which was far from separation existed at the beginning of the heated non-porous section, and the length of the impermeable section was varied to determine how long the boundary layer would remain attached without suction. Some representative results for which the impermeable wall section was 0.3, 0.2 and 0.1 foot respectively (followed by a return to the original suction schedule), are shown on Figure 11. As can be seen, the initial length of porous wall was indeed sufficient to develop a strong boundary layer profile which was far from separation ( $H \approx 1.95$ ). As soon as the boundary layer reached the heated (solid) wall section, the shape factor increased dramatically and separation was encountered in a distance of less than 0.4 feet. It is interesting to note that after the suction has been restored there is still a substantial residual effect of the solid wall section as indicated by an increase in  $H$  over that before the solid wall section.

The results of using multiple heated sections are given in Figure 12. The results in this figure are for an initial 2.5 feet of suction followed by 0.1 feet of heating (solid-wall), and then by two patterns of 3 feet of suction with 0.2 feet of heating. As can be seen, the second heating pulse showed a peak shape factor of nearly 2.5 while the third heating pulse led to separation. By comparison, it is noted that an initial pulse-width of 0.2 feet followed by a second pulse of either 0.2 or 0.1 feet led to separation at the second (as opposed to the third) solid wall section.

In all these discontinuous suction studies, a distance of 0.1 foot was allowed for the suction to go from "on" to "off" or from "off" to "on". Thus, in cases where the heated section was 0.1 feet long, the suction was less than its corresponding value for the continuous suction case for a distance of 0.3 feet.

Finally, calculations for cases wherein the solid portion of the wall was left unheated showed almost no difference from these heated cases; for this body then, apparently the adverse pressure gradient is so strong that it completely dominates any favorable effects of heating.

To enhance the likelihood of stabilized laminar flow, a revised suction plus heat distribution incorporating two 0.1 foot bands of no suction with 30°F surface overheat was employed as shown in Figure 13. Resulting boundary layer calculations for this case are presented in Figure 14 which depicts shape factor, H, and skin friction coefficient,  $C_f$ , as function of the non-dimensionalized arc length, S/L. Results of detailed stability calculations for this case by Professor F. Wazzan of UCLA are given in Table 2 and show no disturbances amplifying to  $e^{-5}$  or greater up to S/L = .90.

In other words, in spite of strong trends to instability and transition (as evinced by a rapidly increasing shape factor) in regions where suction was switched off, the afterbody flow apparently remained laminar for the intermittent suction distribution of Figure 13. The effects of surface heating in regions of strong adverse gradient (as AR-3) are negligible. The distances along the AR-3 afterbody over which suction may be switched off and stability still be maintained is dependent only upon the pressure gradient and the suction rate histories. These distances are short and represent extremely small reductions in the overall afterbody suction flux.

#### B. REICHARDT BODY

A second hull with contrasting characteristics to those of the AH-8 was also chosen for this study. This is a Reichardt body of 5 to 1 fineness ratio (shown in Figure 2b). While the Reichardt shape is more practical from the point of view of enclosed packaging volume, it has a pressure gradient distribution which is less conducive to laminar flow stabilization (Figure 3). The pressure is seen to be nearly constant over the middle 70 percent of its length. Moreover, its pressure gradient becomes adverse, albeit weakly, at approximately 35 percent of length.

### 1. Forebody Region

Boundary layer calculations were performed over the forebody region of the Reichardt hull to determine a temperature distribution which would maintain stabilized laminar flow to the point of minimum pressure. The result of several iterations was a temperature distribution which rose from ambient temperature at the nose to 40°F overheat at minimum pressure ( $S/L \approx .39$ ). Details of the input data and output calculations for the final temperature distribution are given in Table 3. A plot of shape factor,  $H$ , versus arc length position,  $S/L$ , for this case, labelled "heated - No suction", is shown in Figure 15. This temperature distribution maintains the boundary layer shape factor at a nearly constant value of 2.34 over nearly 75 percent of the body, including nearly 65 percent of the adverse pressure gradient region. Stability calculations for this case show all disturbances damped to the minimum pressure location. For purposes of comparison, plots of shape factor for cases with (a) no heat or suction, and (b) no heat but small amounts of suction are shown in the same Figure. In the no heat or suction case, the shape factor passes through 2.4 at 0.05 percent of body length and remains at a value of 2.6 to 70 percent of body length. Boundary layer transition is expected when  $H$  grows larger than about 2.45. The low level of suction maintains the shape factor at a safe, low value of 2.25 to 80 percent of body length.

### 2. Afterbody Region

Similar to the approach outlined above for the AR-3 hull, three different systems: (a) heat alone, (b) suction alone, and (c) suction plus heat were employed in an attempt to extend stabilized laminar flow from the minimum pressure point into the adverse pressure gradient region. These are discussed in turn below.

#### a. Heat Alone

Extension of a 40°F overheat from the minimum pressure location into the adverse pressure gradient results in shape factor,  $H$ , and skin friction coefficient,  $C_f$ , as shown in Figure 16. Beyond an arc length position of  $S/L = 0.85$

the skin friction begins to drop rapidly and separation occurs between  $S/L = .89$  and  $S/L = .92$ . Boundary layer calculations were also run for different overheats, i.e. 0, 20, 60 and  $80^{\circ}\text{F}$ . Figure 17 presents the arc length variation of the skin friction coefficient for all five cases, and shows that differences in overheat level have negligible effect as the pressure gradient becomes increasingly adverse.

b. Suction Alone

In order to delay separation, a number of suction distributions were applied to the extreme adverse pressure gradient region of the Reichardt body. Boundary layer calculations were carried out in an effort to define an "optimum" suction distribution which would delay separation to beyond  $S/L = 0.90$ .

The shape factor for the initial region of the body was given in Figure 16. Under the influence of the nearly constant pressure gradient, the shape factor remains nearly constant at about 2.35 over the first 45 feet of the vehicle ( $S/L = 0.80$ ). Beyond this point, the pressure gradient becomes more unfavorable and the shape factor starts to increase. Details of the shape factors on this aft portion of the vehicle for the various suction distributions investigated are given in Figure 18. In the absence of suction, curve 0, the shape factor heads towards separation, but not so rapidly as for the AR-3 vehicle. The suction distributions corresponding to the shape factor histories shown in Figure 18 are illustrated in Figure 19. When the maximum suction is applied, the shape factor drops rapidly (curve 1). Note that the peak in this suction curve is the same as the one used for the AR-3 vehicle, but that the axial extent of the suction is considerably shorter. Successive reductions in the suction distribution are given by Schedules 2, 3, and 4 on Figure 19, with the corresponding changes in the shape factor distribution given on Figure 18. Each of these suction distributions is sufficient to ensure that the boundary layer remains attached, and the latter, Schedule 4, has been chosen as the "optimum" distribution since further reductions in suction lead to early separation.

c. Suction Plus Heat

As in the AR-3 calculations, this "optimum" continuous suction distribution was then made discontinuous by interspersing impermeable, heated surface sections to determine the feasibility of using surface heating to keep the boundary layer attached. Because the adverse pressure gradient on this Reichardt body is not as steep as that on the AR-3 vehicle, the lengths of the impermeable sections could be made considerably longer. The shape factor distributions for the discontinuous suction distributions are also given in Figure 18. Curve number 5 corresponds to an initial run of 2 feet of porous surface followed by an impermeable heated surface over the rest of the vehicle. (The heating used for the Reichardt body was  $\Delta T = 40^{\circ}\text{F}$ ). Following the two feet of suction, the heated surface keeps the boundary layer attached for about 3 feet before separation occurs. In curve number 6 (on Figure 19), suction was applied in two two-foot intervals separated by a 0.4 foot heated section with the entire rear surface of the vehicle again being heated. Here, separation occurred rapidly once the final heated surface was reached.

Finally, the results for a discontinuous suction distribution with two 0.4 foot intervals of heating is given on Figure 20 (labeled "hot"). The suction distribution for this case is also given on Figure 19. This last case follows the suction levels of Schedule 4 with the inclusion of the two "suction off" bands of Schedule 6. In this case, the shape factor increased slightly over the heated surfaces, but the boundary layer remained attached. The curve labeled "cold" on Figure 20 corresponds to the same suction distribution but with the heat turned off in the solid wall regions. For comparison, the continuous suction distribution is also given (lowest curve). This comparison shows that the heating does provide a measure of protection against separation on the impermeable portions of the surface for these more moderate adverse pressure gradients (compared to the AR-3), but that after a distance the history effects die out.

The suction plus heat scheme which gave the shape factor history of Figure 20 was analyzed for its corresponding boundary layer stability characteristics. The shape factor and friction coefficient for this case, designated as 1-W, have been replotted in Figure 21. The calculated stability growth factors are presented in Figure 22. This is a plot of the natural logarithm of the predicted disturbance amplitude ratios for each critical frequency investigated as a function of arc length. The term growth factor is defined as,

$$\ln \frac{\alpha}{\alpha_0}$$

and the frequency has been non-dimensionalized in the usual way; i.e.

$$w^* = \frac{wv}{U^2}$$

where w is the dimensional Tollmien-Schlichting wave frequency, v is the kinematic viscosity and U is the vehicle speed.

The growth factor is seen in Figure 22 to increase with arc length to a maximum for each of the critical frequencies. Progressing further along the body beyond the position of maximum growth factor, the waves are expected to damp and the growth factor to decrease. This aspect is not investigated by the computer boundary layer stability code, nor is it shown on the figure. These results indicate a growth factor of nearly 8 (for the non-dimensional frequency  $.125 \times 10^{-5}$ ) which is considered large enough to indicate a strong possibility of transition.

A series of modifications to this suction plus heat distribution were then made in an attempt to decrease the maximum growth factor and the probability of transition. A description of these modifications is presented in Table 4 and will be described here along with their rationale.

Case 2-W represents a modification of Case 1-W in which heat was added to the porous, suction walls of Case 1-W. Specifically, a 40°F wall overheat was applied in the regions of suction. Shape factor and skin friction coefficient histories are shown in Figure 23; corresponding growth factor histories are presented in Figure 24. Comparison to Case 1-W, Figures 21 and 22, reveals only slight-to-negligible differences between the two cases due to the addition of heat.

The most amplified disturbance frequencies for both Case 1-W and Case 2-W are seen to grow to unacceptably large, unconservative levels approaching the " $e^9$ " transition prediction level. In an effort to reduce these levels and improve the stability of the attendant boundary layer, a low level of suction was applied upstream of that for Cases 1-W and 2-W. The results for this modification, Case 3-W, are shown in Figures 25 and 26. For this configuration, disturbances at dimensional frequencies in the vicinity of  $0.1-0.15 \times 10^{-5}$  are seen to grow well above  $e^9$  near the arc length location at which suction commences. This is a rather curious result in that suction which is generally thought to be stabilizing is seen here to be destabilizing. The explanation for this observation lies in the often overlooked fact that suction, which both thins and distorts the boundary layer profile, may increase a boundary layer sensitivity to a disturbance wave. The characteristics of the most amplified disturbances are established by the thickness and shape of the boundary layer as well as by the freestream velocity. Suction, therefore, has the power to create a more unstable environment for disturbances propagating from some upstream location by essentially "tuning" the boundary layer to waves, which, without suction, would soon decay. This phenomenon is displayed in Figure 26 by the growth factor history for the disturbance wave  $w^* = 0.15 \times 10^{-6}$  which begins to flatten out at  $S/L \approx .68$  and then amplifies very rapidly near  $S/L \approx .70$  where suction is turned on.

For Case 4-W, the upstream suction levels were increased over those of Case 3-W. Figures 27 and 28 show lower shape factor, higher skin friction coefficient and reduced growth factors compared to Cases 1-W, 2-W and 3-W. Case 4-W shows particularly good stability characteristics with a maximum disturbance growth factor of less than 4. All disturbances are rapidly and effectively damped (not well displayed in the figure) in the presence of this suction distribution.

For the fifth and final iteration, the upstream suction levels were reduced to values intermediate to those of Cases 3-W and 4-W (reference Table 4). The results, displayed in Figures 29 and 30, are extremely interesting, particularly in regard to the previous comments on boundary layer "tuning" by suction. Figure 30, which presents the growth factor histories for the most amplified disturbance frequencies, gives evidence of suction's ability both to tune and to detune a boundary layer to a given disturbance wave. The disturbance  $w^* = 0.17 \times 10^{-5}$ , for example, is seen to be apparently approaching its maximum growth at  $S/L \approx .68$  only to experience a renewed, very rapid growth at the commencement of suction near  $S/L \approx .7$ . For  $S/L \gtrsim .7$ , however, the same wave suddenly begins to decay very rapidly due to detuning of the boundary layer by the specified suction distributions.

These results are re-examined in the light provided by existing analytical studies and discussed at greater depth in Section IV.

### III. HULL DRAG ANALYSIS

To provide a measure of the effectiveness of the different laminar flow stabilization schemes investigated, calculations of total hull drag were carried out. That drag should be the basis for this comparison instead of, say, cost or overall system reliability or simplicity is a moot point at the present time. Ultimately all relevant factors would have to be taken into account. However, estimates of drag are relatively simple to perform and do provide information on vehicle power requirements, which is fundamental. The results of these calculations, which are summarized below, enable a first order comparison not only among the different stabilization schemes, but also between the two hull shapes.

Several simplifying assumptions have been made. In particular, the vehicles are assumed to be without appendages such as fins or control surfaces so that only hull drag calculations need be performed. The total hull drag is assumed to be comprised of (a) wake drag, (b) drag equivalent of suction power, and (c) drag equivalent of heating power. Each drag component is expressed as a drag coefficient in the conventional manner, defined below. The total hull drag coefficient,  $C_{D_t}$ , is expressed as,

$$C_{D_t} = C_{D_w} + C_{D_s} + C_{D_h}$$

where  $C_{D_w}$  is the wake drag coefficient,  $C_{D_s}$  is the equivalent suction drag coefficient, and  $C_{D_h}$  is the equivalent heating drag coefficient.

The wake drag contribution was calculated from the momentum loss integral at the final hull station, as given by the boundary layer computer code, according to the Squire-Young formula

$$C_{D_w} = \frac{2 S_\theta}{A} \left( \frac{U}{U_\infty} \right)^{3.2}$$

Here  $U$  is the local velocity,  $U_\infty$ , is the freestream value,  $A$  is the reference area - generally taken to be the wetted hull area - and  $S_\theta$  is the toroidal area

bounded by the hull radius and the hull radius plus the boundary layer momentum thickness. A correction was applied for the non-ambient static pressure acting at the final hull station.

The equivalent suction drag coefficient,  $C_{D_s}$ , was determined from the power requirements of the suction pump. Assuming the case of a single stage suction pump, the pump power,  $P_s$ , may be expressed as,

$$P_s = Q \cdot \Delta p$$

where  $Q$  is the total volume flow rate of sucked fluid and  $\Delta p$  represents the total pressure rise through the suction system. The suction flow rate,  $Q$ , is obtained by integrating the suction velocity over the suction area. From the single stage pump assumption, the pump must be sized to provide pressure rise from the lowest local static pressure value (below ambient) on the suction surface to the freestream dynamic pressure,  $q_\infty$ , (above ambient) while additionally overcoming pressure drops through the suction skin. Experience has shown that for operational systems, skin pressure drops are generally on the order of 3% of dynamic pressure.<sup>16</sup> Ducting is assumed large enough to produce negligible pressure losses and pump efficiency (electrical to mechanical conversion) is assumed ideal. The suction pump power,  $P_s$ , is converted to a non-dimensional equivalent drag coefficient by dividing by the product of freestream velocity, dynamic pressure and wetted hull area; as,

$$C_{D_s} = \frac{P_s}{U_\infty (\frac{1}{2} \rho U_\infty^2) A}$$

The equivalent heating drag coefficient,  $C_{D_h}$ , was determined in a similar manner. Waste heat from the vehicle propulsion system was assumed to be the source of heating. Therefore, the only penalty charged against equivalent drag due to heating results from the transport and distribution system. A configuration suitable for transporting and distributing heat to the vehicle surface was proposed in Reference 15. It consists of metallic tubes (copper or nickel) which are embedded in a fiberglass vehicle inner hull and electroformed onto an

outer metallic skin and through which heating fluid is pumped. The pump power,  $P_h$ , required to distribute waste heat via this secondary fluid - heat exchanger scheme may be estimated as the product of secondary fluid volume flow rate and a fixed pressure loss.

This concept of surface heating has been investigated in detail for a vehicle shape similar to the AR-3 at Autonetics.<sup>17</sup> The vehicle surface temperature distributions and total heat transfer requirements for the contour studied are similar to those of both the AR-3 and the (5:1) Reichardt vehicles under study here. Estimates of pump power by means of required flow quantity and ducting pressure losses may, therefore, be obtained from the results of the study of Reference 17. Heating fluid flow rates on the order of 180 Lbm/sec (or 2.8 ft<sup>3</sup>/sec) and ducting pressure losses on the order of 5 psi (or 720 psf) have been shown to be adequate. Pressure losses were subsequently increased by 50 percent to account for manifolds and connections. The flow rate, pressure loss product was non-dimensionalized by the freestream velocity - dynamic pressure - wetted hull area product to generate the equivalent heating drag coefficient; as,

$$C_{Dh} = \frac{P_h}{U_\infty (\frac{1}{2} \rho U_\infty^2) A}$$

This coefficient was divided into two components relating to the forebody and afterbody heating systems. The afterbody contributions will be seen, however, to be negligible in comparison to all others.

Following these procedures, total drag estimates were made for the six most interesting cases where heat-plus-suction was applied over the vehicle afterbody. The results are summarized in the following table.

CONFIGURATION	$C_{D_w}$	$C_{D_s}$	$C_{D_h}$ (FOREBODY)	$C_{D_h}$ (AFTERBODY)	$C_{D_t}$
AR-3	$2.7 \times 10^{-5}$	$9.0 \times 10^{-5}$	$.35 \times 10^{-5}$	$1.1 \times 10^{-10}$	$12.1 \times 10^{-5}$
Reichardt (1)	$6.3 \times 10^{-5}$	$1.5 \times 10^{-5}$	$.42 \times 10^{-5}$	$1.3 \times 10^{-9}$	$8.2 \times 10^{-5}$
Reichardt (2)	$6.3 \times 10^{-5}$	$1.5 \times 10^{-5}$	$.42 \times 10^{-5}$	$1.3 \times 10^{-9}$	$8.2 \times 10^{-5}$
Reichardt (3)	$5.5 \times 10^{-5}$	$2.4 \times 10^{-5}$	$.28 \times 10^{-5}$	$1.3 \times 10^{-9}$	$8.2 \times 10^{-5}$
Reichardt (4)	$4.2 \times 10^{-5}$	$4.2 \times 10^{-5}$	$.28 \times 10^{-5}$	$1.3 \times 10^{-9}$	$8.7 \times 10^{-5}$
Reichardt (5)	$5.2 \times 10^{-5}$	$2.8 \times 10^{-5}$	$.28 \times 10^{-5}$	$1.3 \times 10^{-9}$	$8.2 \times 10^{-5}$

Under the assumption that there is no drag penalty due to heat generation, the total equivalent heating drag coefficient is apparently a very small fraction of the total hull drag coefficient. Moreover, the afterbody contribution to the total equivalent heating drag coefficient is at least five orders of magnitude smaller than the other contributions and is therefore negligible. A further observation is that for the Reichardt body, the variations in afterbody suction distribution which were investigated produced only a 5 percent change in the total hull drag coefficient. This is due to the following phenomenon: while larger suction coverage increases the equivalent suction drag coefficient, the wake drag coefficient is simultaneously decreased as the boundary layer is sucked off to diminish the net effect. Previous experience with suction systems for boundary layer control has demonstrated this phenomenon: for low suction, the latter effect dominates the former and  $C_{D_t}$  decreases as suction rate increases. For larger suction, the reverse is true; that is,  $C_{D_t}$  increases as suction rate increases. Further discussion on this interesting point is contained in the following section.

#### IV. DISCUSSIONS AND CONCLUSIONS

The effects of heating and suction may be conveniently studied on the  $Re_{\delta^*}$  - H plane, which gives a useful but approximate picture of the stability characteristics of the boundary layer. Results for the afterbody of the AR-3 body (Reference Figure 14) are plotted on Figure 31 along with the critical Reynolds number curve. All flow states to the left of the critical curve admit no growing disturbances; flow states to the right are unstable. It is expected that a flow which suffers transition by the mechanism of linear Tollmien-Schlichting waves growing ever larger will have a trajectory on the  $Re_{\delta^*}$  - H plane which extends to the right of the critical curve. The trajectory for the AR-3 body begins at the minimum pressure point and proceeds as indicated by the arrows through the suction (to lower H) and heating (to higher H) regions. As suction is applied, the boundary layer moves away from the critical curve, but returns rapidly toward it when the first heating pulse (no suction) is applied. After the suction has once more made the boundary layer strongly stable, the second heating pulse forces the boundary layer into the unstable range. For the continuous suction case, the boundary layer remains well below the critical  $Re_{\delta^*}$  curve, indicating that the suction distribution selected is sufficient to prevent transition (and separation).

The Reichardt body, Case 1-W, fares considerably worse according to this  $Re_{\delta^*}$  - H plane representation (see Figure 32). Shortly downstream of minimum pressure, the boundary layer becomes unstable and moves continuously further from the critical line. The applied suction draws it back towards the stable region, and, even in this discontinuous case eventually stabilizes the boundary layer. In order to keep this body laminar, indications are that the suction would have to be applied much earlier in the constant shape factor region near the front of the body. This was demonstrated in Section II by test Cases 3-W, 4-W and 5-W. Whether or not a reasonable amount of suction near the front of the body would keep the boundary layer stable over the entire (almost) constant-pressure region is not clear from this presentation. What is quite clear are the trends of a boundary layer trajectory on this plane under the action of either suction or heating. Suction is apparently capable of shifting the trajectory to much lower values of H and

increased boundary layer stability. Practical amounts of heating, on the other hand, for the levels of pressure gradient encountered with the two bodies under study here are much less effective in this regard. These calculations and observations suggest that the relative effectiveness of the two mechanisms can be monitored by trajectory changes in the  $Re_{\delta^*}$  - H plane.

Further insight is provided by a detailed investigation of the boundary layer velocity profile and its second derivative. These, in fact, represent the boundary layer as input into the linear stability analysis. Of particular interest is the evolution of the velocity and second derivative profiles in a region where suction is being turned off and heating is being turned on. Four stations through such a region have been selected on the afterbody of the AR-3 body, located by number on Figure 12. Velocity profiles for Station 1, which is in a suction-only region, and for Station 3, which is in a heat-only region are displayed in Figure 33. The former is seen to be fuller and thinner than the latter, which reflects both lower H and increased stability for the suction over the heated boundary layer. Thinner, more energetic boundary layers are at once more stable and better able to negotiate adverse pressure gradients.

The second derivative profiles for the four stations are plotted on Figure 34. As suction is switched off and heating is switched on, the second derivative profile is seen to suffer a zero crossing just before Station 3. Rayleigh's Theory and experience have demonstrated that a zero crossing in the second derivative profile (which corresponds to an inflection point in the velocity profile) signals the onset of instability within the flow. The boundary layer, therefore, goes unstable in passing from the region of suction to that of heating in this adverse pressure gradient. The width of the heated or no suction region must be less than the distance for instability to develop into transition. That this is so has been demonstrated by detailed stability calculations for the same case, which indicate that transition does not occur.

Another presentation which adds insight into the mechanisms of suction and heating and their effectiveness in an adverse pressure gradient was considered by Aroesty and Berger (Reference 10). In an approximate analysis of (for Falkner-Skan water flows) suction and heating in the control of laminar separation, they were able to develop relationships which indicate the level of heating and/or suction required to delay separation in an adverse pressure gradient. Their results (their Figures 3 and 4) are included here for reference in Figure 35. These plots represent the minimum amount of heating or suction necessary to maintain an attached laminar boundary layer in an adverse pressure gradient. Points to the right (below the curves) represent separated and to the left (above) represent unseparated flows. At a length Reynolds number of  $250 \times 10^6$ , a  $40^{\circ}\text{F}$  surface overheat has about the same effectiveness in delaying laminar separation as a level of suction  $v_w/U_\infty = 0.006 \times 10^{-3}$ ! Thus, surface heating is predicted to be of limited utility and of greatly reduced effectiveness in delaying laminar separation, as compared to suction. The same general conclusions can be drawn concerning heating and suction and transition.

The suction parameter vs  $\beta$  trajectory for the afterbodies of the AR-3 (reference Figure 13) and the Reichardt, Case 1-W (reference Figure 9) have been plotted in Figure 36. Also plotted is the separation-limit curve of Figure 35 (from Reference 11). Ignoring the downward spikes which correspond to the heated, no suction regions, these plots illustrate that the suction levels which delay transition for both the AR-3 and Reichardt bodies are consistent with those predicted for delay of separation. It is tempting to investigate the existence of a transition-limit curve in this plane which would indicate the minimum levels of suction which would delay transition for a given adverse pressure gradient. Such an investigation is, unfortunately, beyond the scope of the present study. A similar thought led to the construction of the transition Reynolds number curve in the  $Re_{\delta^*}$  vs  $H$  plane (reference Section II and Figure 5).

Falkner-Skan  $\beta$  and skin friction coefficient are plotted as a function of non-dimensional arc length  $S/L$  for the AR-3 and Reichardt (Case 1-W) bodies on Figures 37 and 38, respectively. The downward spikes in  $C_f$  denote the heated, no suction regions of the afterbody. The results of Figure 35 (from Reference 11) indicate that a wall overheat of  $90^0F$  would be required to keep a laminar boundary layer attached for a  $\beta$  of -0.3. Figure 36 shows that the  $\beta$ 's in the regions of the heated, no suction afterbody strips on the AR-3 body are on the order of -2.0 to -5.0. Such a flow is clearly on its way to separation with negligible help from the applied overheat of  $30^0F$ . The situation is somewhat improved for the Reichardt body, Figure 38, where  $\beta$  in the heated strips is seen to be on the order of -0.2 to -1.0. There is, therefore, some chance of a little help from surface heating, for sufficiently large  $\Delta T$ , in the initial region of the Reichardt vehicle afterbody. These statements which are predicated on results for laminar separation rather than for transition are entirely consistent with the previous discussions and conclusions based on study of the boundary layer trajectory in the  $Re_{\delta^*} - H$  plane.

In summary, the use of surface heating in the afterbody region of the AR-3 or Reichardt (5:1 fineness ratio) vehicles is clearly from very minimal to absolutely zero utility for transition suppression. There is some hope for heating in adverse pressure gradients small compared to those typical of vehicle afterbody regions. Boundary layer calculations and stability analyses performed in the present study indicate the effectiveness of suction for transition (and separation) suppression in an adverse pressure field. These results are in agreement with the limited (approximate) existing theoretical analyses and with intuition. Moreover, the suction field need not be continuously distributed in order to effectively delay transition. Interruptions in the suction distribution which are short compared to the distances necessary for small disturbances to grow sufficiently larger to cause transition are permissible. The width of such interruptions as well as the distribution of suction intensity before and after an interruption must be carefully analyzed.

The  $Re_{\delta^*}$  - H plane representation provides a useful, convenient and inexpensive but approximate means of assessing the effectiveness of an intermittent suction field. The ultimate assessment, however, lies in detailed analysis of the boundary layer stability characteristics. This is especially so because of the ability of suction to "tune" and "detune" a boundary layer to specific disturbance frequencies by modifying the boundary layer thickness and velocity profile. While suction is apparently capable of stabilizing any laminar boundary layer flow, the required suction flow rates and/or flow distributions may become impractical.

As the suction flow rates increase, so does the cost in terms of equivalent drag or energy consumption to provide the suction flow. This point is illustrated in Figure 39, taken from Reference 18 for an 8:1 Reichardt body in air, which shows wake drag coefficient, equivalent suction drag coefficient and overall drag coefficient\* as a function of suction flow rate. The equivalent suction drag is seen to overtake the gains realized by means of suction in wake drag; the overall drag coefficient which decreases for lower levels of suction, increases for higher levels. This point is also illustrated by the calculations and results of Section III.

Comparing the tabulated results of wake drag, equivalent suction drag and overall drag coefficients for the two vehicles, the overall drag for the AR-3 is seen to be larger than that for the Reichardt body. The wake drag for the AR-3 is considerably smaller than that for the Reichardt body. The difference is clearly due to the larger equivalent suction drag for the AR-3. In other words, the higher levels of suction required to stabilize the AR-3 afterbody as compared to the Reichardt afterbody correspond to a higher drag, inspite of the corresponding reduction in wake drag. These factors need to be taken into account by engineers and designers seeking to find practical applications for laminar flow vehicles.

---

\*These coefficients are defined in Section III.

The objective of this report was to present the results of a study of the stabilizing effects of surface heating and suction in the afterbody region of two specific vehicles. The utility of suction in this regard was clearly demonstrated. Before further progress can be made in this area, some little understood but important aspects of the problem, which emerged during the present study, need to be investigated. These include:

1. A study of the relationship between level of suction, the Falker-Skan  $\beta$  parameter and transition leading to a "transition curve" similar to the "separation-limit curve" on Figure 35.
2. A detailed study of the mechanism whereby a boundary layer under the action of suction may be "tuned" or "detuned" to disturbance waves.

and finally,

3. A thorough, parametric study of the optimization of suction, for delay both of transition and of separation, on laminar vehicle afterbodies. Both continuous and discontinuous suction distributions need to be investigated to insure the most stable laminar flow. Further optimization in terms of total drag (as described herein) would lead to fully hydrodynamically optimized vehicle designs.

Experience has shown that these will best be approached by careful theoretical analysis guided and supported by detailed laboratory experiments.

## REFERENCES

1. B. H. Carmichael, "Underwater Vehicle Drag Reduction Through Choice of Shape," Paper No. 66-657, presented at AIAA Second Propulsion Joint Specialist Conference, Colorado Springs, June 1966. Also published in Underwater Missile Propulsion, (L. Greiner, ed.), Compass Publications, Arlington, Virginia, 1967, pp. 147-169.
2. A. R. Wazzan, T. T. Okamura, and A.M.O. Smith, "The Stability and Transition of Heated and Cooled Incompressible Laminar Boundary Layers," Fourth Int. Heat Transf. Conf., Vol. III, Paper FC-14, 1970.
3. A. J. Strazisar, J. M. Prahl, and E. Reshotko, "Experimental Study of the Stability of Heated Laminar Boundary Layers in Water," Case Western Reserve University, Department of Fluid, Thermal, and Aerospace Sciences, FTAS/TR-75-113, September 1975.
4. H. Schlichting, Boundary Layer Theory, 6th ed., McGraw Hill Book Company New York, 1968, pp. 444-447.
5. F. E. Gentry, "The Transitional Analysis Program System User's Manual - Volumes I and II," prepared for Naval Sea Systems Command (PMS 395) by McDonnell Douglas Corporation, Long Beach, California
6. L. Rosenhead, Laminar Boundary Layers, Oxford Press, London, 1963, pp. 540-548.
7. W. S. King, Low-Speed Boundary Layer Transition Workshop, The Rand Corporation, R-1752-ARPA, June 1975.
8. S. Barker, "High Reynolds Number Transition Experiments in a Heated Flow Tube," Autonetics Group of Rockwell International, to be published.
9. W. S. King, "The Effects of Wall Temperature and Suction on Laminar Boundary Stability," The Rand Corporation, No. R-1863-ARPA, April 1976.
10. J. Aroesty and S. A. Berger, "Controlling the Separation of Laminar Boundary Layers in Water: Heating and Suction," The Rand Corporation, R-1789-ARPA, September 1975.
11. C. Gazley, Jr., "The Combined Effects of Pressure Gradient and Heating for Boundary Layer Stability and Transition," Proc. Low-Speed Boundary Layer Workshop II", The Rand Corporation, Santa Monica, September 1976.
12. R. J. Hansen and R. A. Skop, "A Design Methodology for Submersibles with Extended Laminar Boundary Layers," Proc. Low-Speed Boundary Layer Workshop II, September 1976.

13. R. S. Scotti, et al, "Design of a Laminar Flow, Low-Drag Research Vehicle", Proc. Low-Speed Boundary Layer Workshop II, September 1976.
14. J. S. Parsons, R. E. Goodson, "The Optimum Shaping of Axisymmetric Bodies for Minimum Drag in Incompressible Flow," Purdue University Report ACC-72-5, AD 744314, 1972.
15. Autonetics Report #C75-857/301, "High Reynolds Number, Heat Stabilized, Laminar Boundary Layer Experiment Final Report," September 1975.
16. B. H. Carmichael and K. H. Rogers, Autonetics Group of Rockwell International, private conversations.
17. R. T. Tobin, "Large Laminar Flow Vehicle Surface Temperature Control," Rockwell International, IL No. ASR76-267, November 17, 1976.
18. L. W. Gross, "Experimental and Theoretical Investigation of a Reichardt Body of Revolution with Low-Drag Suction in the NASA Ames 12-Foot Pressure Wind Tunnel," Northrop Report BLC-148, July 1963.

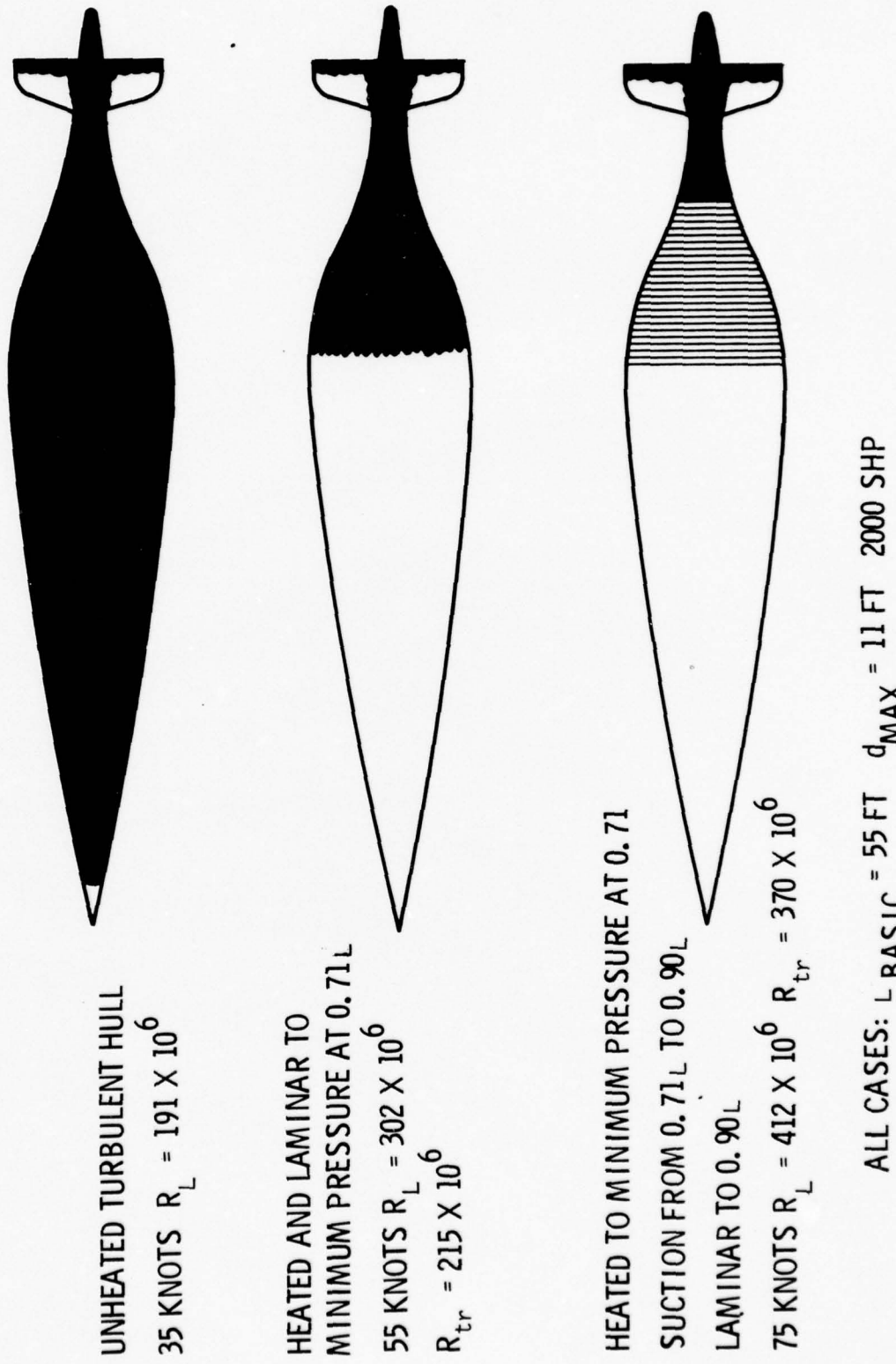
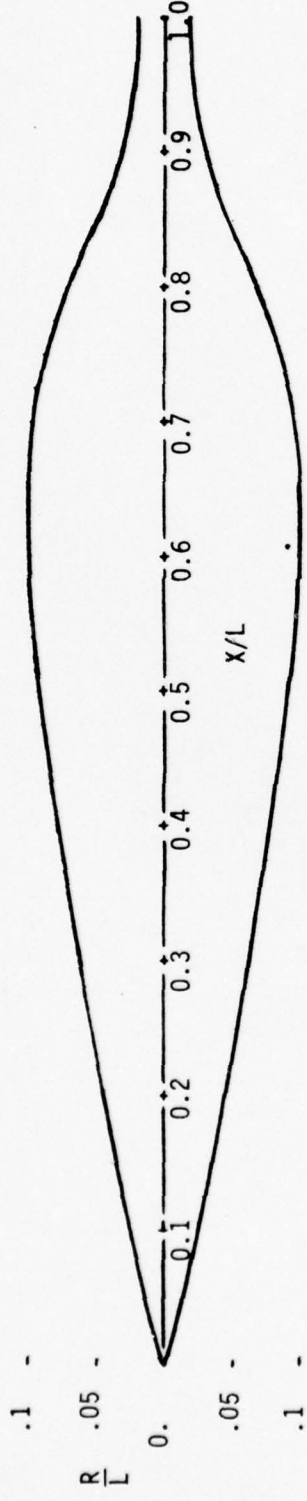
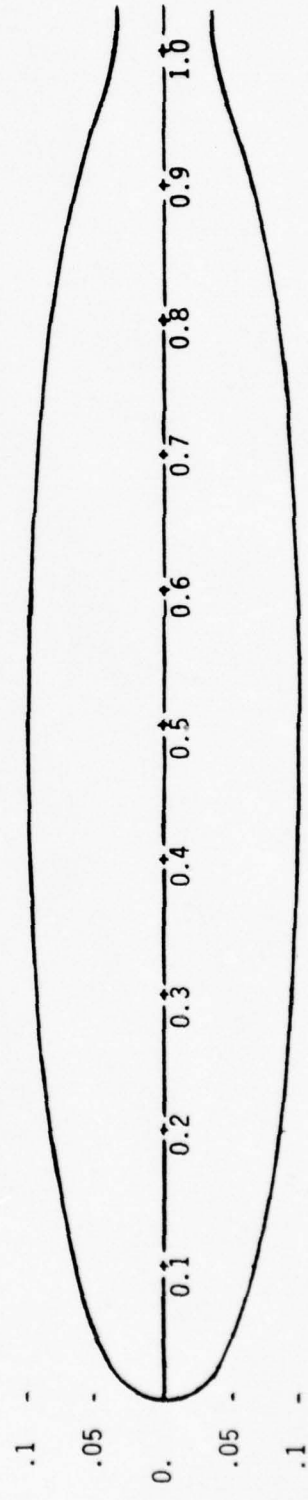


Figure 1. The Effects of Geometry, Heat, and Heat Plus Suction on Vehicle Performance



(a) AR-3 Body Shape, 5:1 Fineness Ratio



(b) Reichardt Body Shape, 5:1 Fineness Ratio

Figure 2. Body Shape Comparison

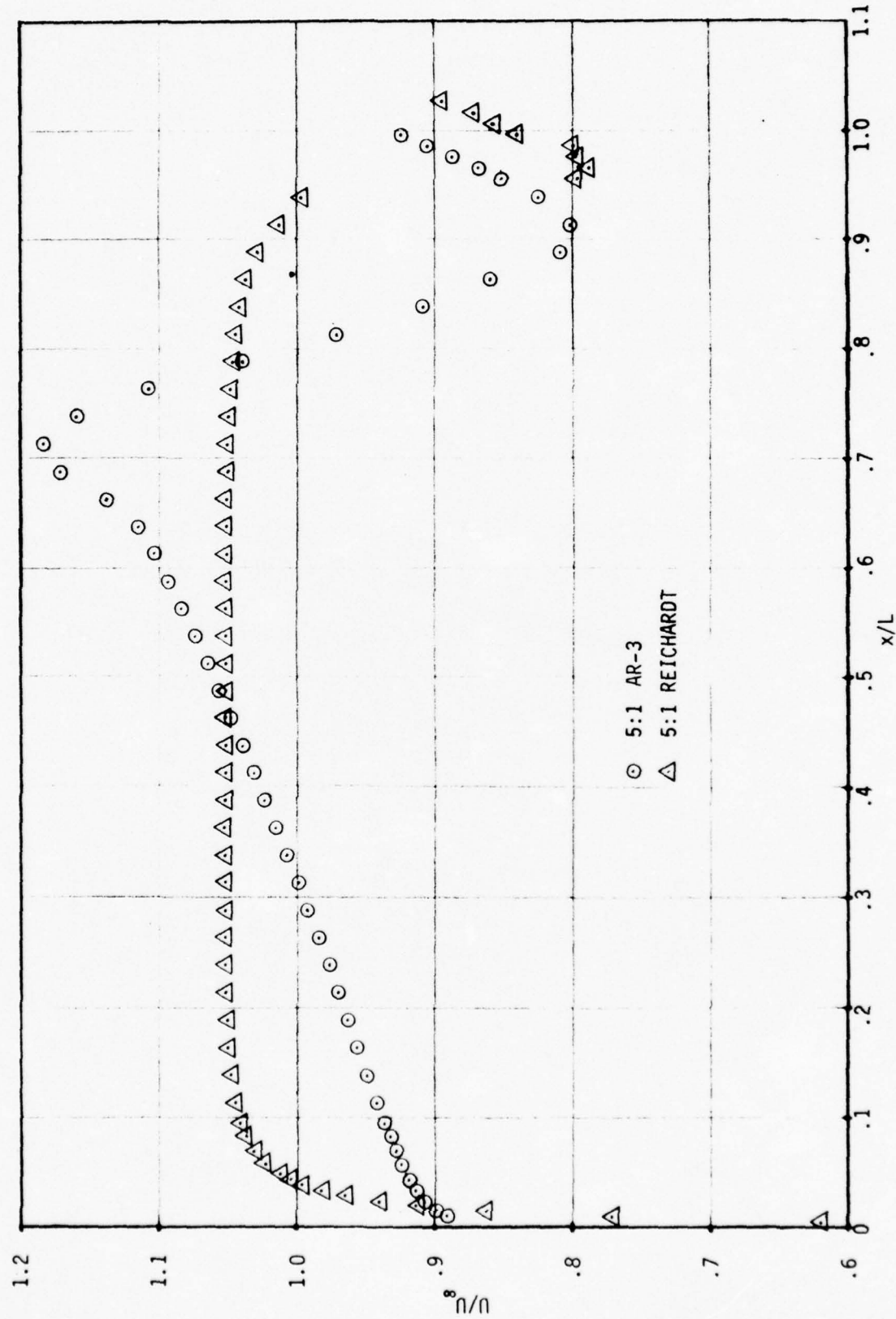


Figure 3. Potential Flow Velocity Distributions for 5:1 Rechardt and AR-3 Shapes

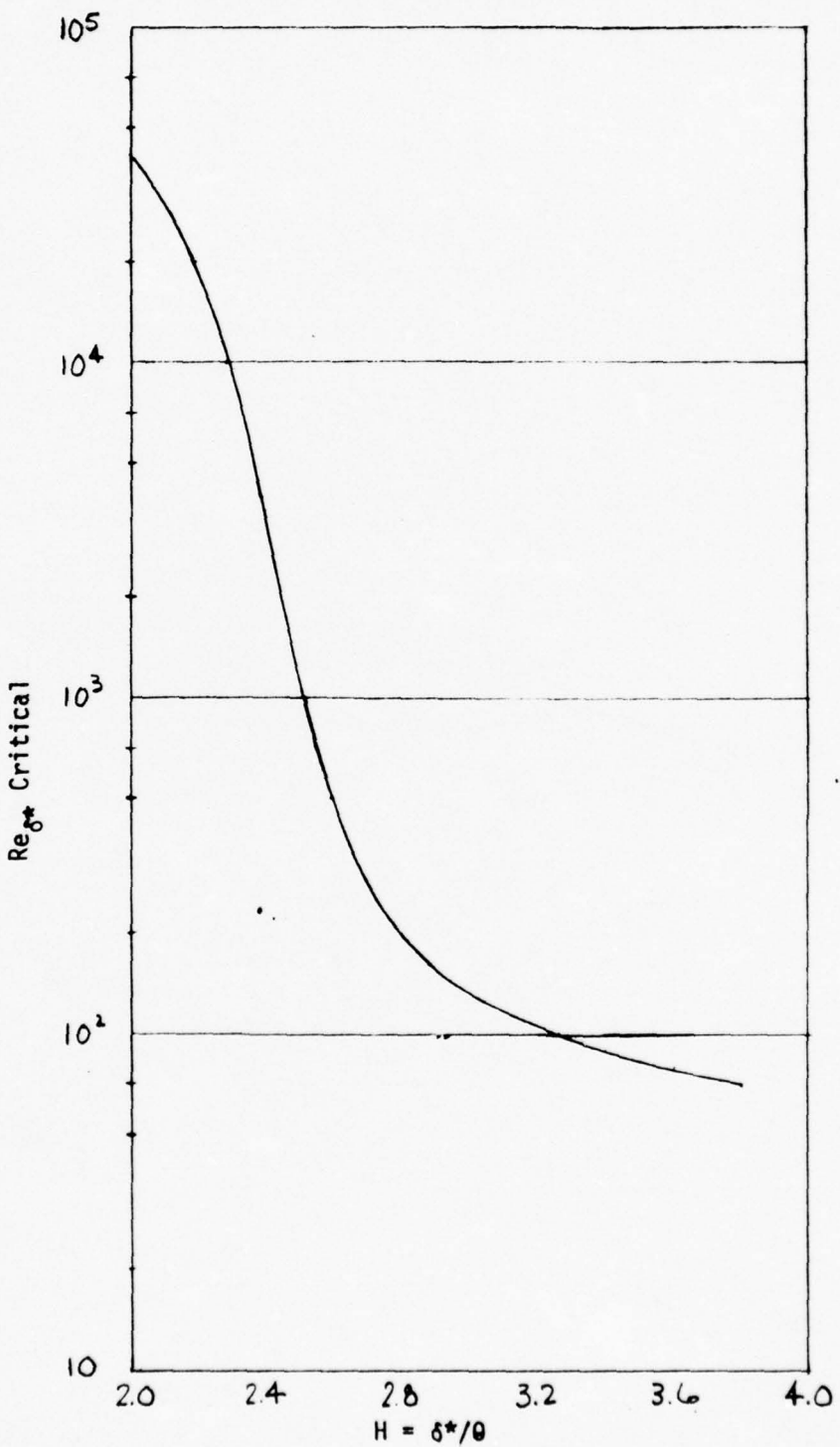


Figure 4. Critical Reynolds Number vs Shape Factor

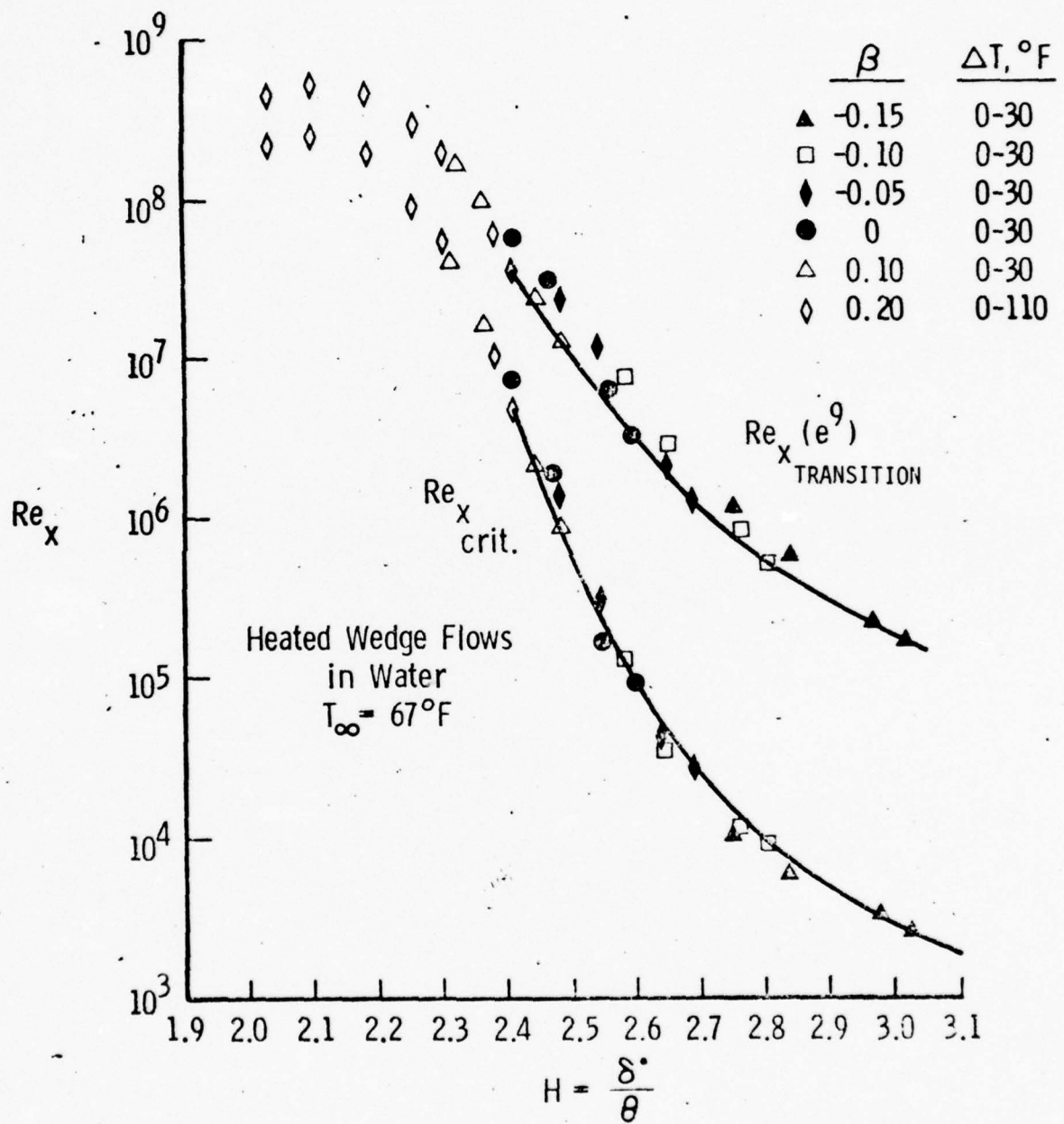


Figure 5. Critical and Transitional Reynolds Numbers  
 (Based on "e<sup>9</sup>") vs. Shape Factor  
 (from Reference 11)

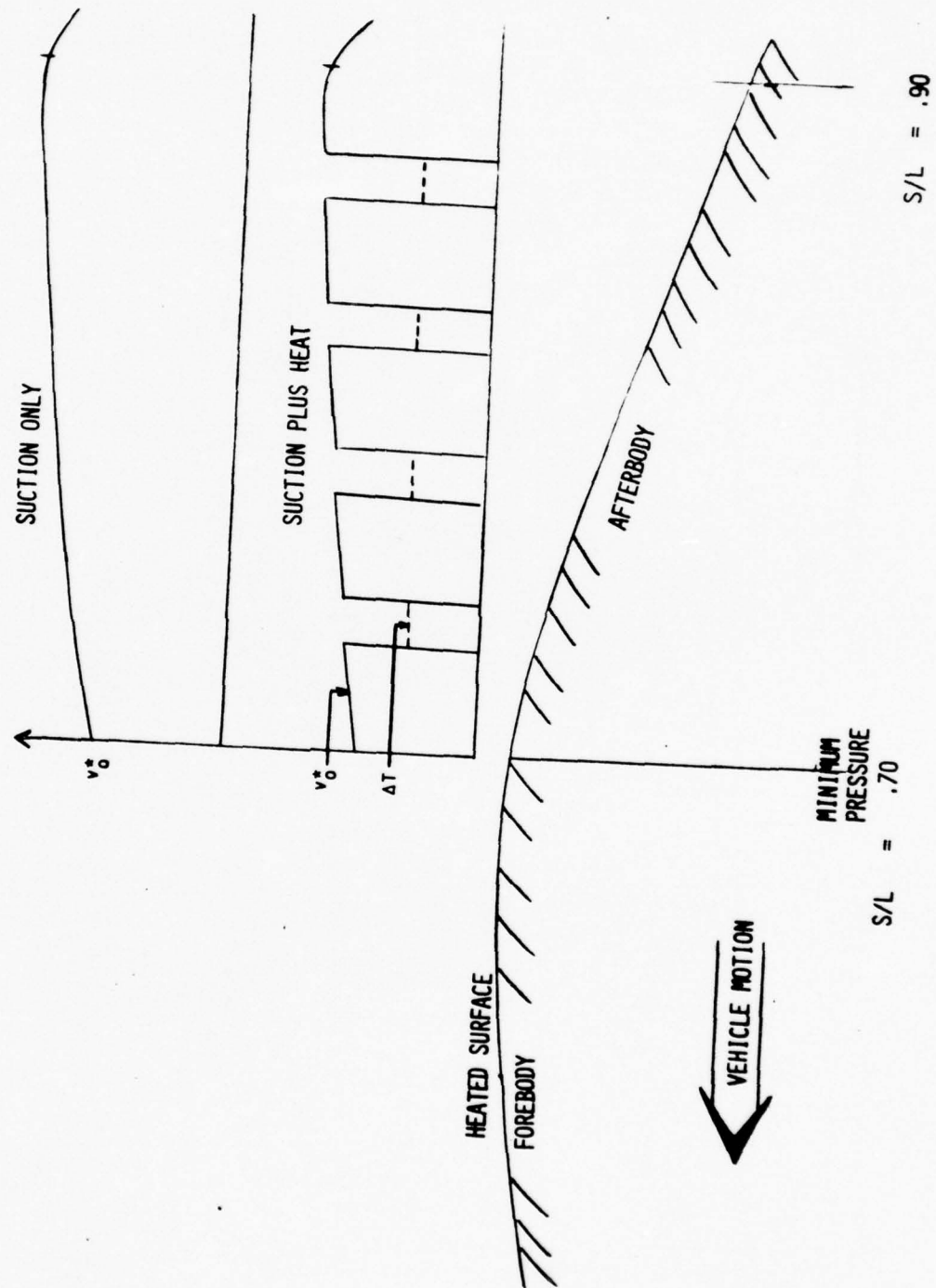


Figure 6. Schematic of Afterbody Suction  
Plus Heating

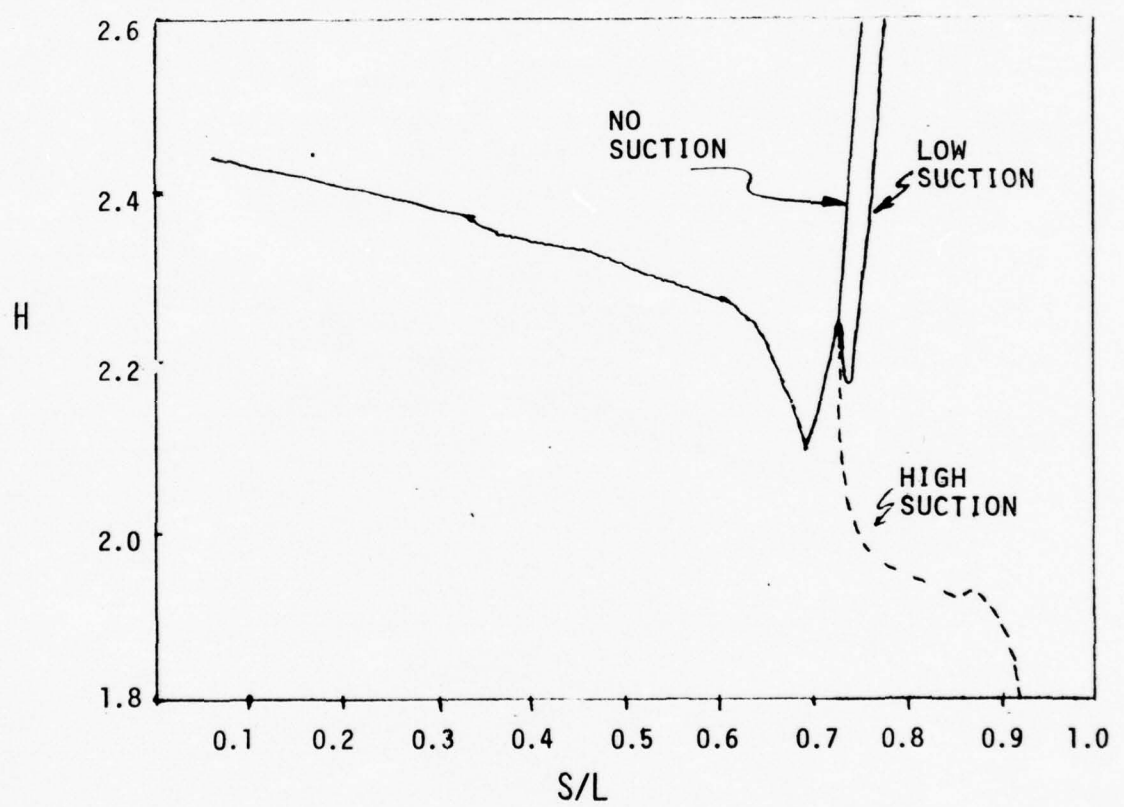


Figure 7.  $H$  vs  $S/L$  for AR-3 (reference Table 1)

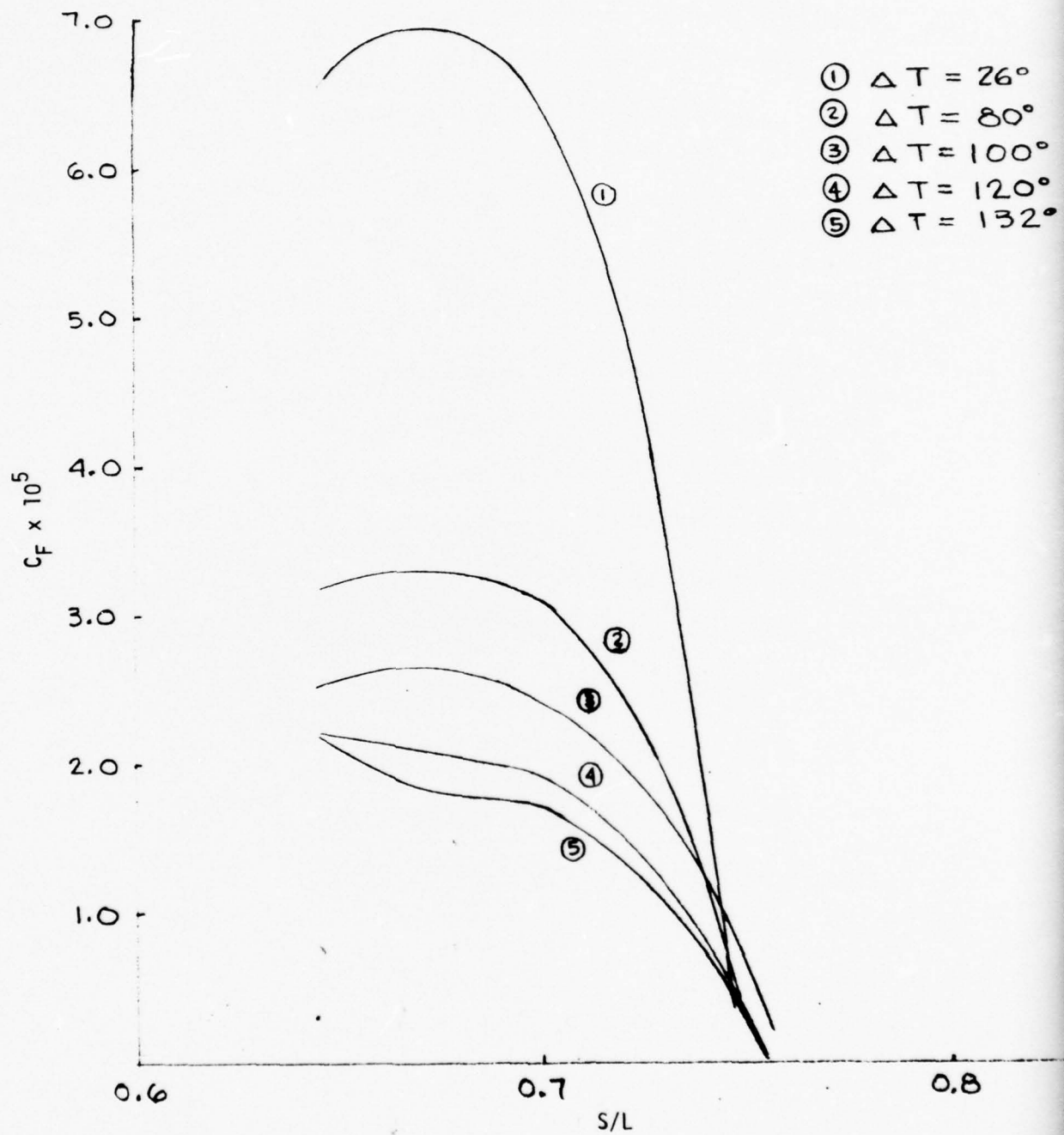


Figure 8. Skin Friction Coefficient vs S/L for the Afterbody Region of AR-3 for Several Surface Overheats

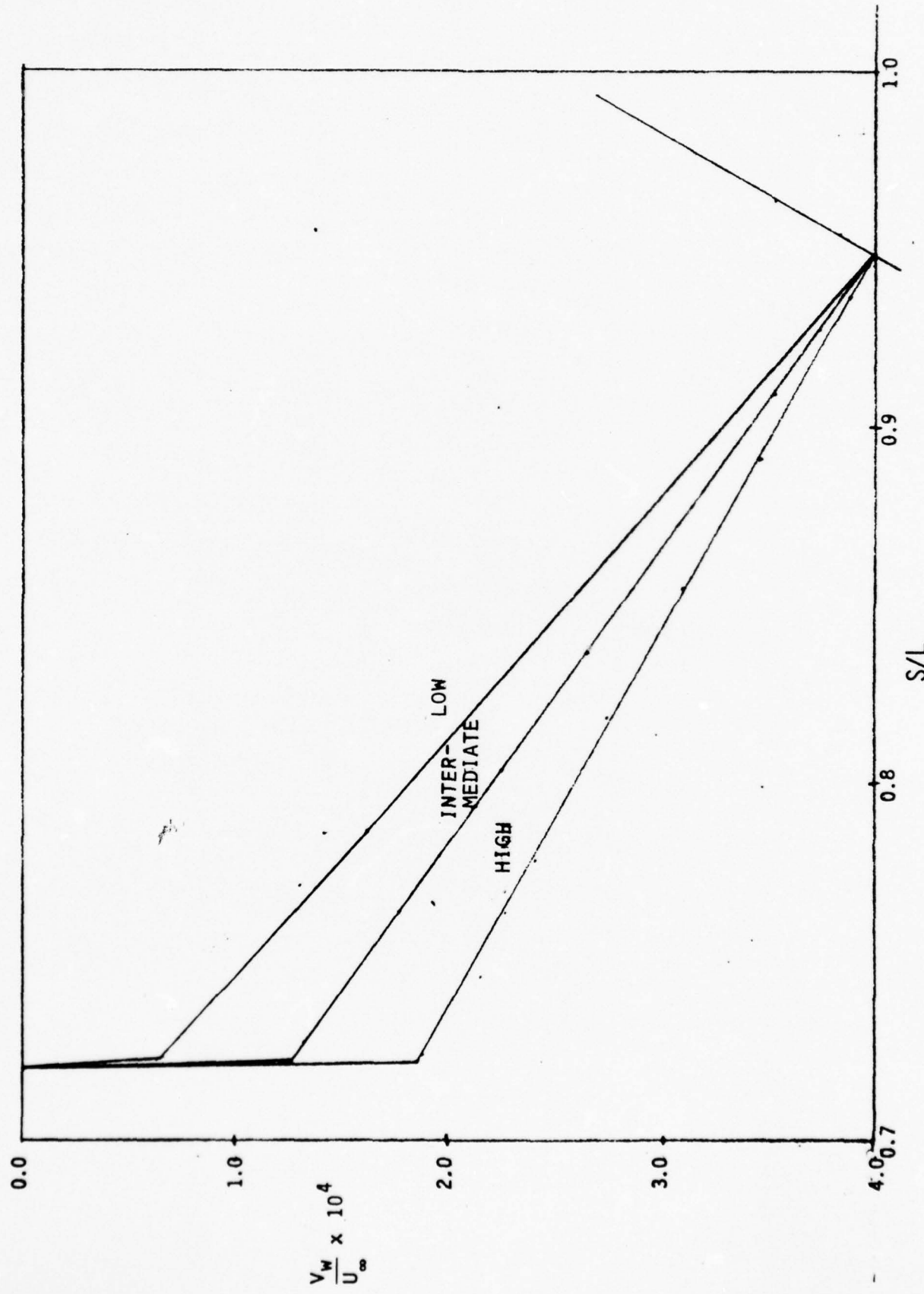


Figure 9. Afterbody Suction Distributions (AR-3)

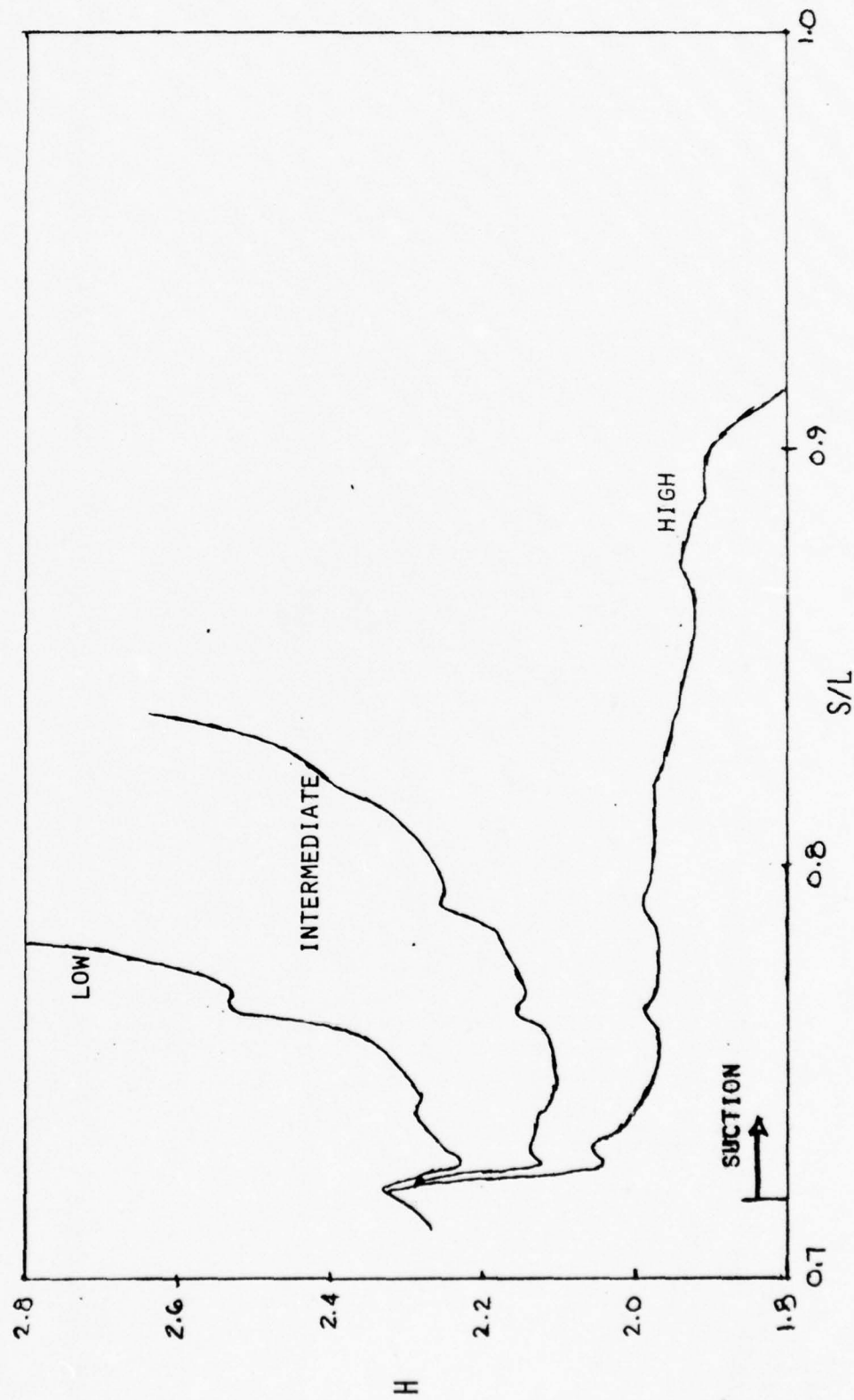


Figure 10. Continuous Suction Cold Wall,  $\Delta T = 0$   
(after Figure 9)

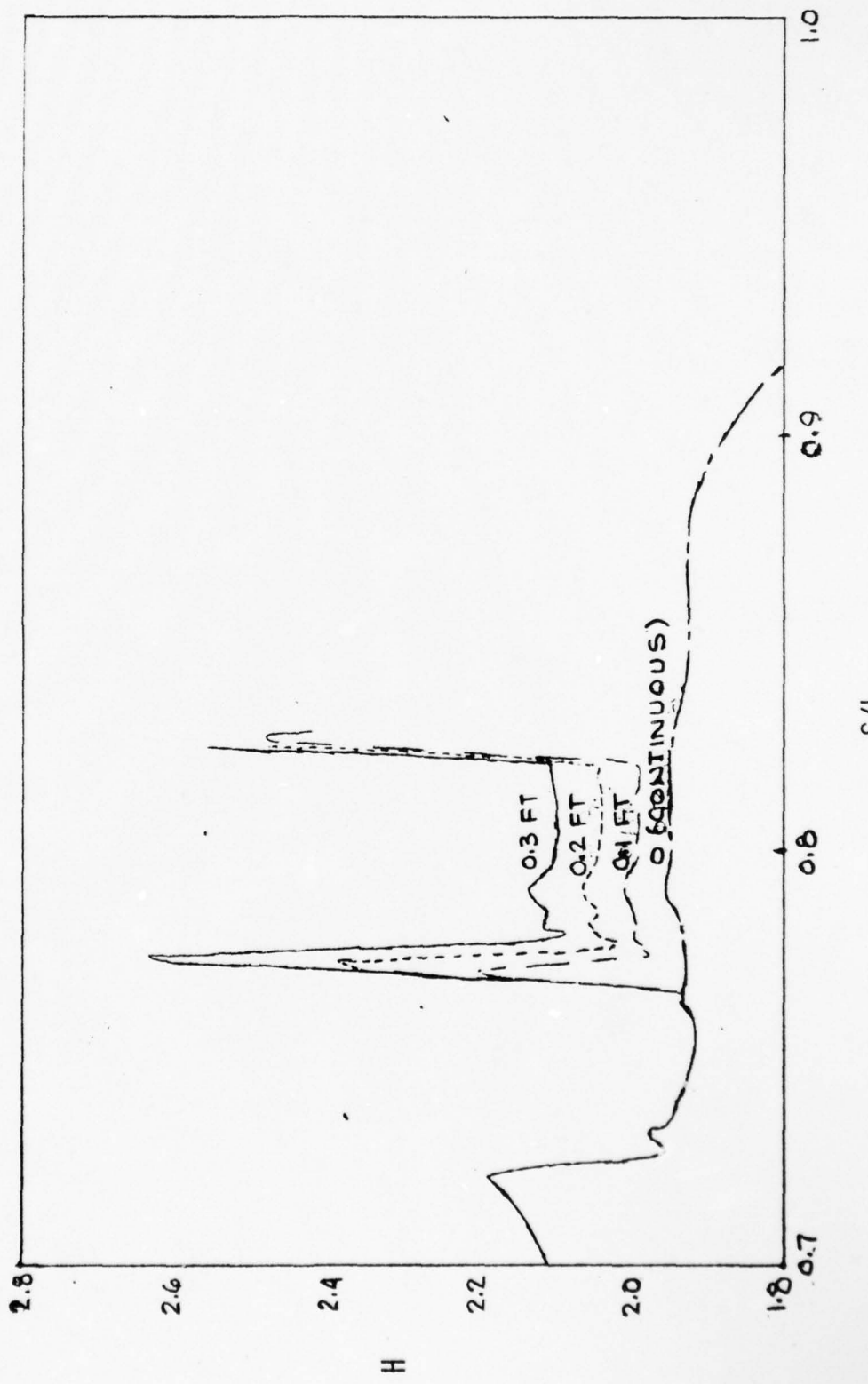


Figure 11. Discontinuous Suction - The Effects of Varying Width of Heating (AR-3)

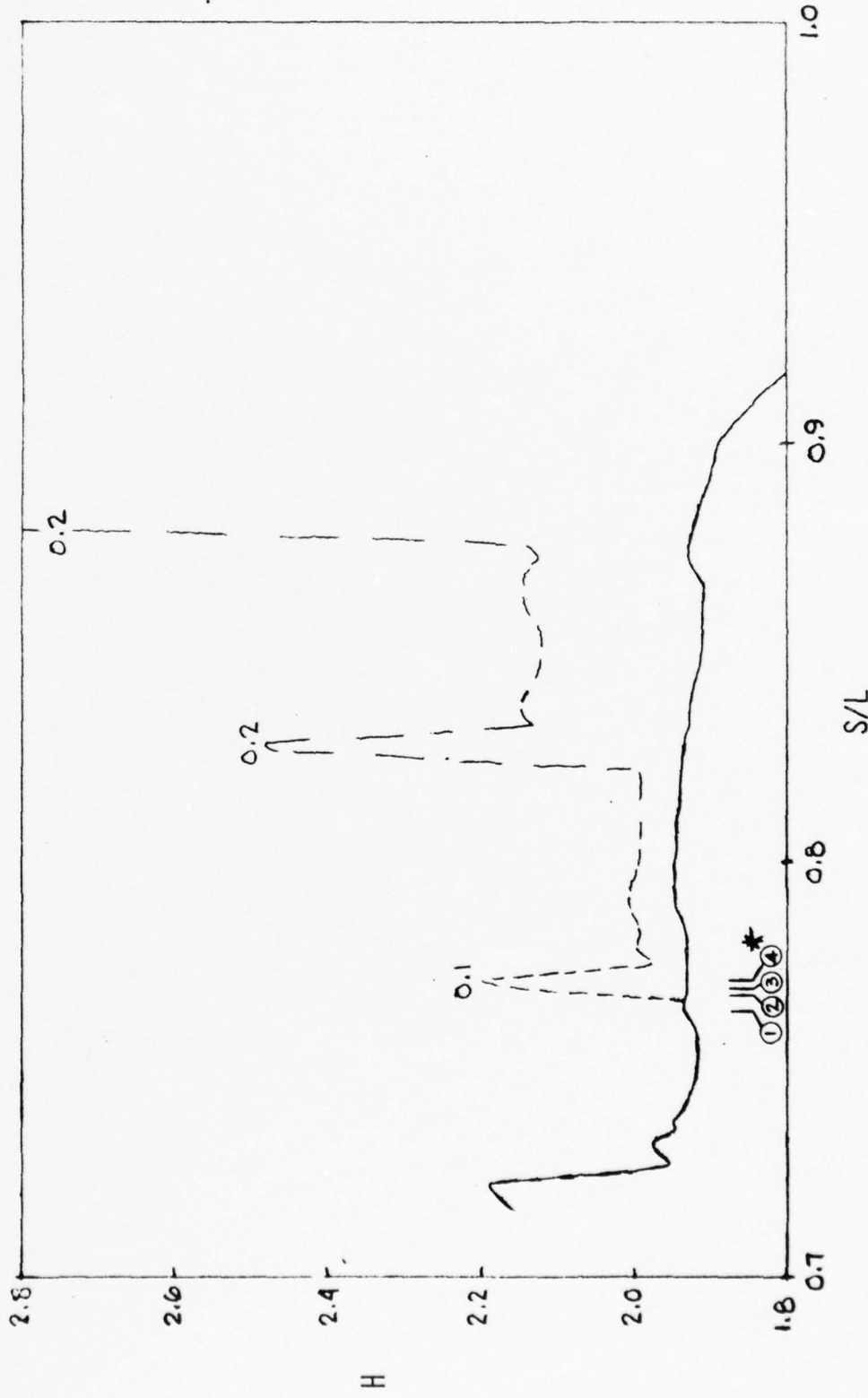


Figure 12. Discontinuous and Continuous Suction High Value,  $\Delta T = 35^{\circ}\text{F}$   
 (Reference Page 27 and Figures 33 and 34)

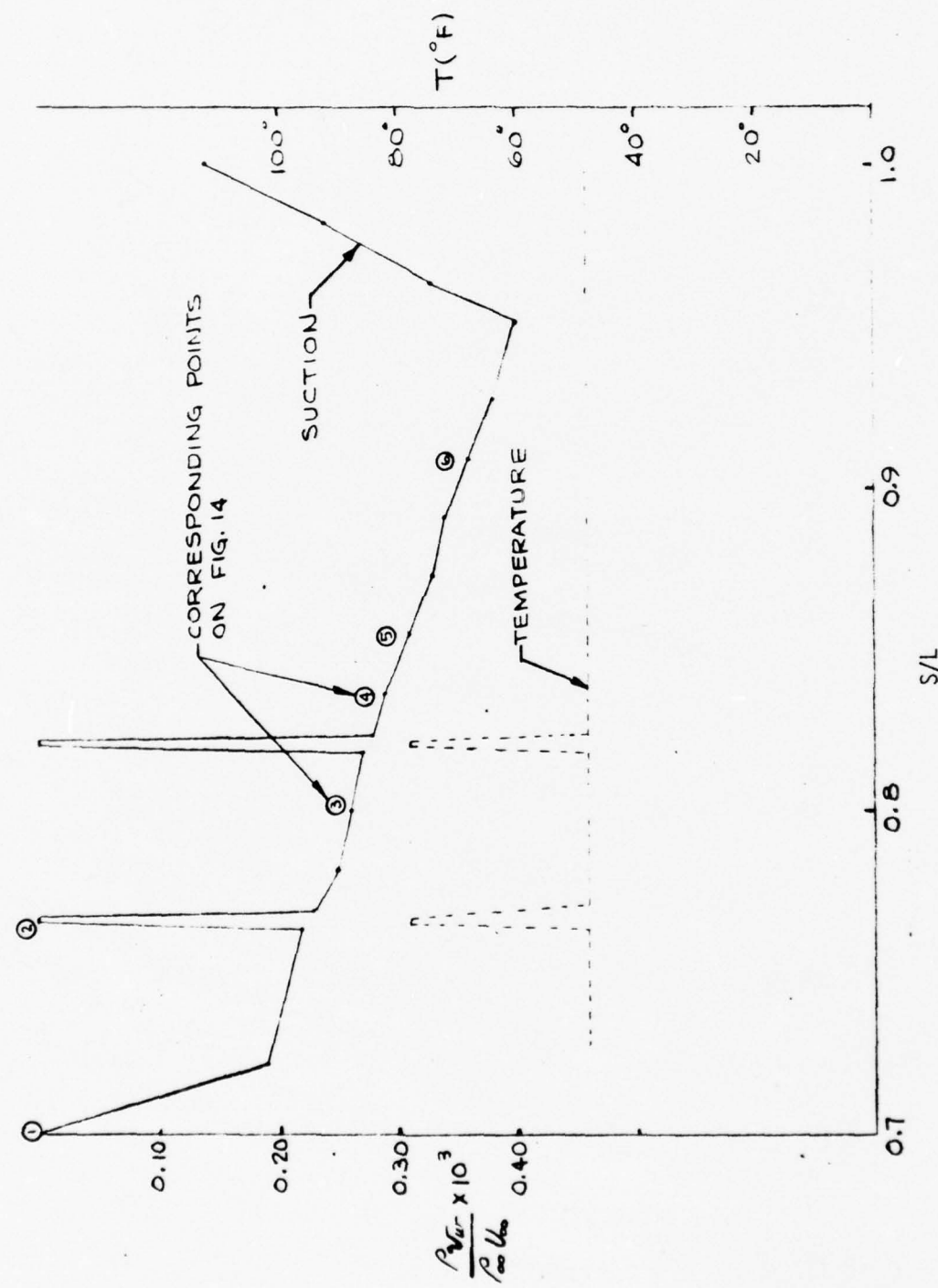


Figure 13. Suction and Temperature Distributions on Afterbody of AR-3

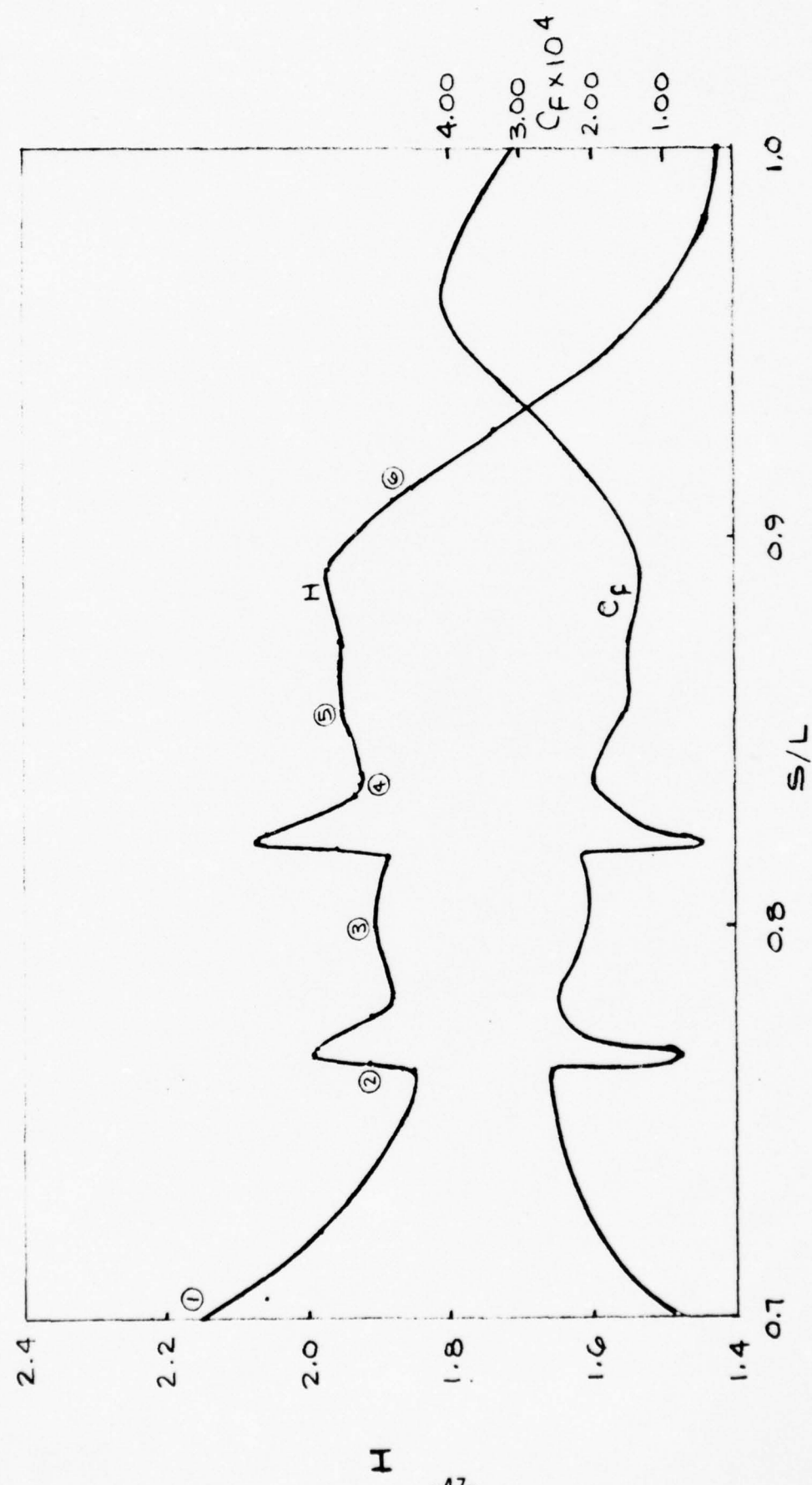


Figure 14. Shape Factor and Friction Coefficient Histories Corresponding to Suction and Heating shown in Figure 13

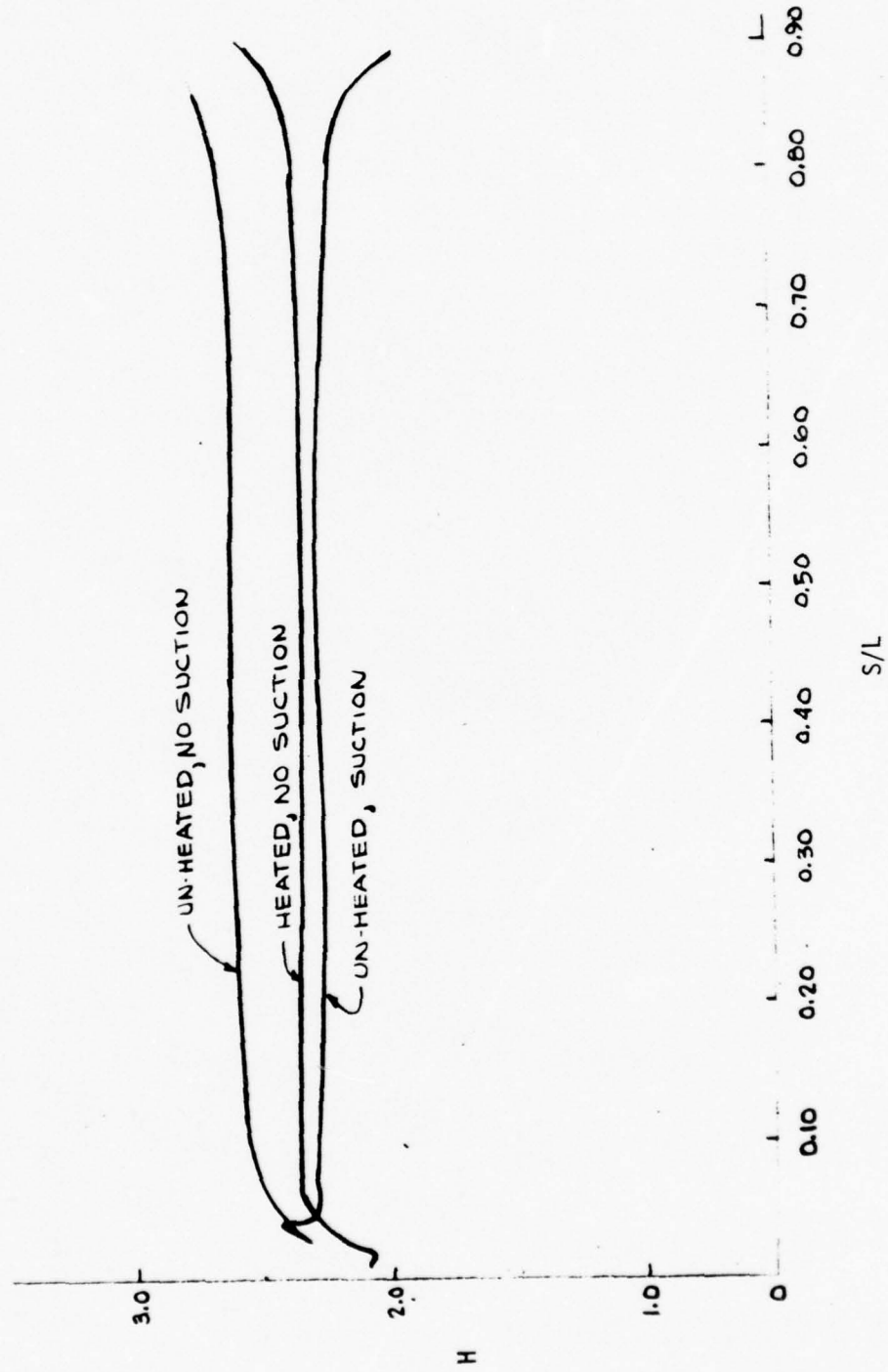


Figure 15. Shape Factor vs Distance (Reichardt Body)

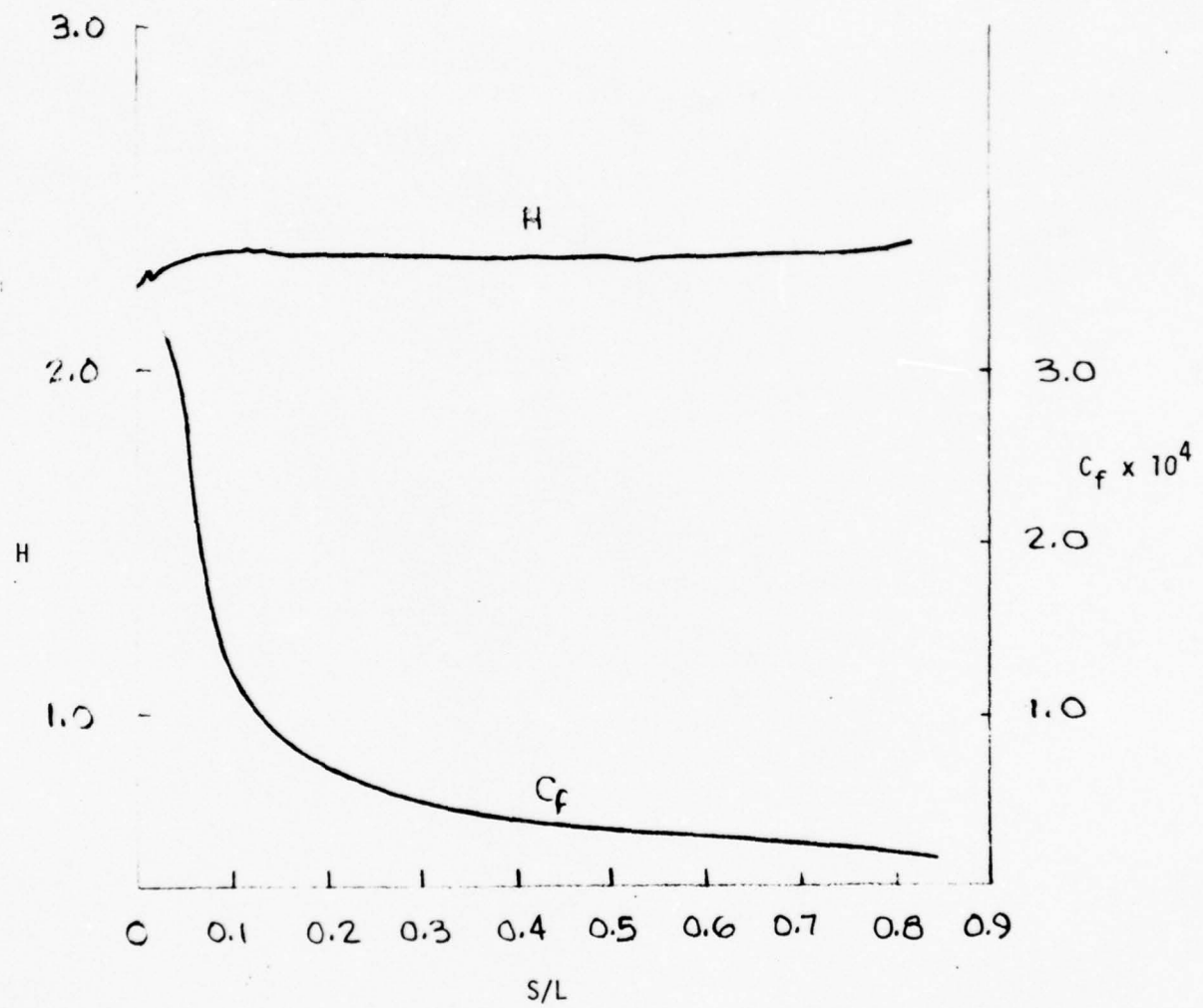


Figure 16. Shape Factor and Friction Coefficient vs. S/L  
(Reichardt Body,  $\Delta T = 40^\circ F$ )

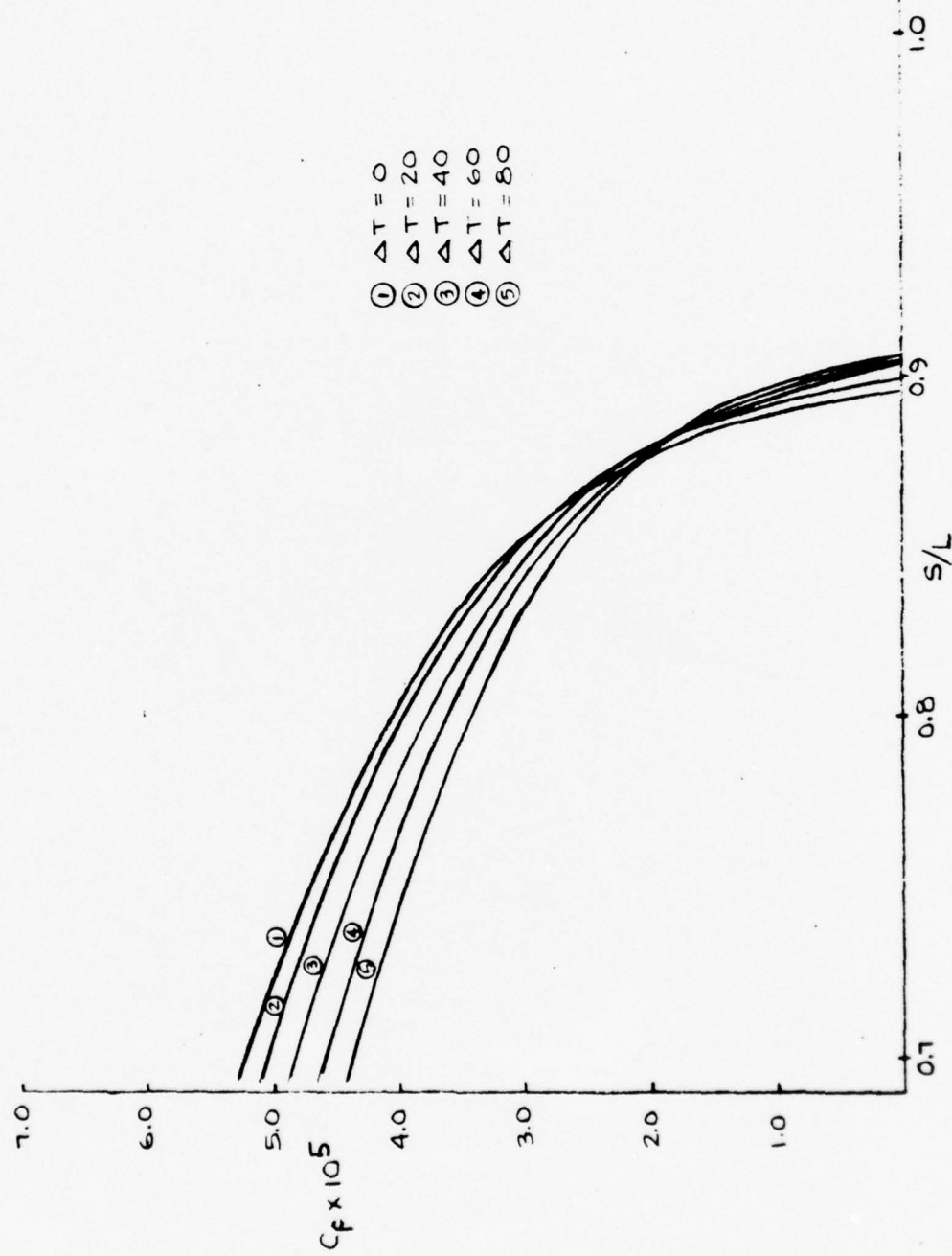


Figure 17. Skin Friction Coefficient vs.  $S/L$  for the Afterbody Region of the Reichardt Body for Several Overheats

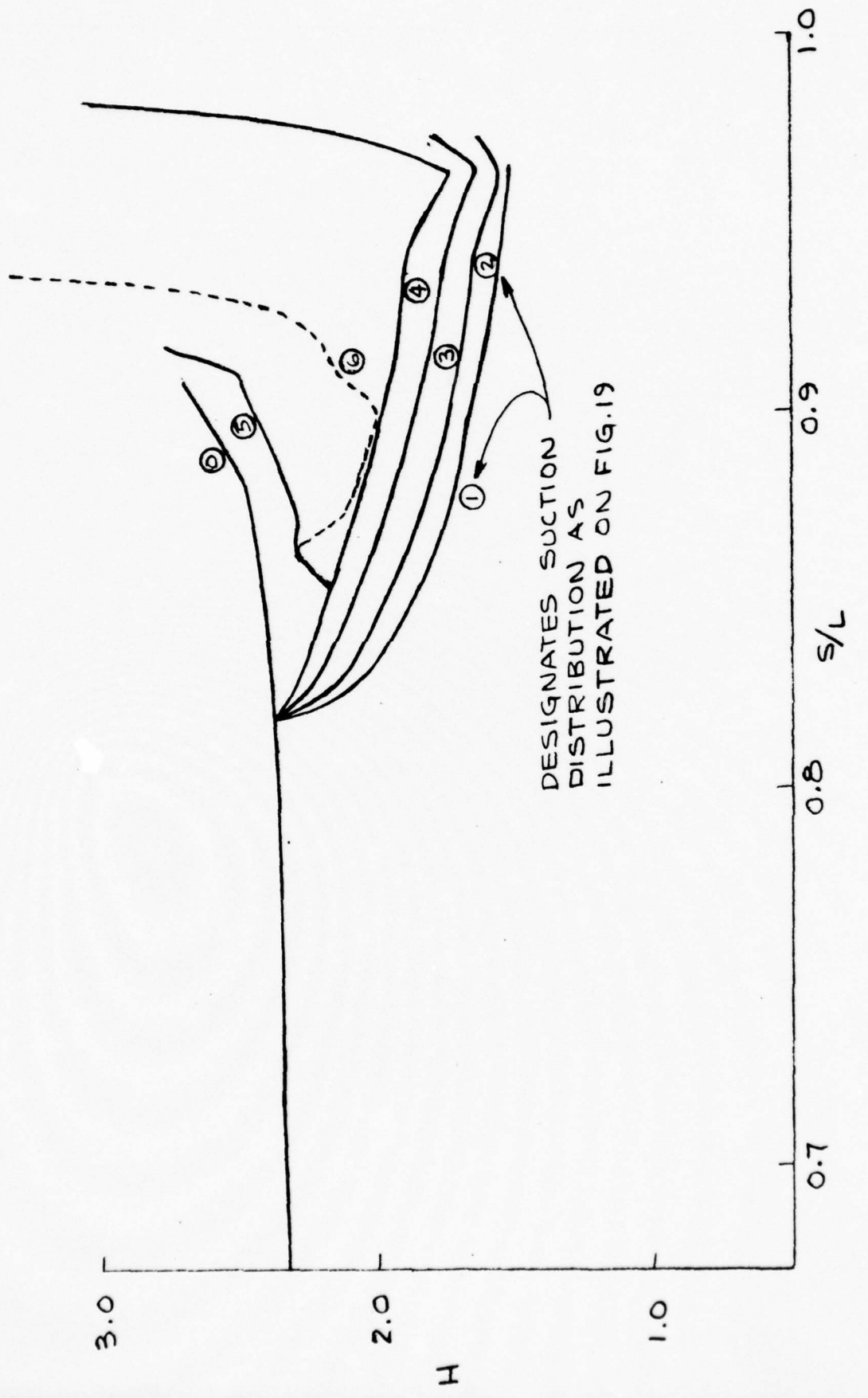


Figure 18. Shape Factor vs.  $S/L$  (Reichardt Body - Various Suction Distributions)

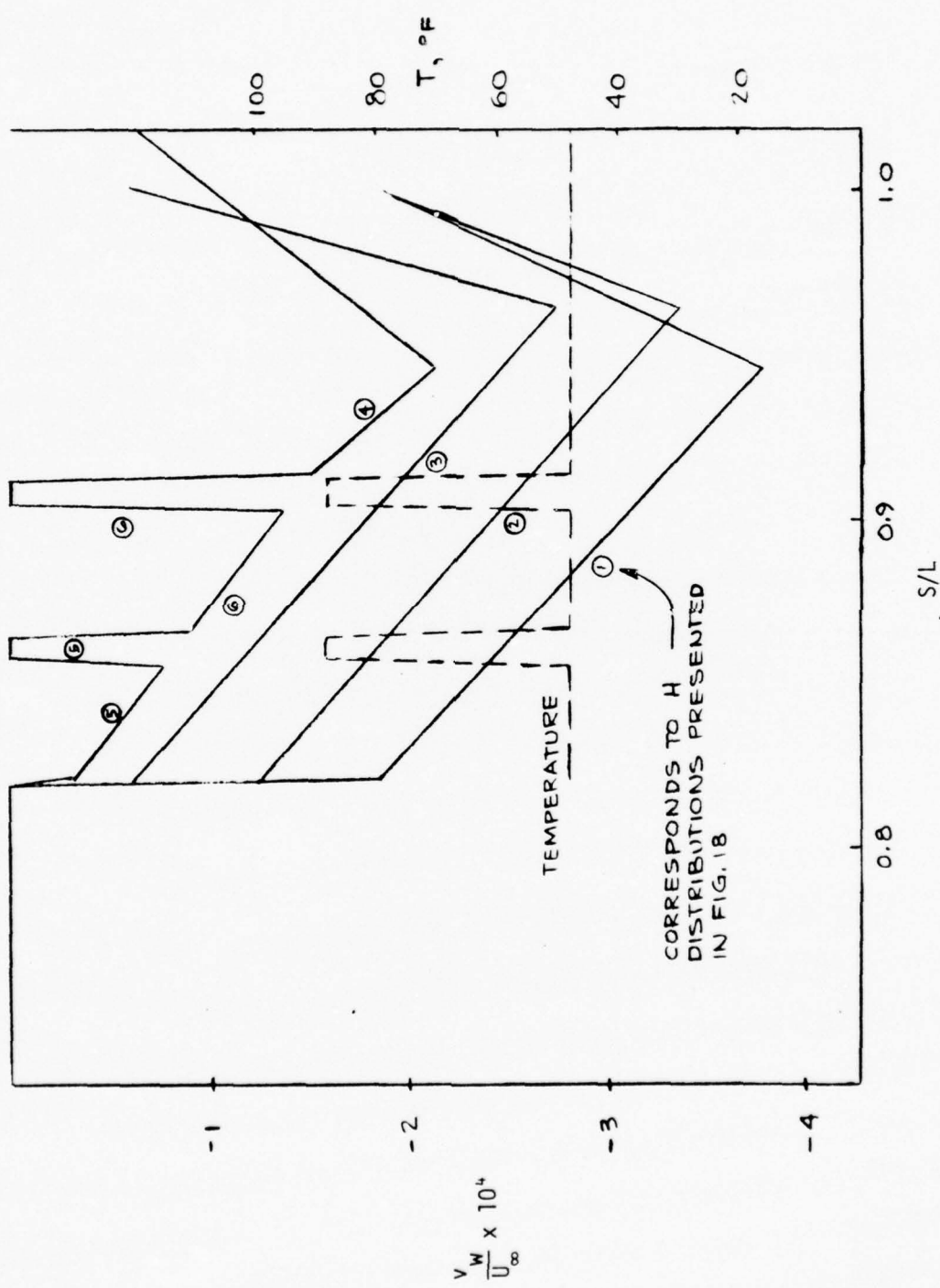


Figure 19. Suction and Temperature Distributions Investigated on the Reichardt Body

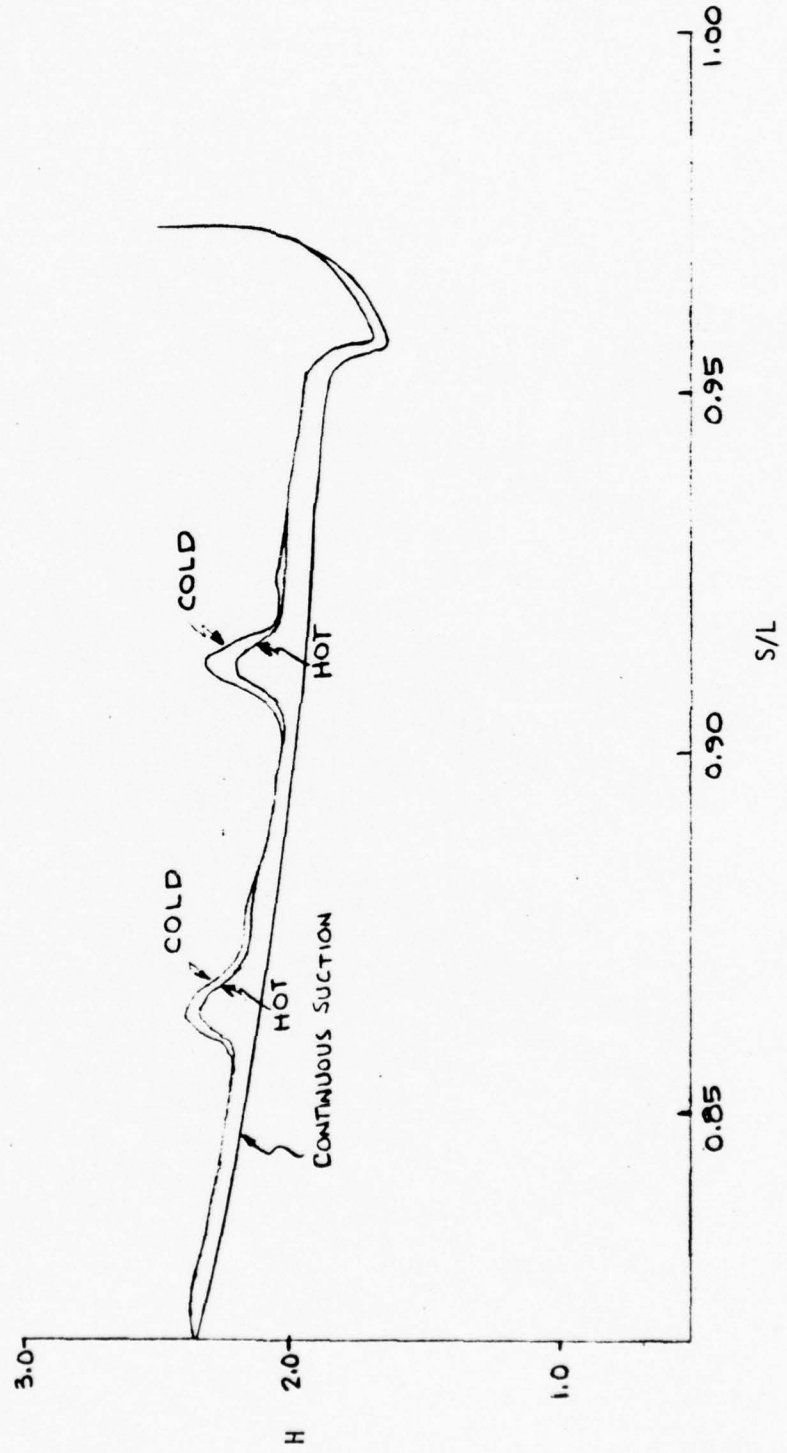


Figure 20. Effects of Surface Heating on Shape Factor in Presence of Unfavorable  $dp/dx$   
(Reichhardt Body)

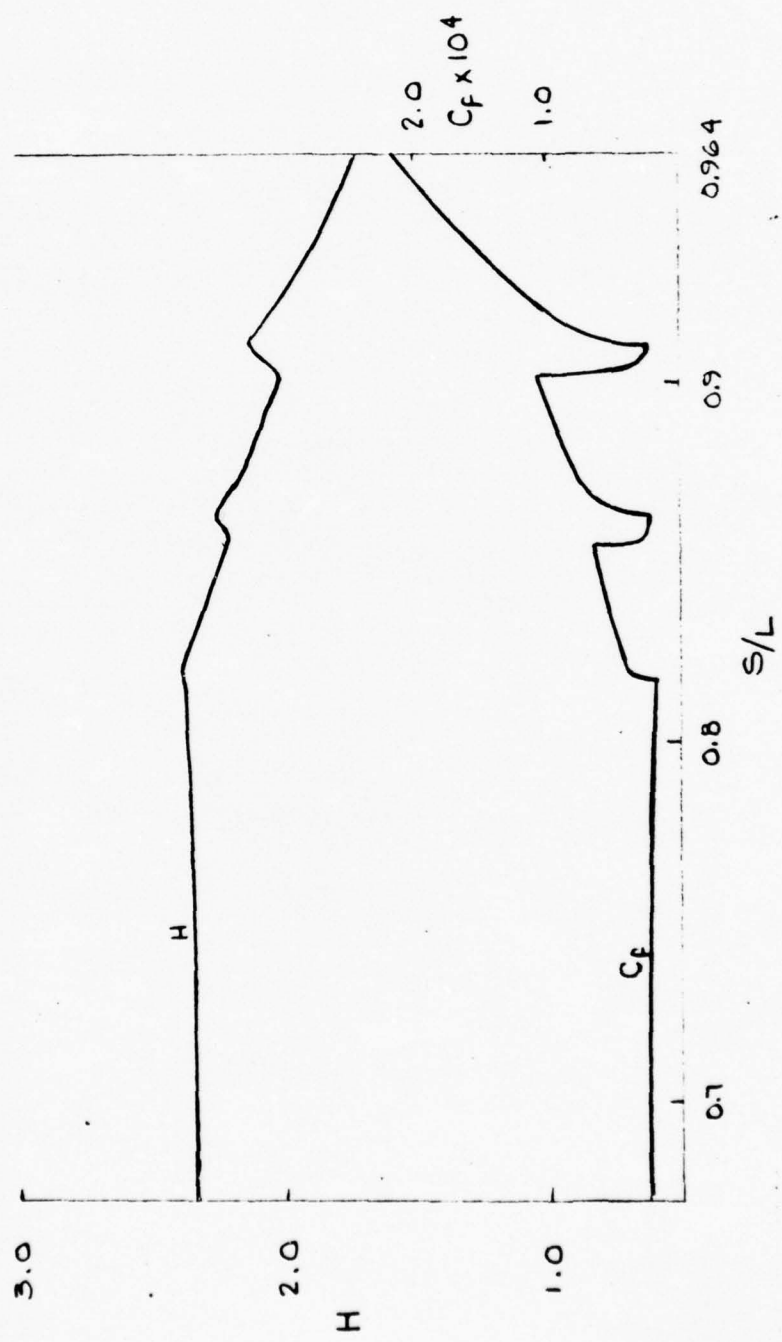


Figure 21. Shape Factor and Friction Coefficient vs.  $S/L$  (Reichardt Body, Case 1-W)

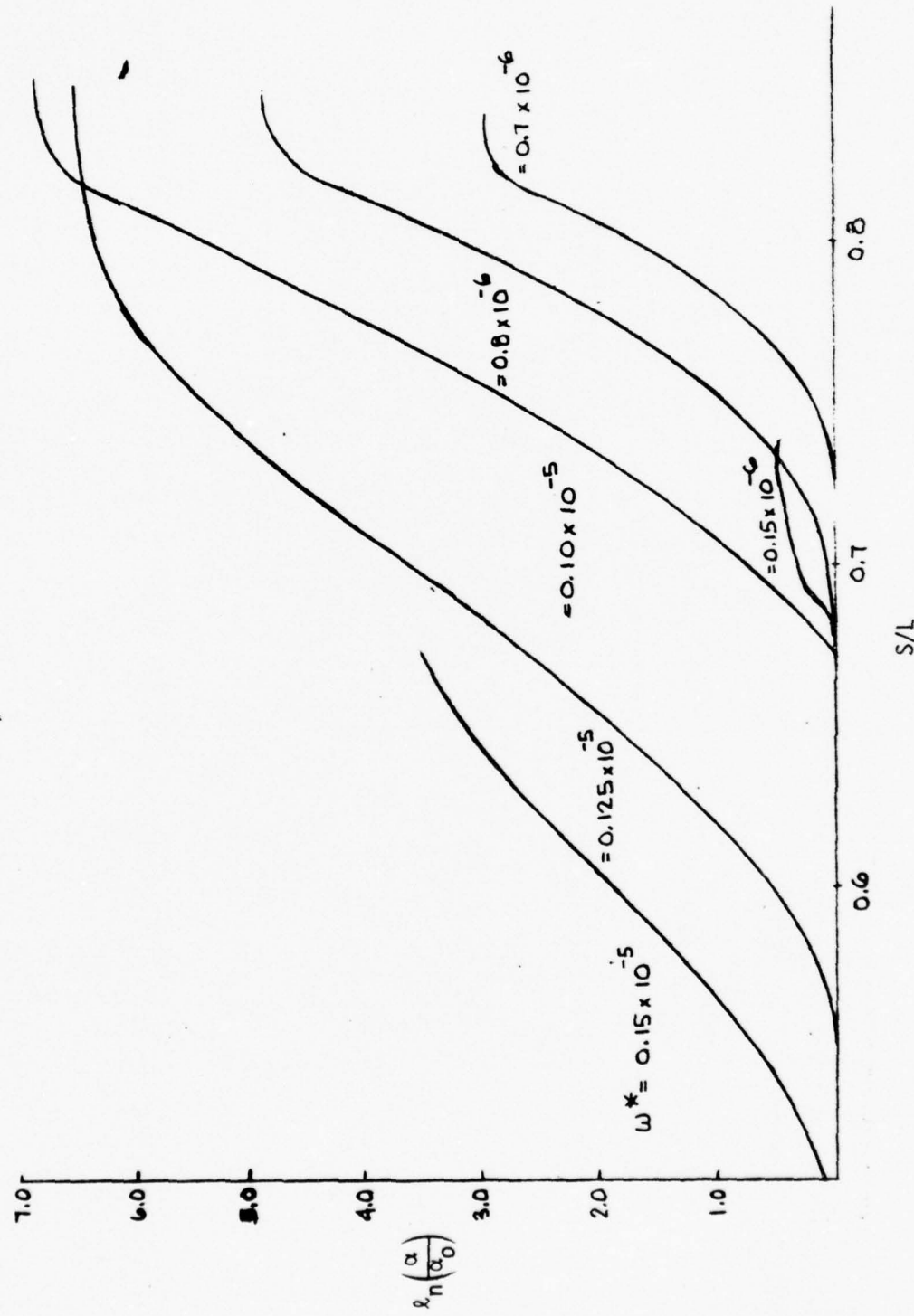


Figure 22. Stability Growth Factors for Reichardt, Case 1-W

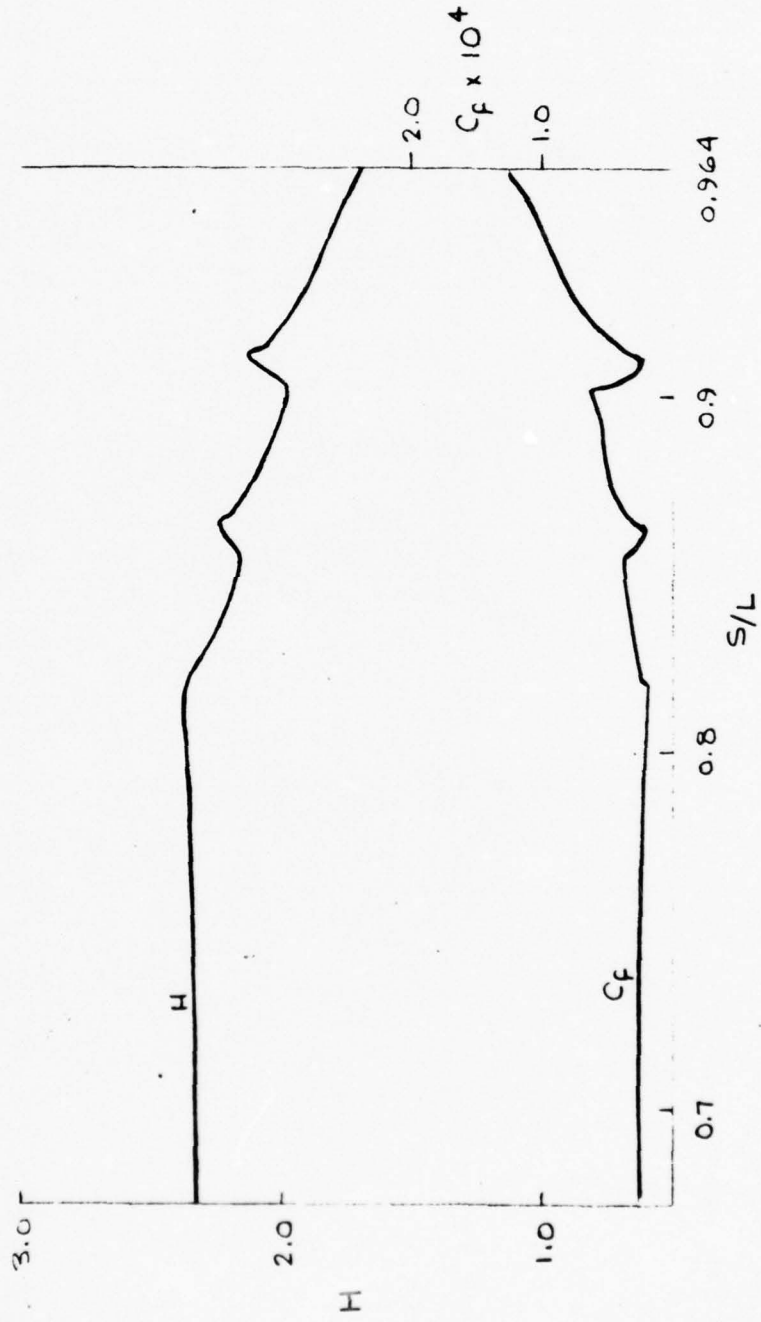


Figure 23. Shape Factor and Friction Coefficient vs. S/L Reichardt Body, Case 2-W

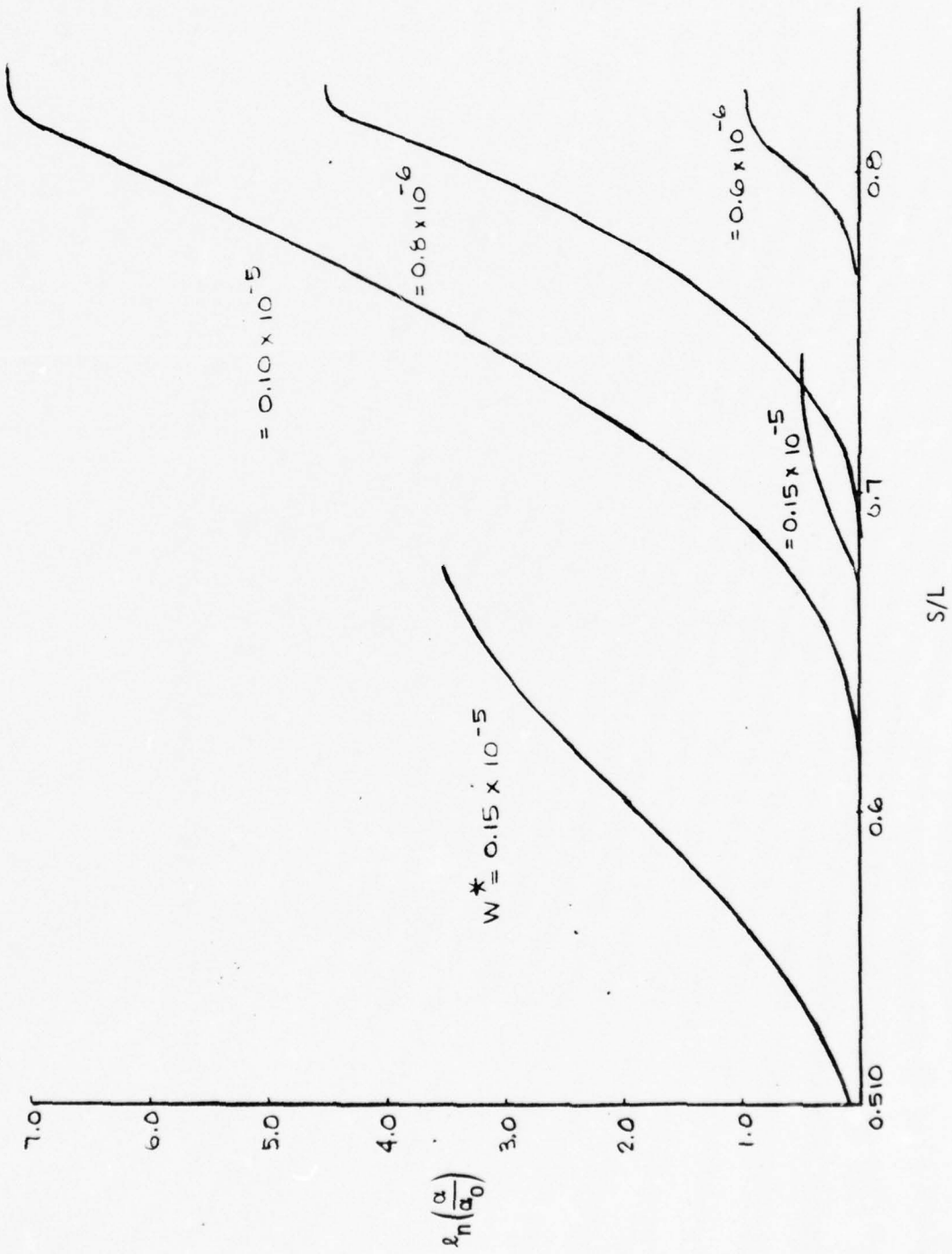


Figure 24. Stability Growth Factors for Reichardt, Case 2-W

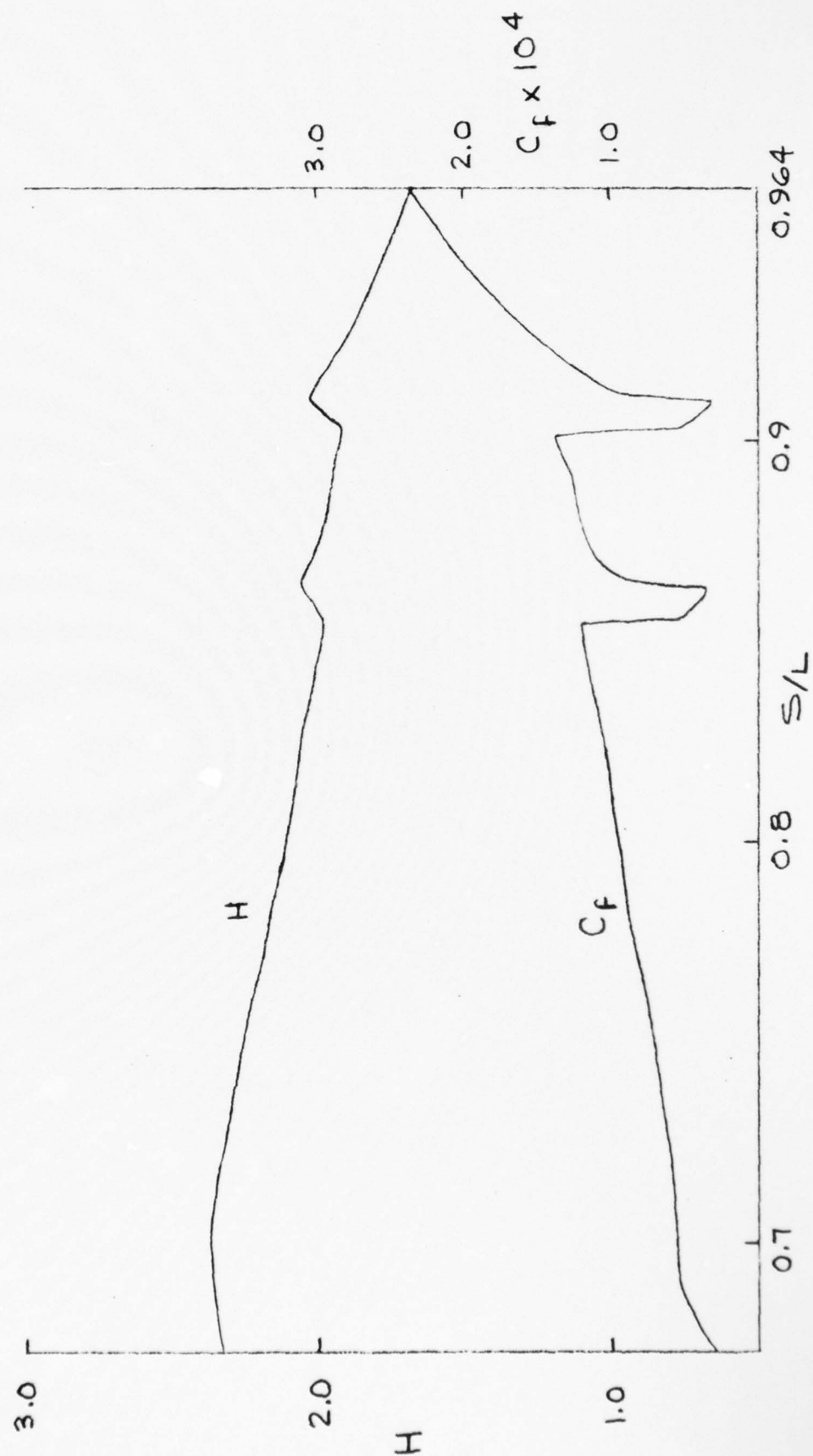


Figure 25. Shape Factor and Friction Coefficient vs.  $S/L$  (Reichardt Body, Case 3-W)

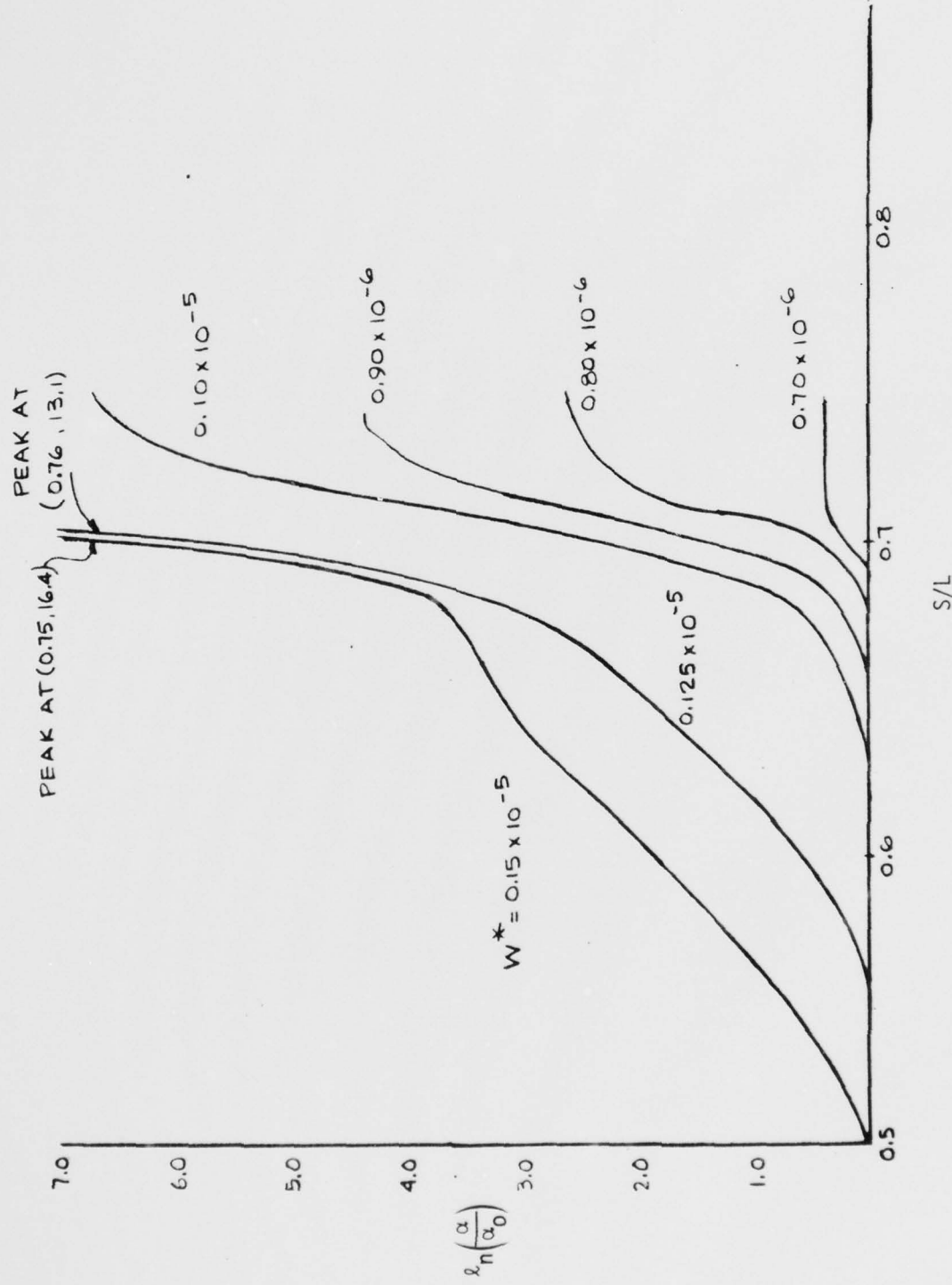


Figure 26. Stability Growth Factors for Richardt, Case 3-W

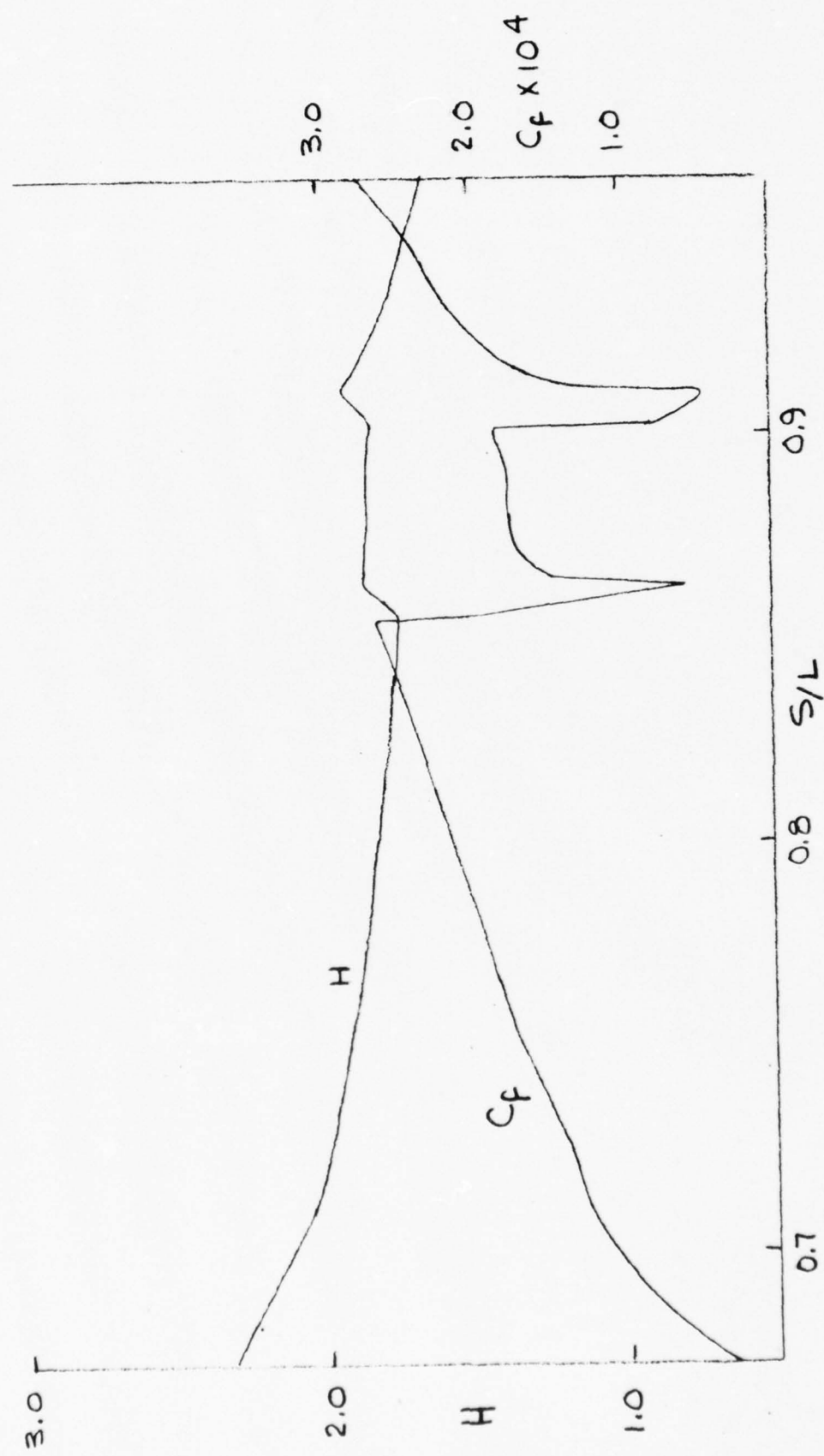


Figure 27. Shape Factor and Friction Coefficient vs.  $S/L$  Reichardt Body, Case 4-W

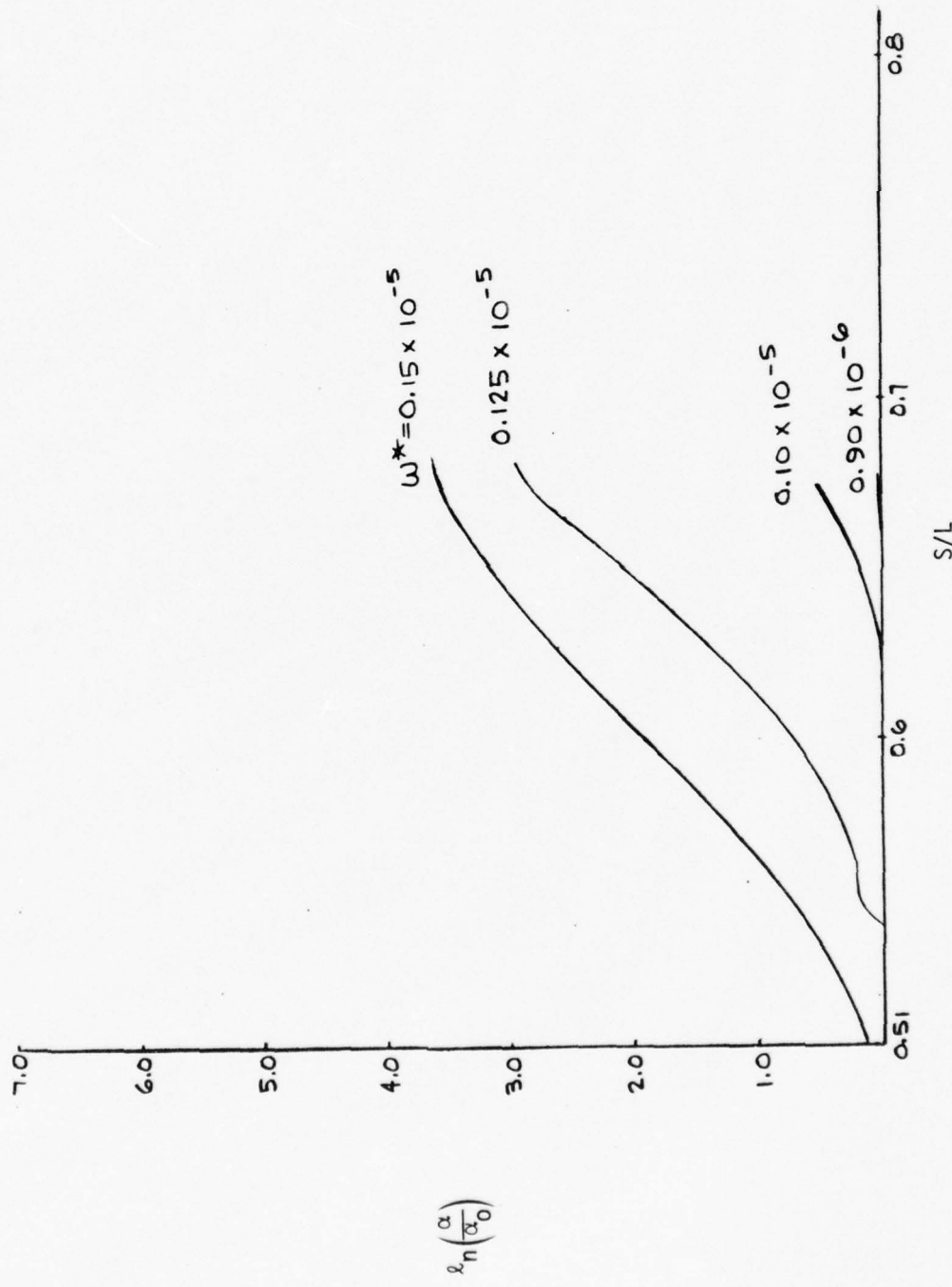


Figure 28. Stability Growth Factors for Reichardt Body, Case 4-W

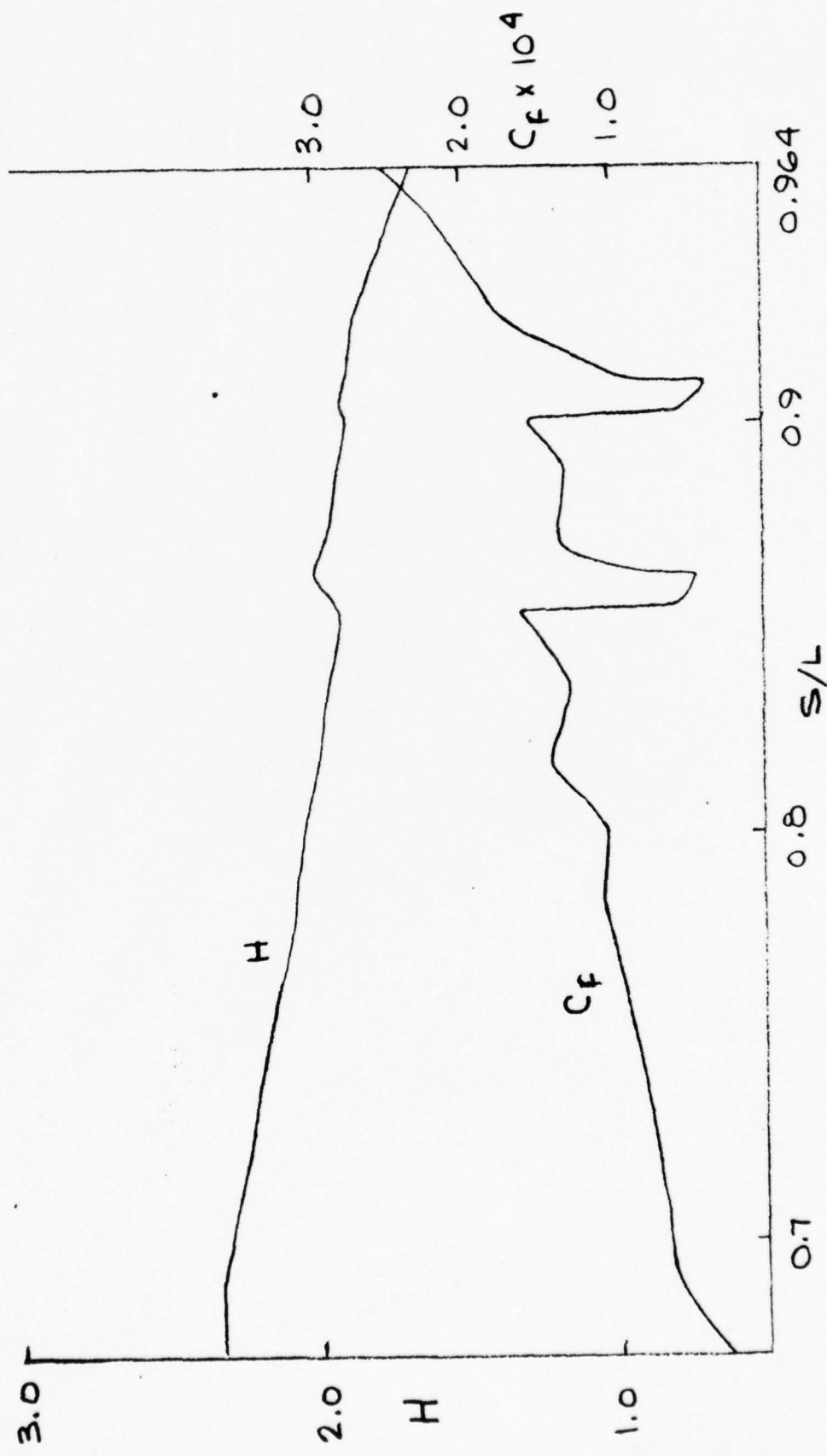


Figure 29. Shape Factor and Friction Coefficient vs.  $S/L$   
Reichardt Body, Case 5-W

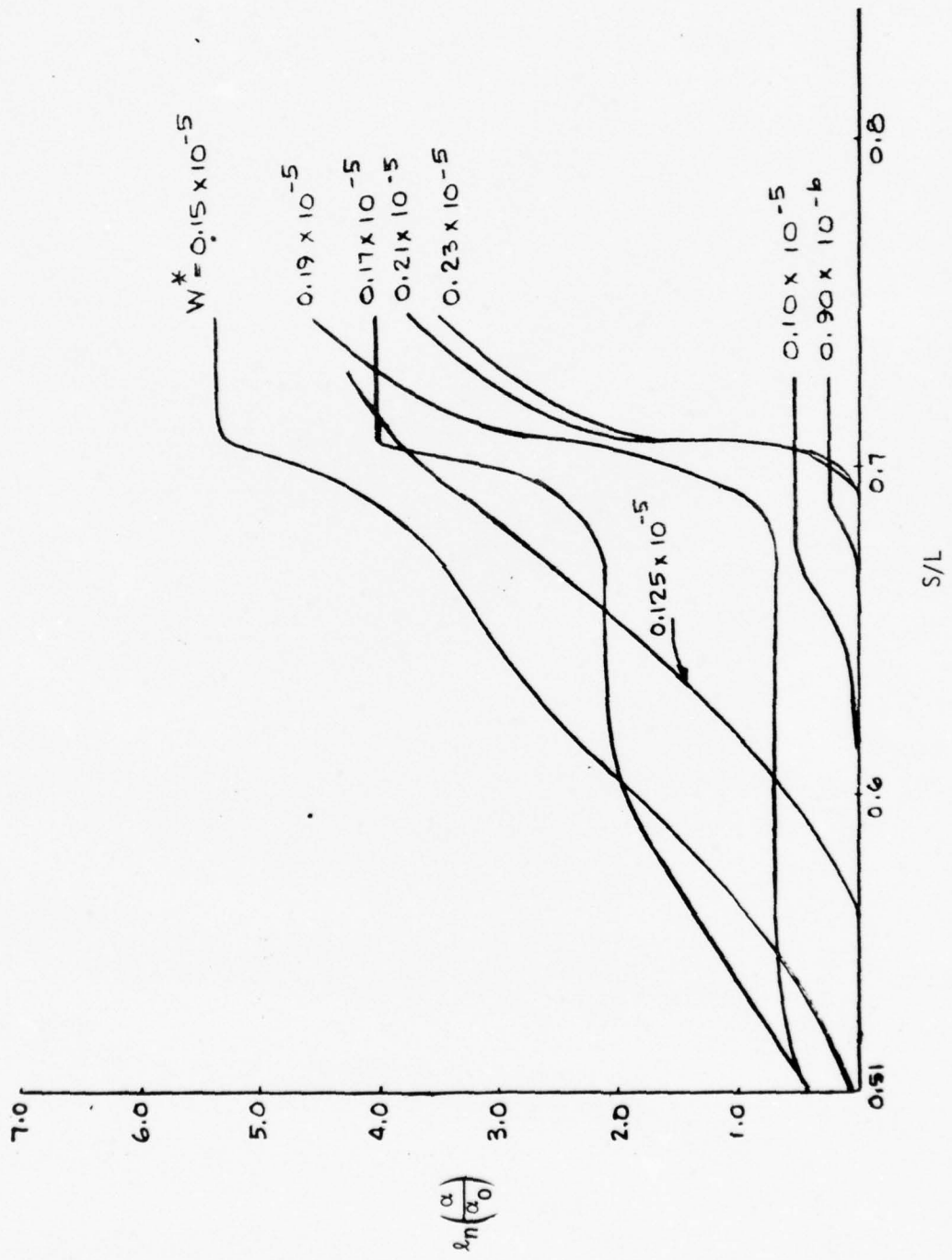


Figure 30. Stability Growth Factors for Reichardt Body, Case 5-W

SHAPE FACTOR -  $Re_{\delta^*}$  HISTORY  
 DISCONTINUOUS SUCTION PLUS HEATING

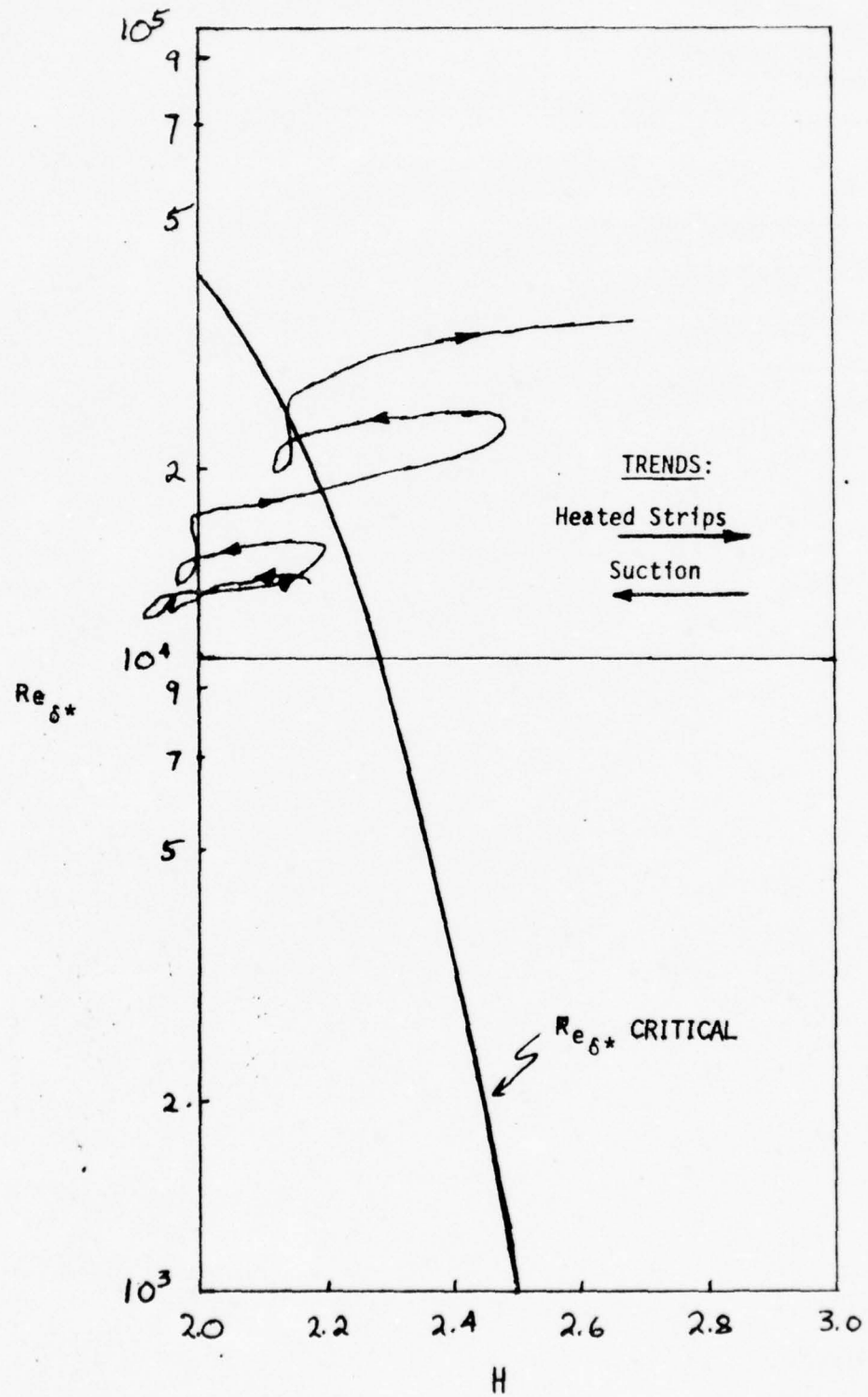


Figure 31. Shape Factor -  $Re_{\delta^*}$  History Discontinuous Suction Plus Heating  
 (AR-3 Body)

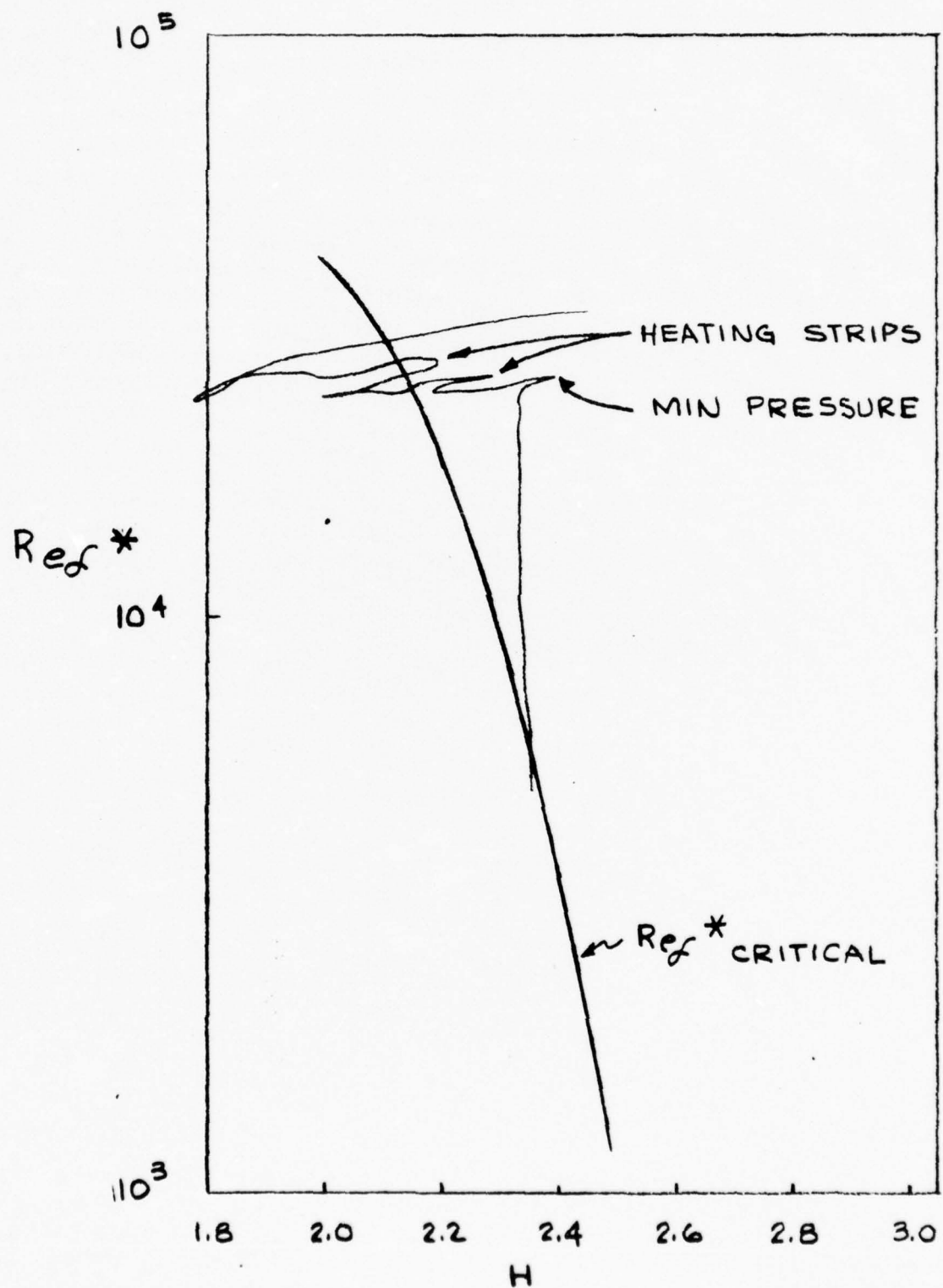


Figure 32. Shape Factor -  $Re_d^*$  History Discontinuous Suction Plus Heating (Reichardt Body, Case 1-W)

BEST AVAILABLE COPY

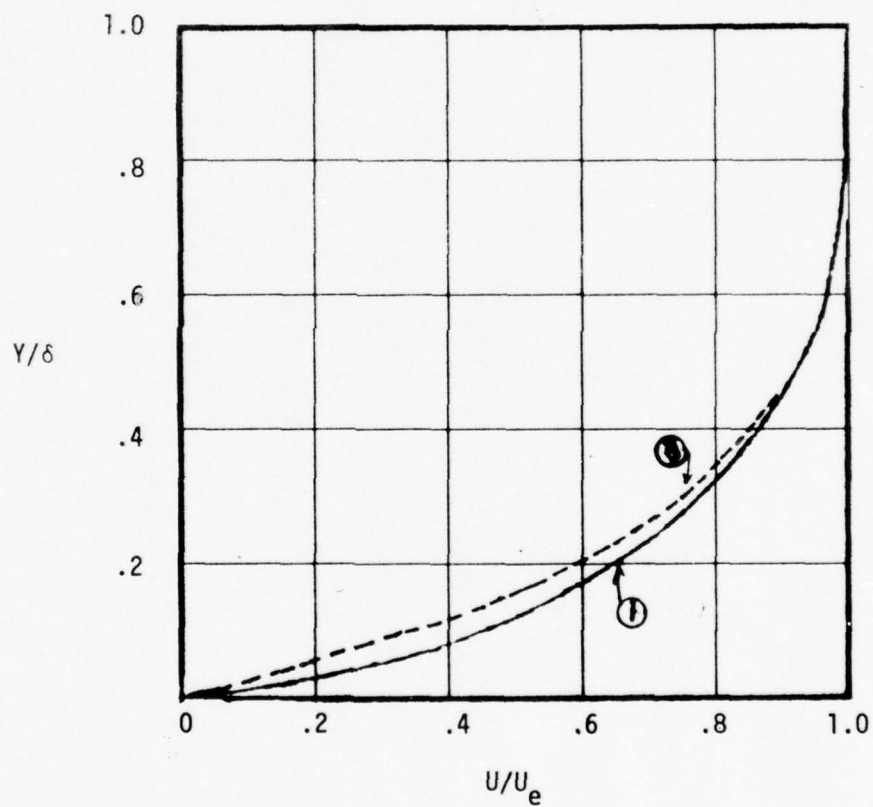


Figure 33. Velocity Profiles in an Adverse Pressure Gradient with Suction and Heating (reference Figure 12, AR-3 Body)

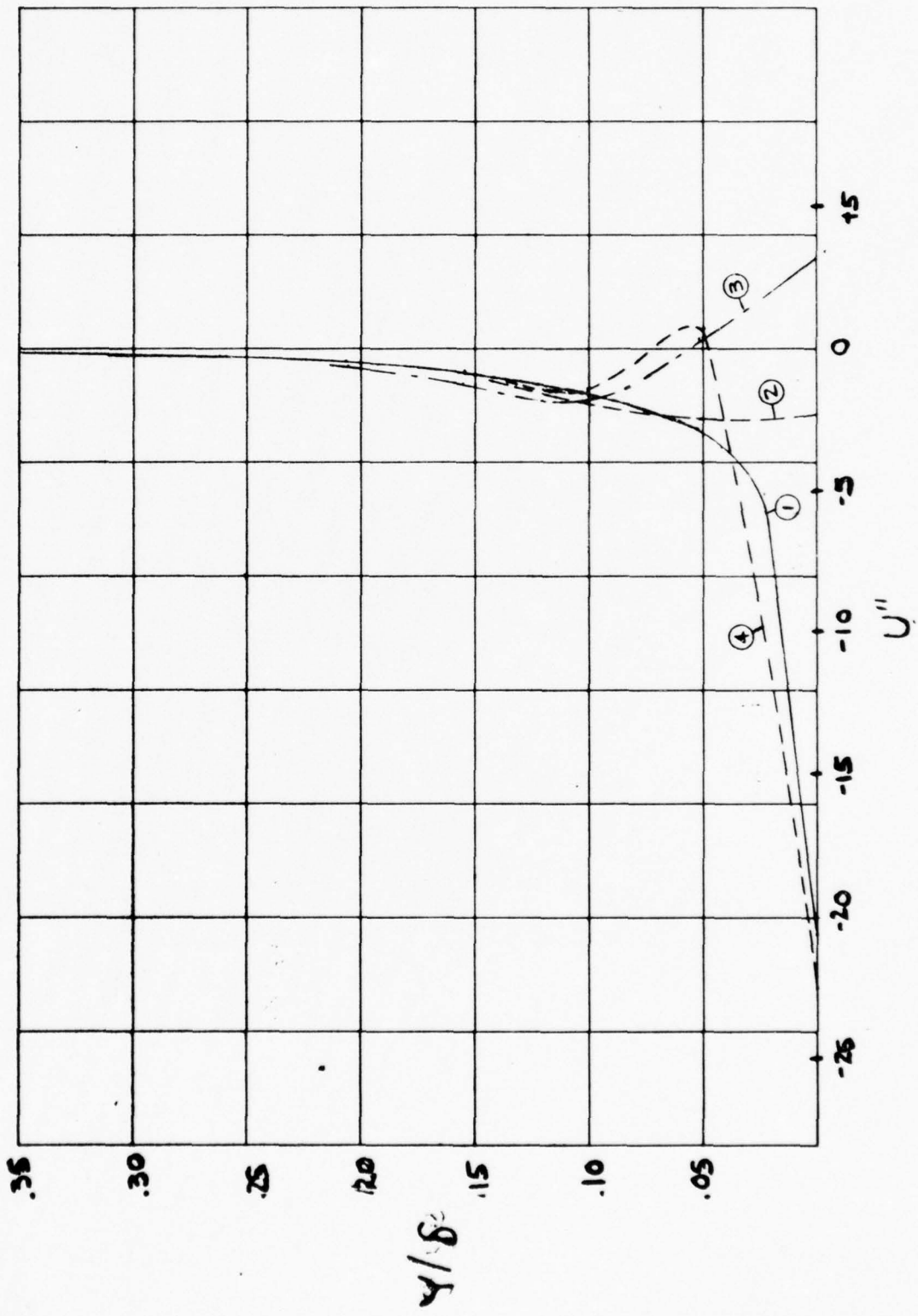


Figure 34. Second Derivative Profiles in an Adverse Pressure Gradient with Suction and Heating (reference Figure 12, AR-3 Body)

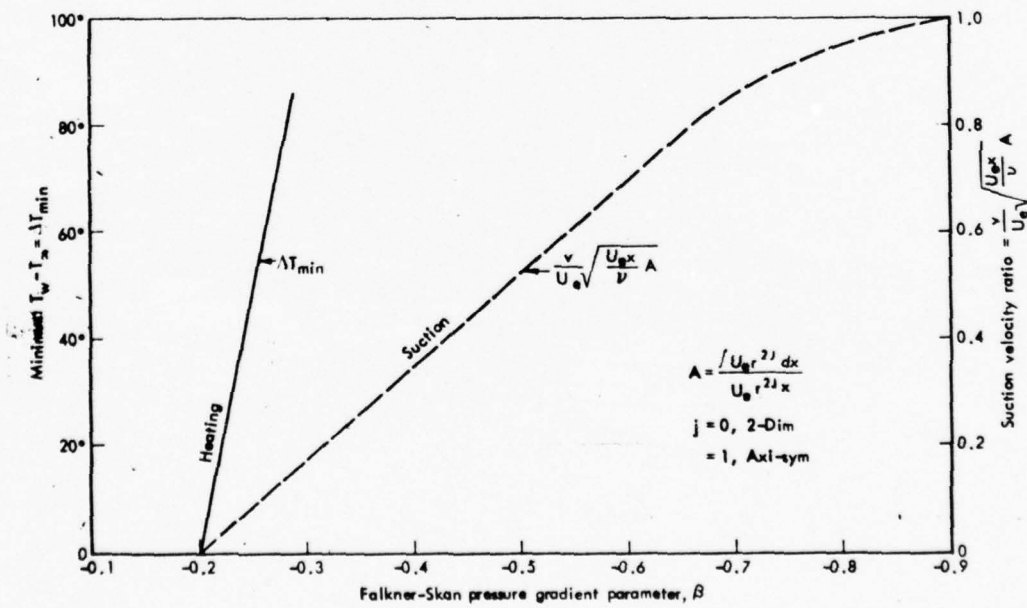
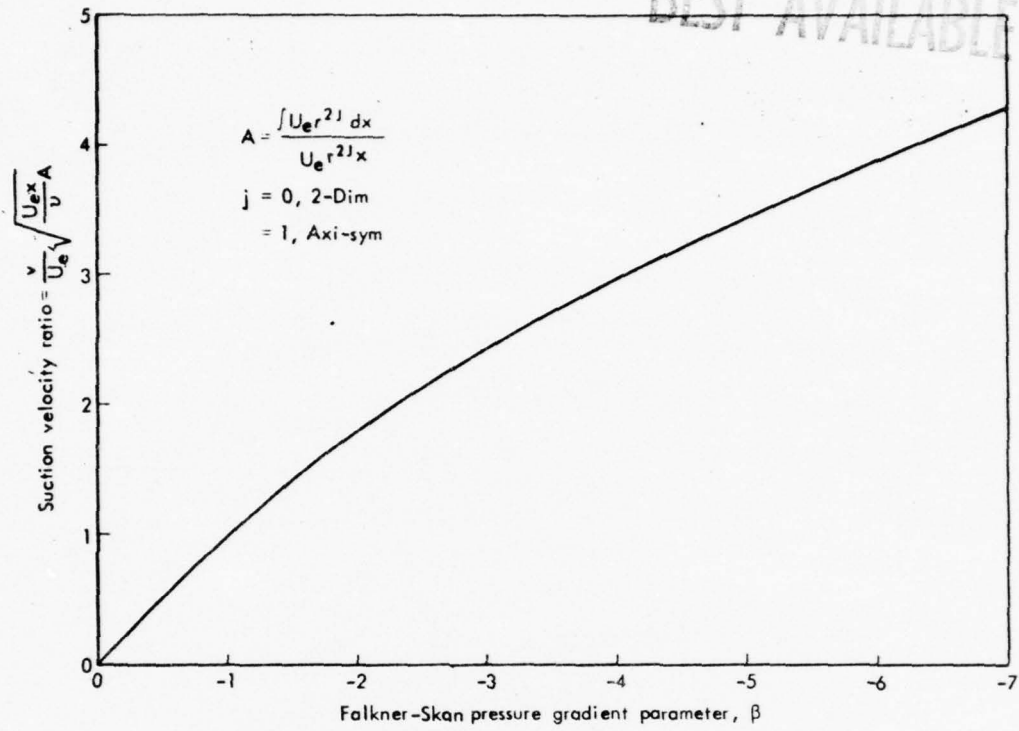


Figure 35. Required Surfacing Heating and Suction to Delay Laminar Separation (from Reference 11)

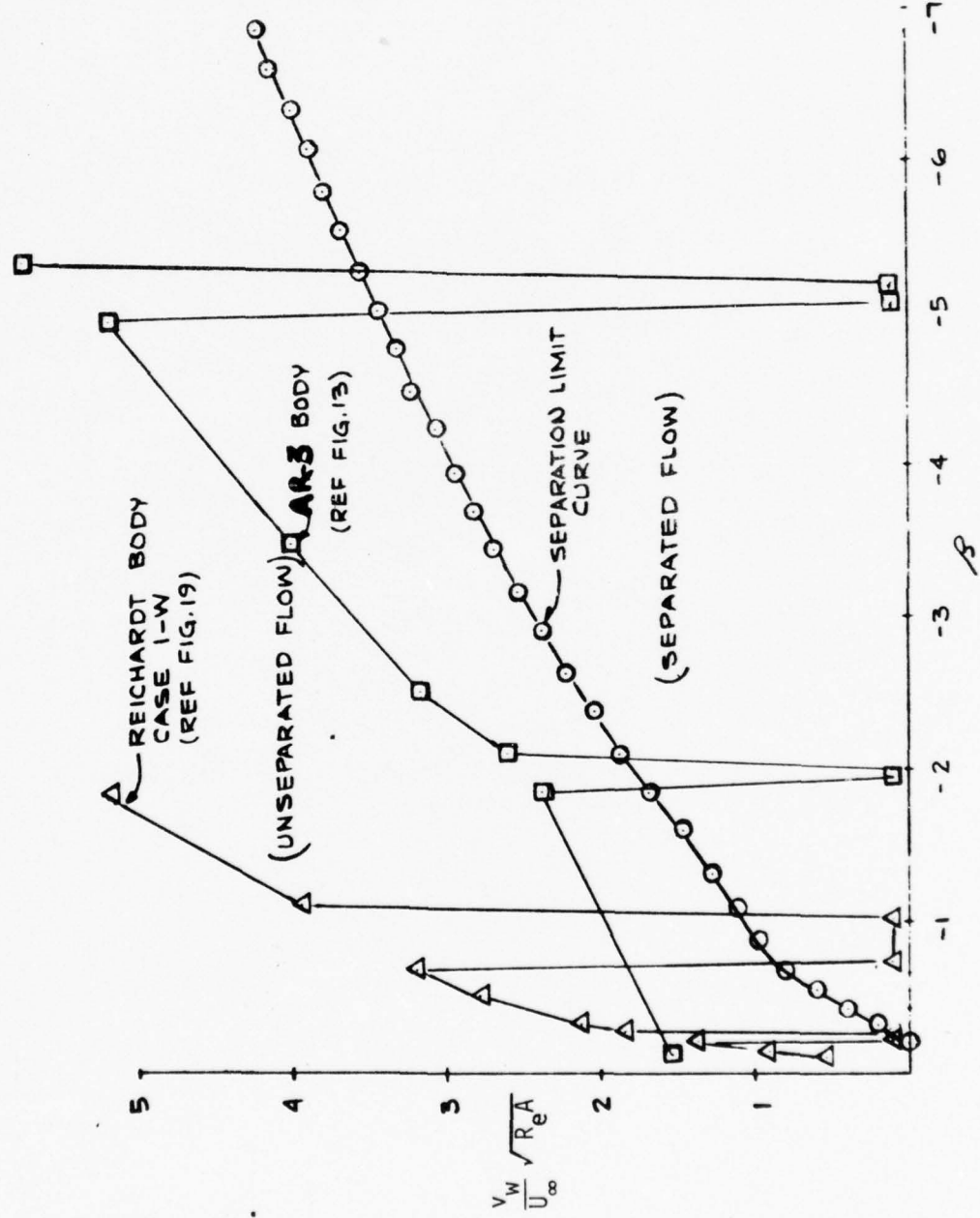


Figure 36. Suction Parameter vs.  $\beta$  History for Reichardt and AR-3 Bodies

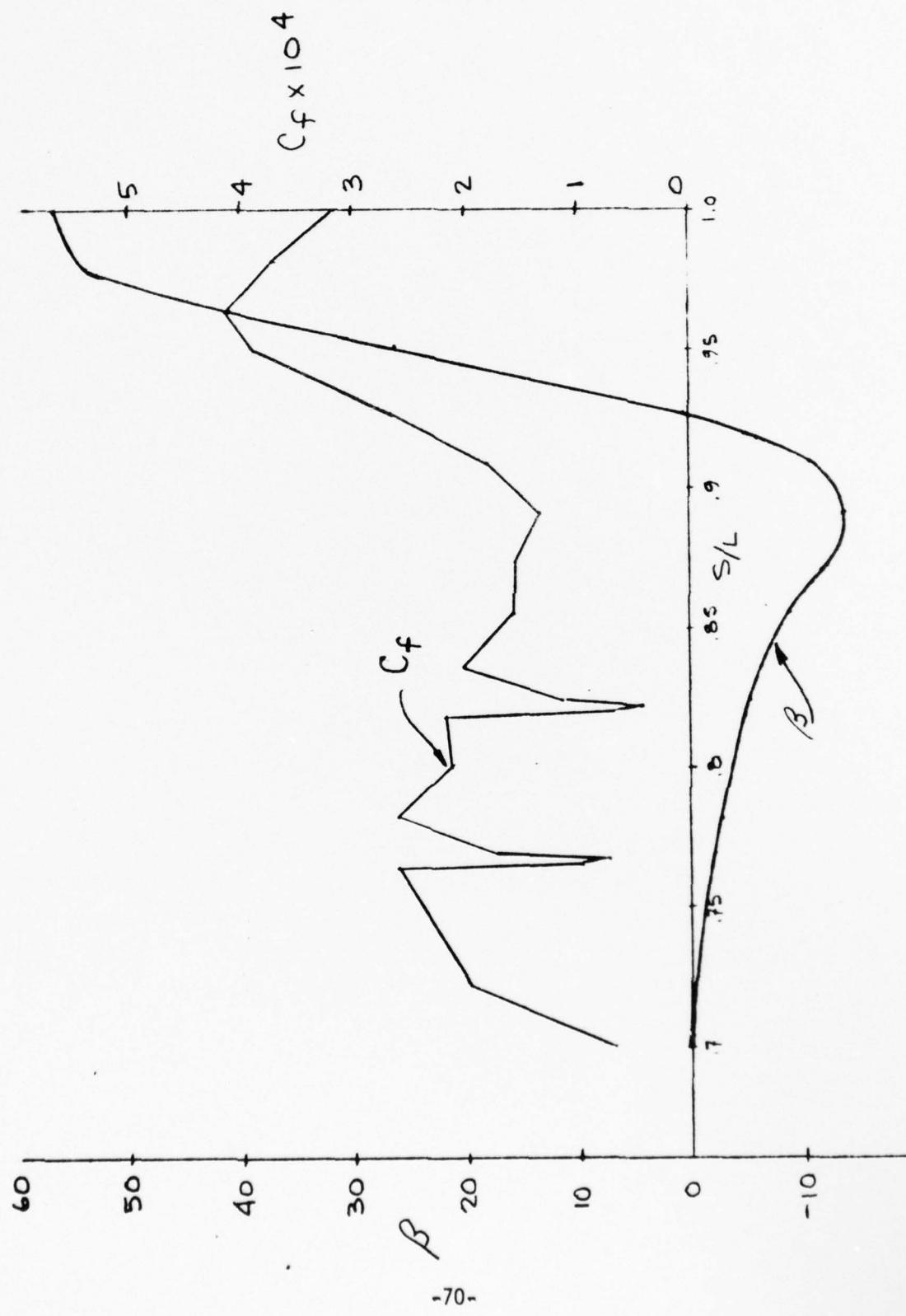


Figure 37.  $\beta$  and  $C_f$  vs.  $S/L$  (AR-3 Body)

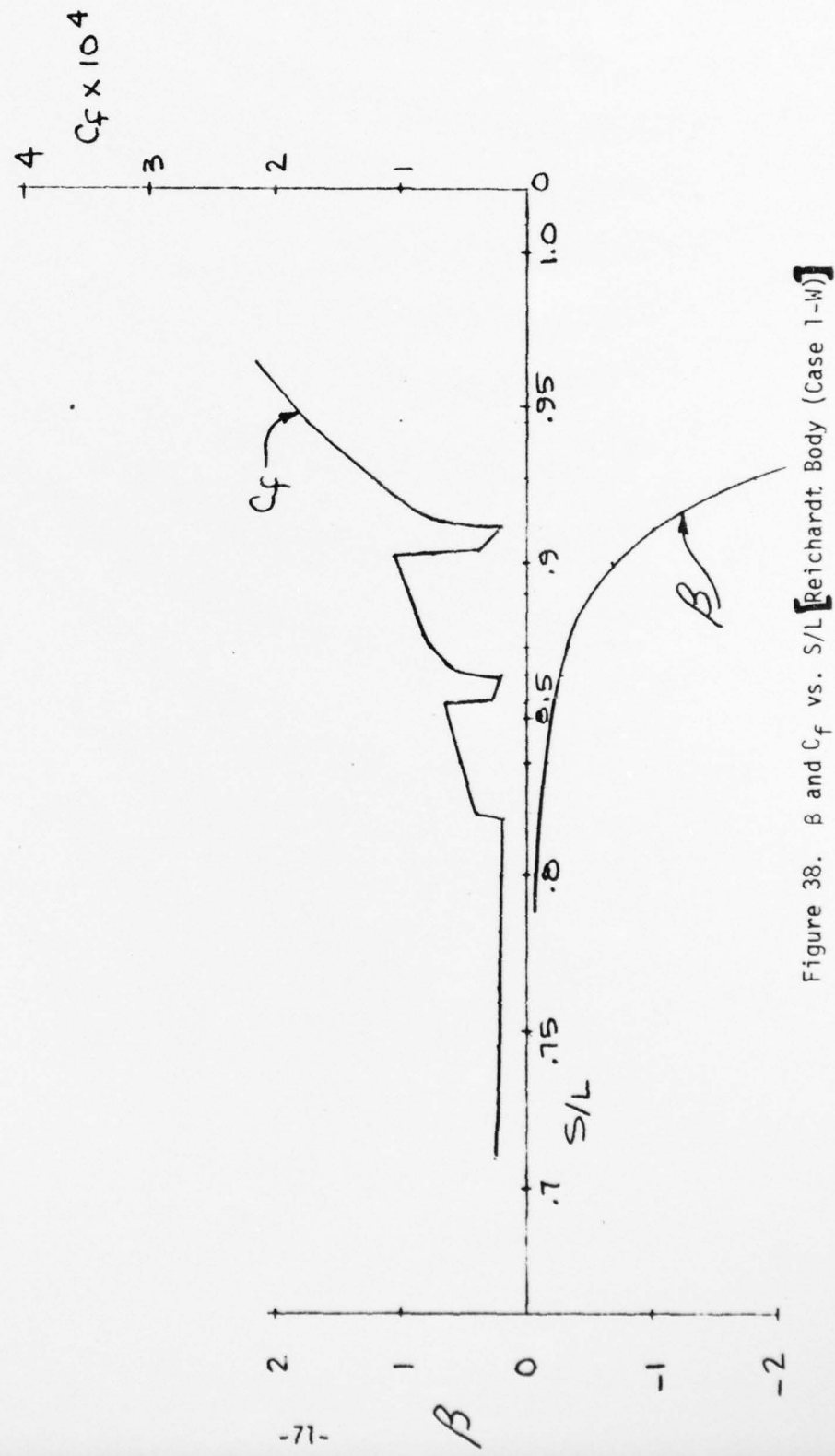
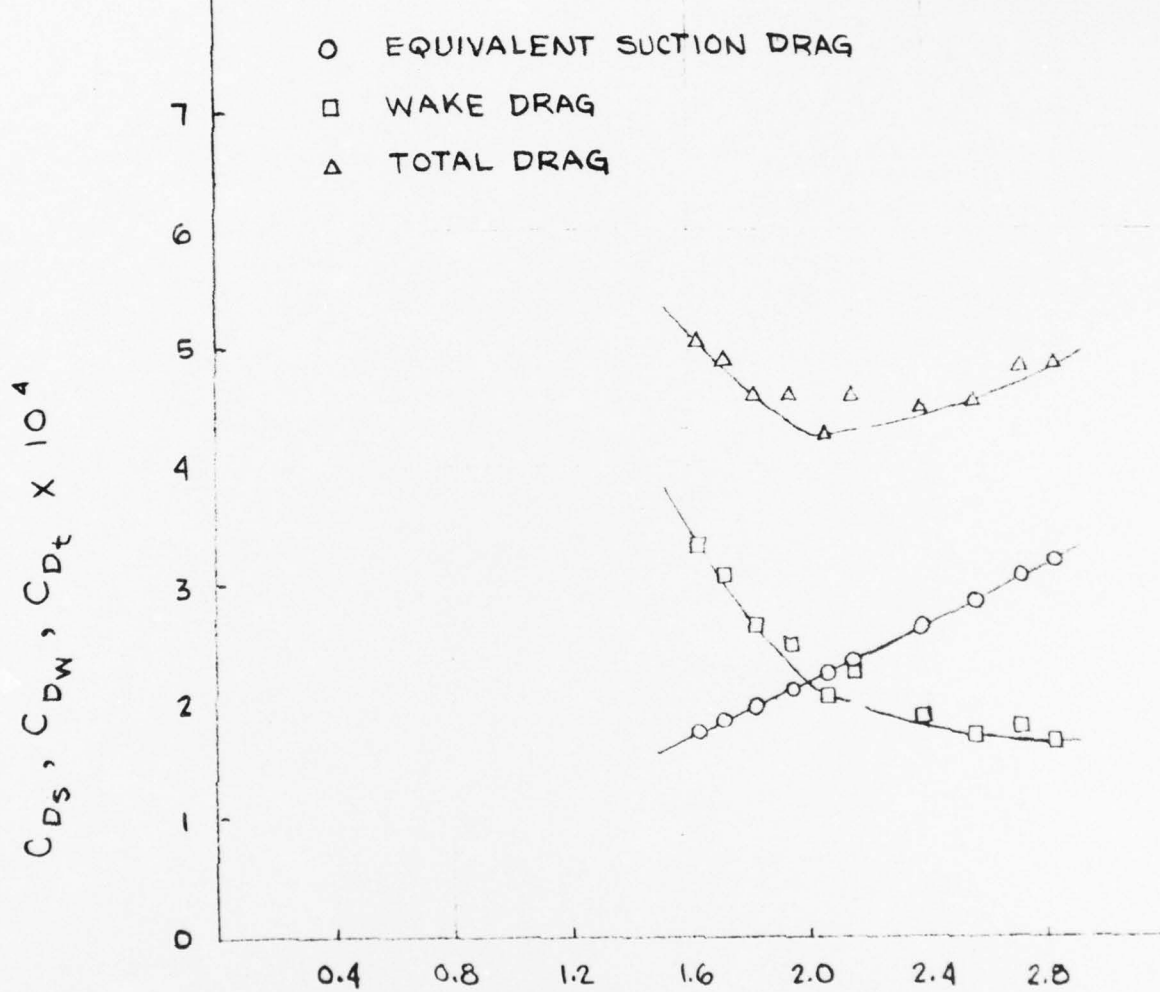


Figure 38.  $\beta$  and  $C_f$  vs.  $S/L$  [Reichardt Body (Case 1-W)]



$$C_{Q_t} \left( \frac{F_t^3 / SEC}{U_\infty - \text{WETTED AREA}} \right) \times 10^4$$

Figure 39. Drag Coefficients vs. Suction Quantity  
 (8:1) Reichardt Body in Air  
 $Re_L = 18.2 \times 10^6$

Table 1. AR-3 Contour (5:1)

Station	$S/L$	$R/L$	$C_p$	$T_w$	$\delta^*$	$H$	
						$T_\infty = 507.7^0$	$U = 84.45 \text{ ft/sec}$
1	0.004	0.002	0.2561	512.90	2.084 $\times 10^{-4}$	2.534	-0.282
2	0.005	0.003	0.2402	513.80	2.378 $\times 10^{-4}$	2.517	-0.371
3	0.007	0.003	0.2218	514.90	2.807 $\times 10^{-4}$	2.508	-0.391
4	0.010	0.004	0.2060	517.70	3.295 $\times 10^{-4}$	2.508	-0.428
5	0.012	0.005	0.1973	519.80	3.698 $\times 10^{-4}$	2.499	-0.421
6	0.015	0.005	0.1910	522.10	4.040 $\times 10^{-4}$	2.485	-0.393
7	0.018	0.006	0.1854	524.80	4.336 $\times 10^{-4}$	2.469	-0.380
8	0.020	0.007	0.1811	524.80	4.624 $\times 10^{-4}$	2.465	-0.309
9	0.024	0.007	0.1760	524.80	5.018 $\times 10^{-4}$	2.463	-0.274
10	0.029	0.008	0.1698	524.80	5.486 $\times 10^{-4}$	2.462	-0.247
11	0.034	0.010	0.1648	524.80	5.908 $\times 10^{-4}$	2.463	-0.228
12	0.039	0.011	0.1604	524.80	6.289 $\times 10^{-4}$	2.462	-0.214
13	0.045	0.012	0.1563	524.80	6.641 $\times 10^{-4}$	2.461	-0.203
14	0.050	0.013	0.1524	524.80	6.971 $\times 10^{-4}$	2.460	-0.193
15	0.059	0.015	0.1465	525.00	7.499 $\times 10^{-4}$	2.459	-0.182
16	0.071	0.017	0.1384	525.00	8.171 $\times 10^{-4}$	2.458	-0.165
17	0.084	0.020	0.1309	525.20	8.770 $\times 10^{-4}$	2.455	-0.155
18	0.097	0.022	0.1237	525.30	9.315 $\times 10^{-4}$	2.452	-0.146

Table 1 - Continued

Station	S/L	R/L	C <sub>P</sub>	T <sub>w</sub>	$\delta^*$	H	$h = (q/T_w - T_a)$
23	0.218	0.046	0.0592	527.00	$13.04 \times 10^{-4}$	2.421	-0.106
24	0.243	0.051	0.0452	527.30	$13.62 \times 10^{-4}$	2.413	-0.101
25	0.269	0.056	0.0308	527.70	$14.16 \times 10^{-4}$	2.405	-0.098
26	0.294	0.060	0.0161	527.90	$14.67 \times 10^{-4}$	2.398	-0.094
27	0.320	0.064	0.0011	528.00	$15.15 \times 10^{-4}$	2.391	-0.090
28	0.345	0.069	-0.0144	528.60	$15.60 \times 10^{-4}$	2.385	-0.090
29	0.370	0.073	-0.0303	529.10	$16.01 \times 10^{-4}$	2.375	-0.088
30	0.396	0.077	-0.0466	529.70	$16.41 \times 10^{-4}$	2.367	-0.086
31	0.421	0.080	-0.0634	530.20	$16.79 \times 10^{-4}$	2.358	-0.084
32	0.446	0.084	-0.0806	530.70	$17.16 \times 10^{-4}$	2.349	-0.082
33	0.471	0.087	-0.0983	531.30	$17.52 \times 10^{-4}$	2.341	-0.081
34	0.497	0.090	-0.1165	531.80	$17.87 \times 10^{-4}$	2.331	-0.079
35	0.522	0.093	-0.1352	532.40	$18.22 \times 10^{-4}$	2.322	-0.078
36	0.547	0.095	-0.1545	532.90	$18.56 \times 10^{-4}$	2.312	-0.076
37	0.572	0.097	-0.1746	533.40	$18.90 \times 10^{-4}$	2.302	-0.074
38	0.597	0.098	-0.1958	533.80	$19.22 \times 10^{-4}$	2.289	-0.072
39	0.622	0.099	-0.2189	533.80	$19.53 \times 10^{-4}$	2.275	-0.068
40	0.647	0.100	-0.2442	533.80	$19.43 \times 10^{-4}$	2.237	-0.067
41	0.672	0.100	-0.2964	533.80	$18.79 \times 10^{-4}$	2.175	-0.068
42	0.697	0.099	-0.3707	533.80	$18.81 \times 10^{-4}$	2.158	-0.066
43	0.722	0.097	-0.3988	533.80	$19.56 \times 10^{-4}$	2.145	-0.136
44	0.748	0.092	-0.3440	533.80	$23.04 \times 10^{-4}$	2.218	-0.248
45	0.773	0.085	-0.2247	533.80			
46	0.800	0.076	-0.0801	533.80			
47	0.827	0.066	0.0563	533.80			

Table 1 - Continued

<u>Station</u>	<u>S/L</u>	<u>R/L</u>	<u>C<sub>p</sub></u>	<u>T<sub>w</sub></u>	<u>δ*</u>	<u>H</u>	<u>h = (q/T<sub>w</sub> - T<sub>a</sub>)</u>
48	0.854	0.055	0.1728	533.80			
49	0.881	0.045	0.2773	533.80			
50	0.908	0.035	0.3449	533.80			
51	0.934	0.027	0.3564	533.80			
52	0.960	0.023	0.3197	533.80			
53	0.977	0.021	0.2741	533.80			
54	0.987	0.020	0.2433	533.80			
55	0.997	0.020	0.2110	533.80			
56	1.007	0.020	0.1782	533.80			
57	1.017	0.020	0.1449	533.80			

Table 2. Tollmien-Schlichting Wave Growth Factors ( $\beta_n \alpha/\alpha_0$ ) AR-3 Body

<u>S/L</u>	<u><math>1.0 \times 10^{-6}</math></u>	<u><math>1.5 \times 10^{-6}</math></u>	<u><math>2.5 \times 10^{-6}</math></u>	<u><math>4.5 \times 10^{-6}</math></u>	<u><math>6.5 \times 10^{-6}</math></u>	<u><math>8.5 \times 10^{-6}</math></u>	<u><math>10.0 \times 10^{-6}</math></u>
0.700	0.0	0.0	0.0	0.0	0.0	①*	0.0
0.722	0.0	0.0	0.0	0.0	0.0	②	0.0
0.764	0.0	0.0	0.0	0.0	0.0	③	0.0
0.765	0.0	0.0	0.0	0.0	0.0	④	0.0
0.767						⑤	0.0
0.769						⑥	0.0
0.800						⑦	0.0
0.818						⑧	0.0
0.820						⑨	0.0
0.822						⑩	0.0
0.824						⑪	0.0
0.836						⑫	0.0
0.854						⑬	0.0
0.873						⑭	0.0
0.891						⑮	0.0
0.909						⑯	0.0
0.927						⑰	0.0

\*DENOTES START OF STABILITY CALCULATION RUN. REFER TO FIGURES 13 AND 14.

Table 3. Reichardt Contour (5:1)

Station	<u>S/L</u>	<u>R/L</u>	<u>C<sub>p</sub></u>	<u>T<sub>w</sub></u>	<u>δ*</u>	<u>H</u>	<u>h = (q/T<sub>w</sub> - T<sub>a</sub>)</u>
1	0.027	0.025	0.4054	516.62	4.913 × 10 <sup>-4</sup>	2.324	-0.1497
2	0.030	0.027	0.3230	518.01	4.651 × 10 <sup>-4</sup>	2.290	-0.2072
3	0.034	0.030	0.2572	520.21	4.622 × 10 <sup>-4</sup>	2.295	-0.2640
4	0.037	0.032	0.2063	522.00	4.718 × 10 <sup>-4</sup>	2.306	-0.2688
5	0.040	0.034	0.1639	523.53	4.873 × 10 <sup>-4</sup>	2.314	-0.2666
6	0.045	0.036	0.1158	525.43	5.157 × 10 <sup>-4</sup>	2.324	-0.2574
7	0.051	0.039	0.0695	527.50	5.566 × 10 <sup>-4</sup>	2.333	-0.2435
8	0.056	0.042	0.0352	529.20	5.972 × 10 <sup>-4</sup>	2.337	-0.2302
9	0.062	0.045	0.0089	530.62	6.384 × 10 <sup>-4</sup>	2.344	-0.2172
10	0.068	0.047	-0.0082	531.85	6.783 × 10 <sup>-4</sup>	2.349	-0.2059
11	0.073	0.049	-0.0242	532.92	7.145 × 10 <sup>-4</sup>	2.350	-0.1963
12	0.082	0.052	-0.0451	534.51	7.750 × 10 <sup>-4</sup>	2.353	-0.1816
13	0.096	0.057	-0.0638	536.35	8.565 × 10 <sup>-4</sup>	2.357	-0.1646
14	0.109	0.060	-0.0762	537.82	9.330 × 10 <sup>-4</sup>	2.359	-0.1510
15	0.122	0.064	-0.0834	539.05	10.05 × 10 <sup>-4</sup>	2.361	-0.1458
16	0.141	0.068	-0.0919	540.54	11.02 × 10 <sup>-4</sup>	2.360	-0.1273
17	0.166	0.073	-0.0990	542.10	12.22 × 10 <sup>-4</sup>	2.359	-0.1142
18	0.192	0.078	-0.1026	543.34	13.34 × 10 <sup>-4</sup>	2.358	-0.1042
19	0.217	0.081	-0.1044	544.35	14.39 × 10 <sup>-4</sup>	2.356	-0.0962
20	0.242	0.084	-0.1058	545.19	15.38 × 10 <sup>-4</sup>	2.352	-0.0896
21	0.267	0.087	-0.1065	545.91	16.34 × 10 <sup>-4</sup>	2.350	-0.0840
22	0.292	0.090	-0.1069	546.53	17.26 × 10 <sup>-4</sup>	2.347	-0.0792
23	0.318	0.092	-0.1072	547.08	18.16 × 10 <sup>-4</sup>	2.344	-0.0750

Table 3 - Continued

Station	S/L	R/L	C <sub>p</sub>	T <sub>w</sub>	$\delta^*$	H	$h = (q/\tau_w - \tau_a)$
24	0.343	0.094	-0.1072	547.57	19.04 x 10 <sup>-4</sup>	2.343	-0.0712
25	0.368	0.095	-0.1075	547.70	19.90 x 10 <sup>-4</sup>	2.341	-0.0667
26	0.393	0.097	-0.1078	547.70	20.78 x 10 <sup>-4</sup>	2.341	-0.0628
27	0.418	0.098	-0.1071	547.70	21.67 x 10 <sup>-4</sup>	2.342	-0.0597
28	0.443	0.099	-0.1071	547.70	22.53 x 10 <sup>-4</sup>	2.341	-0.0569
29	0.468	0.099	-0.1071	547.70	23.41 x 10 <sup>-4</sup>	2.342	-0.0544
30	0.493	0.100	-0.1069	547.70	24.29 x 10 <sup>-4</sup>	2.342	-0.0521
31	0.518	0.100	-0.1068	547.70	25.18 x 10 <sup>-4</sup>	2.340	-0.0499
32	0.543	0.100	-0.1066	547.70	26.11 x 10 <sup>-4</sup>	2.342	-0.0477
33	0.568	0.100	-0.1063	547.70	27.07 x 10 <sup>-4</sup>	2.342	-0.0457
34	0.593	0.099	-0.1061	547.70	28.05 x 10 <sup>-4</sup>	2.343	-0.0438
35	0.618	0.099	-0.1057	547.70	29.09 x 10 <sup>-4</sup>	2.344	-0.0419
36	0.643	0.098	-0.1051	547.70	30.14 x 10 <sup>-4</sup>	2.344	-0.0401
37	0.668	0.097	-0.1052	547.70	31.27 x 10 <sup>-4</sup>	2.344	-0.0383
38	0.693	0.095	-0.1044	547.70	32.54 x 10 <sup>-4</sup>	2.349	-0.0364
39	0.718	0.094	-0.1033	547.70	33.89 x 10 <sup>-4</sup>	2.352	-0.0346
40	0.743	0.092	-0.1023	547.70	35.39 x 10 <sup>-4</sup>	2.356	-0.0327
41	0.768	0.090	-0.1008	547.70	37.10 x 10 <sup>-4</sup>	2.362	-0.0307
42	0.793	0.087	-0.0989	547.70	39.09 x 10 <sup>-4</sup>	2.372	-0.0286
43	0.818	0.084	-0.0962	547.70	41.53 x 10 <sup>-4</sup>	2.388	-0.0263
44	0.844	0.081	-0.0929	547.70	44.67 x 10 <sup>-4</sup>	2.416	-0.0237
45	0.869	0.078	-0.0862	547.70	49.22 x 10 <sup>-4</sup>	2.471	-0.0204
46	0.894	0.073	-0.0763	547.70	59.43 x 10 <sup>-4</sup>	2.670	-0.0139
47	0.920	0.068	-0.0590	547.70			
48	0.945	0.062	-0.0253	547.70			

Table 3 - Continued

<u>Station</u>	<u>S/L</u>	<u>R/L</u>	<u>C<sub>p</sub></u>	<u>T<sub>w</sub></u>	<u>δ*</u>	<u>H</u>	<u>h = (q/T<sub>w</sub> - T<sub>a</sub>)</u>
49	0.972	0.055	0.0064	547.70			
50	0.990	0.048	0.3663	547.70			
51	1.001	0.044	0.3803	547.70			
52	1.011	0.041	0.3643	547.70			
53	1.022	0.039	0.3617	547.70			
54	1.032	0.038	0.2927	547.70			
55	1.042	0.037	0.2640	547.70			
56	1.052	0.037	0.2380	547.70			
57	1.062	0.036	0.1976	547.70			

Table 4. Suction Plus Heat Cases Investigated for the Reichardt Body

STN	S/L	CASE 1-W		CASE 2-W		CASE 3-W		CASE 4-W		CASE 5-W	
		T( <sup>°</sup> R)	SUCTION*	T( <sup>°</sup> R)	SUCTION	T( <sup>°</sup> R)	SUCTION	T( <sup>°</sup> R)	SUCTION	T( <sup>°</sup> R)	SUCTION
67	0.636	547.7		547.7		547.7		547.7		547.7	
68	0.654					547.7		547.7		547.7	
69	0.673					547.7		547.7		547.7	
70	0.691					508.0	-0.00001	508.0	-0.00010	508.0	-0.00003
71	0.709						-0.00002		-0.00011		-0.00004
72	0.727						-0.00003		-0.00012		-0.00005
73	0.745						-0.00004		-0.00013		-0.00006
74	0.764						-0.00005		-0.00014		-0.00007
75	0.782						-0.00006		-0.00015		-0.00008
76	0.800						-0.00007		-0.00016		-0.00009
77	0.818	547.7					-0.00008		-0.00017		-0.00010
78	0.820	508.0	-0.00003								
79	0.836	508.0	-0.00005								
80	0.845	508.0	-0.00007								
81	0.856	548.0									
82	0.864	548.0									
83	0.865	508.0	-0.00009								
84	0.873	508.0	-0.00010								
85	0.891	508.0	-0.00012								
86	0.902	508.0	-0.00013								
87	0.904	548.0									
88	0.911	548.0									
89	0.913	508.0	-0.00015								
90	0.927	508.0	-0.00018								
91	0.945	508.0	-0.00021								
92	0.964	508.0	-0.00017	547.7							

\*  $\frac{\rho v_w}{\rho_\infty U_\infty}$ , where  $\rho$  is density,  $v_w$  is suction velocity and  $U_\infty$  is freestream velocity.

DISTRIBUTION LIST

Chief of Naval Research Department of the Navy Arlington, VA 22217 ATTN: Vehicles and Propulsion Program Code 211	3	U.S. Army Material Command 5001 Eisenhower Avenue Alexandria, VA 22333 ATTN: AMCRD-F	1
Chief of Naval Development Department of the Navy Washington, DC 20360 ATTN: NAVMAT 0331 NAVMAT 0334	1	Air Force Office of Scientific Research Bolling Air Force Base Bldg. 410 Washington, DC 20332 ATTN: Mr. M. Rogers	1
David Taylor Naval Ship Research & Development Center Bethesda, MD 20084 ATTN: Code 522.1	1	National Aeronautics and Space Administration 600 Independence Avenue, SW Washington, DC 20546 ATTN: Code RAA Code RAV	1
Naval Research Laboratory Washington, DC 20375 ATTN: Technical Information Office, Code 2627	1	Office of Naval Research Department of the Navy Arlington, VA 22217 ATTN: Mr. M. Cooper, Code 430B	1
Superintendent U.S. Naval Academy Annapolis, MD 21402	1	ONR Branch Office 1030 East Green Street Pasadena, CA 91106 ATTN: Mr. B. F. Cagle	1
Superintendent U.S. Naval Postgraduate School Monterey, CA 93940	1	ONR Branch Office Chicago 536 South Clark St. Chicago, Ill 60605 ATTN: Mr. M. A. Chaszeyka	1
Commander Naval Under Sea Center San Diego, CA 92132 ATTN: Mr. T. Lang	1	Office of Naval Research Branch Office 495 Summer Street Boston, MA 02210 ATTN: Dr. A. D. Wood	1
Commandant of the Marine Corps Washington, DC 20380 ATTN: Dr. A. L. Slafkosky Scientific Advisor (Code RD-1)	1		
Defense Documentation Center Cameron Station, Bldg. 5 Alexandria, VA 22314	2		
Department of the Army DCS for Research and Development and Acquisition Washington, DC 20310 ATTN: DAMA-WSA (Mr. R. L. Ballard)	1		

ACOSTA, Professor Allan J.  
Department of Mechanical Engineering  
California Institute of Technology  
Pasadena, California 91125

AROESTY, Dr. Jerome  
Physical Sciences Department  
The Rand Corporation  
1700 Main Street  
Santa Monica, California 90406

BARKER, Professor Steven J.  
Mechanics and Structures Department  
School of Engineering  
5731 Boelter Hall  
University of California  
Los Angeles, California 90024

CHARWAT, Professor Andrew F.  
School of Engineering and Applied Science  
University of California  
Los Angeles, California 90024

CROW, Professor Steven  
School of Engineering and Applied Science  
University of California  
Los Angeles, California 90024

ELLISON, Dr. William  
Cambridge Acoustical Associates, Inc.  
1033 Massachusetts Avenue  
Cambridge, Massachusetts 02138

GAZLEY, Dr. Carl, Jr.  
Physical Sciences Department  
The Rand Corporation  
1700 Main Street  
Santa Monica, California 90406

GOLDSCHMIED, Fabio R.  
Advisory Scientist  
Heat Transfer and Fluid Dynamics Research  
Westinghouse Electric Corporation  
Research and Development Center  
Beulah Road  
Pittsburgh, Pennsylvania 15235

GOODRICH, Mr. David  
Naval Underwater Systems Center  
Code SB323  
Newport, Rhode Island 02840

GRAN, Dr. Robert  
Dynamics Technology, Inc.  
3838 Carson Street  
Torrance, California 90503

GRANVILLE, Mr. Paul S. (Code 1541)  
David Taylor Naval Ship Research and  
Development Center  
Department of the Navy  
Carderock Laboratory  
Bethesda, Maryland 20034

GRITTON, Dr. Eugene C.  
Physican Sciences Department  
The Rand Corporation  
1700 Main Street  
Santa Monica, California 90406

HAIGH, Mr. Wayne W.  
Dynamics Technology, Inc.  
3838 Carson Street  
Torrance, California 90503

HANSEN, Dr. Robert J.  
Code 8441  
Naval Research Laboratory  
Washington, D. C. 20375

HARPOLE, Mr. George  
Physical Sciences Department  
The Rand Corporation  
1700 Main Street  
Santa Monica, California 90406

HUANG, Thomas  
David Taylor Naval Ship Research and  
Development Center  
Department of the Navy  
Bethesda, Maryland 20034

KING, Dr. William S.  
Physical Sciences Department  
The Rand Corporation  
1700 Main Street  
Santa Monica, California 90406

KRALL, Mr. Kenneth M.  
Vought Corporation  
Advanced Technology Center, Inc.  
P. O. Box 6144  
Dallas, Texas 75222

LEE, Mr. Richard S.  
Undersea Systems Division  
McDonnell-Douglas Corporation  
5301 Bolsa Avenue  
Huntington Beach, California 92647

LEEHHEY, Professor Patrick  
Department of Ocean Engineering  
Massachusetts Institute of Technology  
Room 5-222  
Cambridge, Massachusetts 02139

McCARTHY, Mr. Justin H.  
David Taylor Naval Ship Research and  
Development Center  
Carderock, Maryland 20034

MACK, Dr. Leslie M.  
Jet Propulsion Laboratory  
4800 Oak Grove Drive  
Pasadena, California 91103

MANNING, Mr. Robert W.  
Naval Sea Systems Command  
PMS-395-A412  
Washington, D. C. 20362

DONOHUE, Dr. George L.  
Department of the Navy  
NUC  
San Diego, CA 92132

MERKLE, Dr. Charles  
Dynamics Technology, Inc.  
3838 Carson Street  
Torrance, California 90503

MICHEL, M. Roger  
Chef du Département d'Aérothermodynamique  
ONERA/CERT  
2, avenue Edouard Belin  
31055 - Toulouse  
FRANCE

MILLER, Dr. Richard T.  
Associate Professor of Mathematics  
Michigan State University  
East Lansing, Michigan 48823

MONS, Dr. Robert F.  
Westinghouse Electric Corporation  
Oceanic Division  
P. O. Box 1488  
Annapolis, Maryland 21404

MORKOVIN, Professor Mark V.  
Department of Mechanics and Mechanical  
and Aerospace Engineering  
Illinois Institute of Technology  
3300 South Federal Street  
Chicago, Illinois 60616

MURMAN, Dr. Earll M.  
Flow Research, Inc.  
1819 South Central Avenue  
Kent, Washington 98031

NADOLINK, Richard H.  
Naval Underwater Systems Center  
Code SB323  
Newport, Rhode Island 02840

ORMAND, Lt. Col. Lowell  
Office of Scientific Research  
AFOSR/NA Building 410  
Bolling Air Force Base, D. C. 20332

PEIRCE, Dr. Thomas E. (NSEA-0351)  
Director, Research and Technology  
Naval Sea Systems Command  
Department of the Navy  
Arlington, Virginia 20362

REISCHMAN, Dr. Michael M.  
Naval Undersea Center  
Code 2542  
San Diego, California 92132

RESHOTKO, Professor Eli  
Case Western Reserve University  
Cleveland, Ohio 44106

ROBINSON, Mr. James H.  
Code 1522  
David Taylor Naval Ship Research and  
Development Center  
Carderock Laboratory  
Bethesda, Maryland 20034

SELWYN, Dr. Philip A.  
TTO  
Defense Advanced Research Projects  
Agency  
1400 Wilson Blvd.  
Arlington, VA 22209

TAYLOR, Dr. Thomas D.  
Aerospace Corporation  
P. O. Box 92957  
Los Angeles, California 90009

VAGLIO-LAURIN, Dr. Robert  
General Applied Science Laboratory  
Merrick and Stewart  
Westbury, New York 11590

van DRIEST, Dr. Edward R.  
Physical Sciences Department  
The Rand Corporation  
1700 Main Street  
Santa Monica, California 90406

von KERCZEK, Dr. Christopher  
David Taylor Naval Ship Research and  
Development Center  
Department of the Navy  
Bethesda, Maryland 20034

WAGNER, Mr. Richard D.  
Langley Research Center  
National Aeronautics and Space  
Administration  
Hampton, Virginia 23665

WORTMAN, Dr. Andrew  
Northrup Corporation  
Ventura Division  
1515 Rancho Conejo Boulevard  
Newbury Park, California 91320

YAO, Dr. Lun-Shin  
Physical Sciences Department  
The Rand Corporation  
1700 Main Street  
Santa Monica, California 90406